

AFOSR-TR-89-0401
②

FINAL TECHNICAL REPORT

ON

AI AND Mg ALLOYS FOR AEROSPACE APPLICATIONS
USING RAPID SOLIDIFICATION AND POWDER
METALLURGY PROCESSING

AFOSR Grant No: AFOSR-85-0191

AD-A207 005

Submitted by

Hamish L. Fraser
Department of Materials Science and Engineering
University of Illinois at Urbana-Champaign
1304 W. Green Street
Urbana, IL 61801

DTIC
SELECTED
S D
APR 12 1989
R H

DISTRIBUTION STATEMENT A

Approved for public release
Distribution Unlimited

SC

REPORT DOCUMENTATION PAGE		READ INSTRUCTIONS BEFORE COMPLETING FORM
1. REPORT NUMBER AFOSR-TR-89-0401	2. GOVT ACCESSION NO.	3. RECIPIENT'S CATALOG NUMBER
4. TITLE (and Subtitle) Al and Mg Alloys for Aerospace Applications Using Rapid Solidification and Powder Metallurgy Processing		5. TYPE OF REPORT & PERIOD COVERED Final Technical Report
		6. PERFORMING ORG. REPORT NUMBER
7. AUTHOR(s) Hamish L. Fraser		8. CONTRACT OR GRANT NUMBER(s) AFOSR-85-0191
9. PERFORMING ORGANIZATION NAME AND ADDRESS University of Illinois, Dept. of Materials Science, 1304 W. Green Street, Urbana, IL 61801		10. PROGRAM ELEMENT, PROJECT, TASK AREA & WORK UNIT NUMBERS 6102F 2306/1A1
11. CONTROLLING OFFICE NAME AND ADDRESS Air Force of Scientific Research, Bolling AFB, Bldg. 410, Washington, D.C. 20332		12. REPORT DATE 3/28/89
14. MONITORING AGENCY NAME & ADDRESS (if different from Controlling Office) AFOSR, Ac Bldg. 410 Bolling AFB, D.C. 20332		13. NUMBER OF PAGES 95
16. DISTRIBUTION STATEMENT (of this Report) This document has been approved for public release; its distribution is unlimited.		15. SECURITY CLASS. (of this report) Unclassified
		15a. DECLASSIFICATION/DOWNGRADING SCHEDULE
17. DISTRIBUTION STATEMENT (of the abstract entered in Block 20, if different from Report)		
18. SUPPLEMENTARY NOTES Approved for public release, distribution unlimited		
19. KEY WORDS (Continue on reverse side if necessary and identify by block number) Rapid Solidification Processing of Al- and Mg-alloys, Powder Metallurgy, Dynamic Powder Compaction		
20. ABSTRACT (Continue on reverse side if necessary and identify by block number) On reverse side.		

The work performed during the past three years has involved studies of some elevated temperature Al and Mg alloys, and in addition a preliminary study of intermetallic compounds based on Al_3X , where X is Ti, V, and Ni+Ti.

In the case of the ALalloys, this work was in essence a continuation of the work performed during the preceeding three years of study, where rapid solidification processing (RSP) of ALalloys was investigated. Two areas were investigated, one involving alloys which might exhibit high elastic moduli, and the second concerned the improvement in fracture toughness when Si is added to AL-Fe-Mo alloys. It was found that the modulus increases in AL-Be alloys processed by rapid solidification were as expected from theory, whereas those for AL-Mn alloys were somewhat below expectation. This latter result was attributed to casting porosity present in our samples. In terms of the AL-8Fe-2Mo-Si alloys (where both 0.5% and 1.0% si have been added), the development of microstructure following RSP has been studied in alloys with, and without, the Si additions. The presence of Si resulted in the formation of the compound α -AlFeSi, with space group determined to be Im3 by convergent beam electron diffraction. The morphology of the precipitates of this compound were found to be approximately spherical and when compared with the lenticular precipitates in the case of consolidated AL-8Fe-2Mo, this shape is thought to account for the difference in fracture toughness results.

Two classes of Mg alloys have been studied, one involving Mg-rare earth element alloys, and the second light-weight Mg-Li-Si alloys. In the first of these, Mg-Gd alloys have been investigated. These alloys have been prepared by conventional casting techniques, since there is a rather large solubility of Gd in Mg, permitting solution treatment at an attractive alloying level. The decomposition of the resulting superstaured solid solution has been studied, and it has been determined that this alloy is thermally unstable, the precipitates coarsening at a considerable rate. Much work has been performed on the Mg-Li-Si system. Si is added to produce a refined dispersion of Mg_2Si , and this has been achieved by the use of rapid solidification processing. Li is added to reduce the density of the alloys. The work performed has included a detailed investigation of the phase equilibria at the Mg rich corner of the ternary system, a study of the evolution of the microstructures of rapidly solidified alloys, and an assessment of their tensile and oxidation properties. It has been shown that a refined dispersion of the phase Mg_2Si may be effected in the ternary alloy through the use of RSP. However, rather than give rise to attractive mechanical properties, decohesive rupture occurs at the particle/matrix interfaces. Most of the strengthening effect of Li appears to be associated with a grain size effect. The oxidation properties appear to be mostly affected by microstructure; a single phase microstructure appears to offer good oxidation resistance, and the presence of the phase Mg_2Si also seems to key the oxide layer mechanically to the metallic substrate.

Two approaches have been taken regarding the intermetallic compounds Al_3X , where X is either Ti, V, or Ni+Ti. The first has been to employ RSP techniques, here centrifugal atomization, for the preparation of pre-alloyed material, with low degrees of solute segregation. It has been shown that useful consolidated pieces can be produced in this way, and the microstructural development of these materials from powders to consolidated materials has been studied. A preliminary study has been made of the deformation mechanisms in these compounds. Thus, samples of consolidated materials have been compressed to about 1-3% strain at 300° and 600°C. For Al_3Ti with the DO₂₂ crystal structure, at the lower temperature, deformation is accomplished by ordered twinning and the motion of some dislocations with Burgers vectors given by $b=1/2<110]$ on {001}. At 600°C, the deformation microstructure consists of pairs of dislocations with $b=1/2<110]$ gliding on {001}, as well as dislocations with $b=1/2<112]$ gliding on {111}; these latter dislocations appear to be dissociated as $1/2<112] \rightarrow 1/3<112]+2/3<112]$. Most of the line segments lie approximately parallel to <110] directions, and this is interpreted on the basis of a possible influence of the anisotropy of charge densities on the Peierls stresses experienced by various dislocation segments.

Table of Contents

I.	Introduction	1
II.	Aluminum Alloys Studies	2
	A. High Modulus Al-Based Alloys	2
	1. Microstructure and Mechanical Properties of Al-Be Alloys	2
	2. Microstructure and Mechanical Properties of Al-Mn Alloys	6
	B. Elevated Temperature Al-8Fe-2Mo-Si Alloys	9
	1. Transformation Behavior	9
	a) Al-8Fe-2Mo Alloy	10
	b) Al-8Fe-2Mo-Si Alloy	15
	2. Mechanical Properties of Al-8Fe-2Mo-Si Alloys	22
III.	Magnesium Alloy Studies	25
	A. Alloys Based on Mg-Li	26
	1. Phase Equilibrium of Mg-Li-Si System	26
	2. Microstructures of Rapidly Solidified Mg-Li-Si Alloys	35
	3. Tensile Properties of Rapidly Solidified Mg-Li-Si Alloys	43
	4. Oxidation Behavior of some Mg Alloys	48
	a) Thermo-Gravimetric Analysis (TGA)	48
	b) Identification of Oxidation products by XRD and XPS Techniques	53
	c) In-situ Oxidation Tests	56
	d) Oxidation Model	57
	e) Oxidation Behavior of Mg Alloy "Standards"	60
	5. Conclusions	61
	B. Mg-Gd Alloys	63
	1. Aging Behavior	63
	2. Mechanical Properties	64
IV.	Intermetallic Compounds Based on Al ₃ X	
	A. Background	
	1. Crystal structures	
	2. Deformation Behavior of Al ₃ Ti Compound	
	a) Mechanical Properties of Al ₃ Ti	

(Circular stamp: DTIC - Defense Technical Information Center)

Accession For	
NTIS	<input checked="" type="checkbox"/>
DTIC TAB	<input type="checkbox"/>
Unannounced	<input type="checkbox"/>
Justification	
By _____	
Distribution/	
Availability Codes	
Dist	Avail and/or Special
A-1	

b) Defect Configurations in Al ₃ Ti	72
3. Experimental Procedure	74
B. Results	75
1. Microstructural Studies	75
a) Al-25at%Ti Alloy	75
b) Al-25at%V Alloy	76
c) Al-8at%Ni-25at%Ti Alloy	78
2. Elevated Temperature Compression Studies	80
a) Al ₃ Ti Deformed at 300°C	80
b) Al ₃ Ti Deformed at 600°C	83
c) Al ₆₇ Ni ₁₈ Ti ₂₅ Deformed at 300°C	85
d) Al ₆₇ Ni ₁₈ Ti ₂₅ Deformed at 300°C	86
V. References	87
VI. Appendix	90
VII. Publications From This Program	93
VIII. Ph.D Degrees Supported by This Program	95

Introduction

The work performed under this contract has involved three components. These include studies of elevated temperature Al and Mg based alloys, and also intermetallic compounds based on Al_3X , where X is either Ti, V, or Ni+Ti. These will be described in turn below, and in each case there are introductory statements included. Following a description of the work, lists of theses and publications resulting from this work are presented.

Aluminum Alloy Studies

High Modulus Alloys

In the following, a summary of work on conventionally cast and rapidly solidified Al-Be and Al-Mn alloys is presented. Detailed results of the microstructures have been covered in the first annual report and, are therefore, not repeated here.

Microstructures and Mechanical Properties of Al-Be Alloys

The as-cast microstructure of Al-Be alloys exhibited primary dendrites of Be, together with a eutectic mixture consisting of Be rods in an Al matrix. For this alloy, the volume fraction of Be was calculated to be 5.8%. When alloys containing increasing amounts of Be are rapidly solidified by Laser Surface Melting (LSM) and self-quenching, the microstructures showed a transition from a cellular structure consisting of Al interspersed with linear arrays of cph Be precipitates to ones consisting predominantly of a uniformly refined dispersion of bcc Be particles in an Al matrix.(1,2) The formation mechanism for these microstructures has been interpreted on the basis of undercooling prior to nucleation such that a metastable monotectic reaction occurs.(1,2) A metastable Al-Be phase diagram derived from the work of Murray (3) is shown in Figure 1. The monotectic composition is approximately 2 wt% Be.

The thermal stability of the bcc Be dispersions in the Al-4Be alloy produced by LSM was investigated by following the changes in microhardness and microstructure for samples heat-treated at 400°C. Microhardness measurements showed a decrease with aging time. Concurrently, the microstructure transformed from bcc Be particles to cph Be prism-rods. To facilitate the crystallographic analyses of these prism-rods, a higher heat-treatment temperature (500°C for 1 hr) was employed to increase the prism-rod size. The microstructure following this treatment showed both the prism-rod morphology characteristic of the 400°C treatment and a second morphology consisting of blocky particles.

Several crystallographic orientations involving cph Be were observed in the heat-treated material and are listed in Table 1. A total of 11 orientation relationships have been listed, and 8 of the 11 orientations were observed experimentally. Some of the orientation relationships (OR's) represent permutations of the symmetry elements of the other orientations. Experimental evidence for these OR's was obtained utilizing electron microscopy and the results showed that OR's 1,2,3,4, and 7 produced the prism rods in the 400°C heat treatments, and OR's 2,3, and 8 produced the more equiaxed and faceted particles observed at the higher temperature heat-treatments. A large number of variants of the 8 OR's were observed.

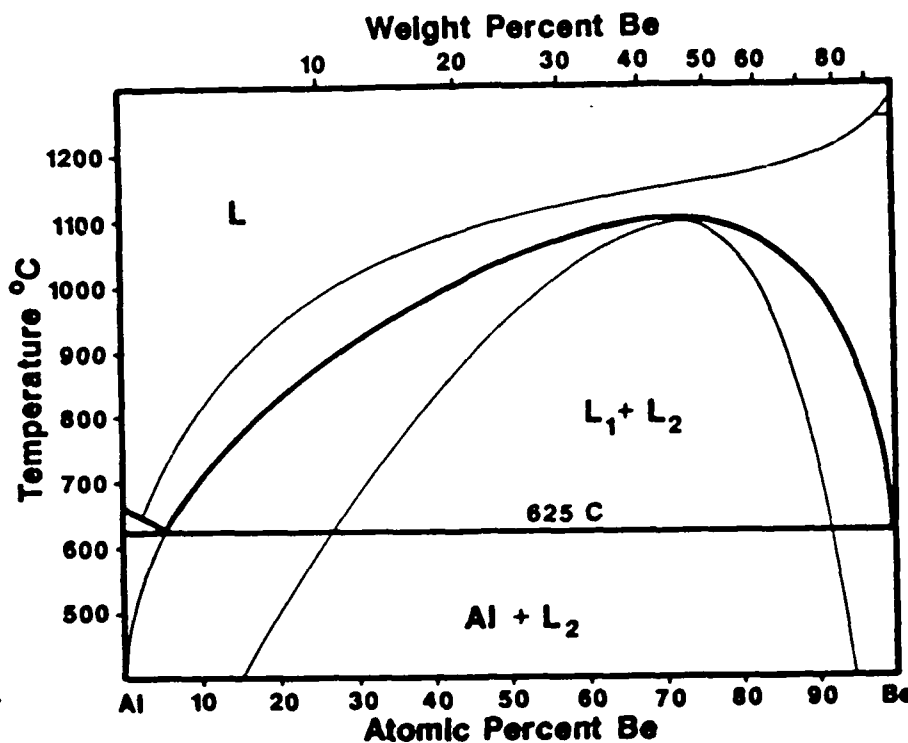


Figure 1. Metastable phase diagram for the Al-Be system.

1. [100] [12̄10]	(010) (0001)	(100) (10̄10)
2. [101] [12̄10]	(10̄1) (10̄10)	(010) (0001̄)
3. [101] [12̄10]	(10̄1) (0001)	(010) (10̄10)
4. [010] [12̄10]	(10̄1) (0001)	(101) (1010̄)
5. [101] [12̄10]	(11̄1) (0001)	(1̄21) (10̄10)
6. [101] [11̄00]	(11̄1) (0001)	(1̄21) (1120)
7. [001] [12̄10]	(100) (1011)	(010) (1012)
8. [101] [0001]	(11̄1) (1010)	(1̄21) (12̄10)
9. [101] [0001]	(11̄1) (1210)	(1̄21) (1010)
10. [101] [10̄10]	(11̄1) (12̄10)	(1̄21) (0001)
11. [101] [12̄10]	(11̄1) (1010)	(1̄21) (0001̄)

Table 1. The crystallographic orientations between Al and cph Be.

Calculations of the number of variants for each OR based on the method of Cahn and Kalonji (4) and determinations of the intersection point group and multiplicity showed that 58 possible variations of the 8 OR's can occur in any one Al grain. For the prism-rod morphology alone, there were 36 possible variants, which explained the large number of orientations observed for these. From calculations of the lattice mismatch between cph Be and Al (2) and the observable absence of a large strain contrast around the particles in the TEM micrographs, it appeared that lattice plane matching and strain energy effects (5) had little influence on the crystallography of the prism-rod Be particles.

In contrast to the LSM rapidly solidified alloys, melt spinning did not produce a uniform dispersion of Be particles. Instead, the microstructures exhibited a precursor reaction which indicated that nucleation occurred in the L₁-L₂ phase field in Figure 1 prior to the monotectic reaction. To determine the mechanical properties, ribbon particulate was extruded at 375°C with an extrusion ratio of 18:1. Optical metallography indicated a fully dense product. The hardness of the extrusion was 54 DPH. Thin foil examination of the extrusion revealed a dynamically recrystallized microstructure with Al grains (1-2 mm) containing a coarse dispersion of Be particles.

The monotonic tensile properties for the Al-4Be alloy, for both as-cast material and extruded melt-spun ribbons, is presented in Table 2. The extruded material showed significantly superior tensile strength and ductility relative to the cast material; however, the elastic modulus was about the same. Fractography revealed that the failure mode for both materials was by void coalescence.

	<u>Extruded Al-3.7Be*</u>	<u>Cast Al-4.8Be*</u>
Elastic Modulus	71.5 GPa	74.4 GPa
Yield Strength	126 MPa	127 MPa
Ultimate Strength	163 MPa	120 MPa
Reduction in Area	83%	30%
True Fracture Strength	350 MPa	172 MPa
True Fracture Ductility	1.80	0.203
Strain Hardening Exponent	0.094	0.203
Strength Coefficient	224 MPa	230 MPa

* Values reported are the average of two samples

Table 2. Monotonic Properties of Al-Be Alloys

Since the solubility of Be is less than 0.3 at pct, the elastic modulus of the Al-Be composite should depend only on the volume fraction of Be. The calculated volume fraction of 5.8% for the Al-4Be alloy is low, and therefore from the standpoint of elastic modulus, an optimal dispersion of small Be particles with high aspect ratio is preferable. Thus, the morphology and size of the Be needles in LSM heat treated material should have provided good elastic constraint to the Al matrix. Unfortunately, the precursor reaction prevented formation of these unique microstructures in the melt-spun ribbon. As a consequence, the elevated temperatures experienced during extrusion produced a microstructure consisting of a coarse dispersion of Be particles, free of the needle morphology, and therefore provided virtually no improvements in the elastic modulus. The variation in the elastic modulus with Be content is shown in Figure 2. The measured values were consistent with those calculated using the Hashin and Shtrikman formulation(6) for a dispersion of spherical particles. It was concluded that for obtaining significant improvements in the elastic modulus of Al alloys by composite alloying high Be concentrations would be required.

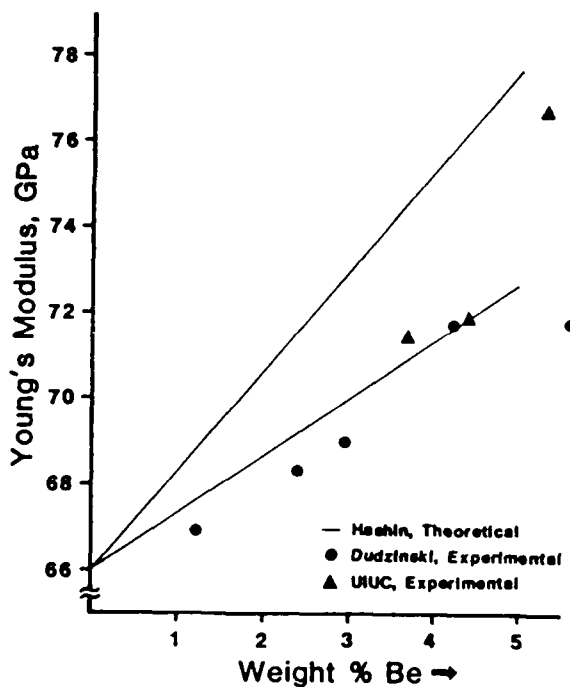


Figure 2. Variation of elastic (Young's) modulus with Be content. Theoretical bounds were calculated for a two-phase microstructure of Al and Be using modulus and Poisson's ratio values of 66 GPa and 0.33, respectively, for Al and 293 GPa and 0.039, respectively, for Be.

The fatigue strength of the Al-4Be extruded ribbon was evaluated. The results for ten samples are summarized in Table 3. Three of the ten samples were subjected to a 500°C, 1 hr heat treatment. The microstructure following this treatment consisted of coarse Be particles in an Al matrix; the prism-rod morphology characteristic of the LSM material was absent. The failure criteria, which was based on a 10% load drop, produced a crack size of 2.2 mm. Crack initiation occurred at a surface indentation caused by the knife edge of the strain guage. However, the presence of such a notch had little influence on the short term fatigue life. Fatigue striations were on the order of the grain size, and crack branching was evident. The fatigue properties of the Al-4Be alloy corresponded to that of an intermediate Al alloy, namely the 1100-T6 and 7075-T6 Al alloys.

<u>Specimen No.</u>	<u>$\Delta\varepsilon/2$</u>	<u>$\Delta\sigma/2$ (MPa)</u>	<u>Nf</u>
1	0.004	112	620
2*	0.006	86	980
3	0.006	126	321
4	0.002	99.5	6,950
6	0.0015	88	48,900
7	0.00072	50	5x10 ⁶
8	0.001	70	836,000
9*	0.00072	50	775,000
10*	0.001	70	372,000

* After heat treatment

Table 3. Fatigue Life Data of Al-3.7Be Extruded Ribbon.

Microstructures and Mechanical Properties of Al-Mn Alloys

Al-1.1Mn and Al-7.5Mn-2Mo alloys were chill cast. The effect of solution treatment (630°C for 1 hr) followed by artificial aging (200°C for 96 hrs) of the Al-1.1Mn alloy was examined. The resultant microstructure exhibited some second phase precipitation, presumably of the Al₆Mn phase.

In an effort to determine the response of Al-Mn alloys to RSP and subsequent consolidation, the Al-7.5Mn-2Mo alloy was melt spun; the resultant microstructures were cellular with intercellular regions composed of Mn rich particles. Heat treatment of the melt-spun ribbons at 400°C produced coarse second phase particles. Analytical studies revealed that the Al matrix

contained a substantial concentration of Mn after heat treatment. (7)

The variation in elastic modulus with Mn content for as-cast and solution treated (630°C for 1 hr) Al-Mn alloys is presented in Figure 3. The results show an increase in modulus of Al at a rate of 10 Gpa/at pct Mn, which differs from that of 4.8 GPa/at pct Mn reported by others(8). A rapid increase in modulus is predicted by Leigh's model(9) and the present results are consistent with this. Aging (200°C for 96 hrs) the solution-treated Al-1.1Mn alloy resulted in a drop in modulus (Figure 3); this effect was associated with the precipitation of presumably the Al₁₆Mn phase (Fig 18b). Since the volume fraction of the second phase was lower than the calculated value of 4% for the 1.1Mn composition, it was concluded that the discrepancies in modulus data were probably associated with the unreported presence of these precipitates.

Since the elastic constants for the Al₁₆Mn intermetallic are not available, the data of Dudzinski(10-12) was modelled (Figure 4) on the basis of the Hashin and Shtrikman formulation(6) to yield values of 150 Gpa and 0.25 for the elastic modulus and Poisson's ratio, respectively. Application of these results to the Al-1.1Mn alloy predicted values for the elastic modulus which were in good agreement with that measured for the artificially aged alloy. (For example, the measured modulus of 68.3 GPa is within the calculated upper and lower bounds of 68.5 and 68.1 GPa, respectively). In addition, the results showed that the increase in modulus of Al-Mn alloys

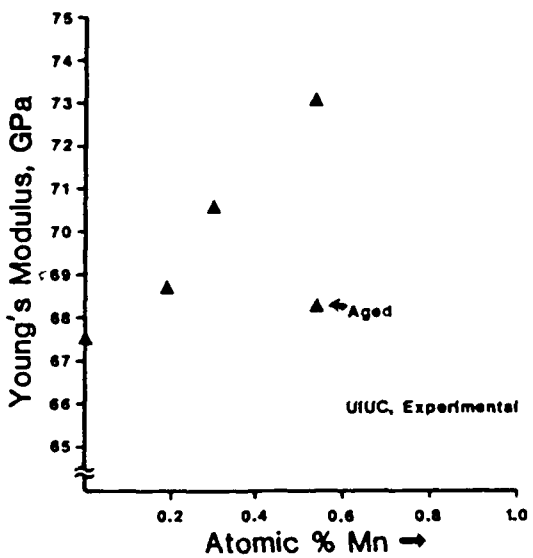


Figure 3. Variation of elastic (Young's) modulus with Mn content. Alloys were solution-treated at 630°C and quenched prior to testing.

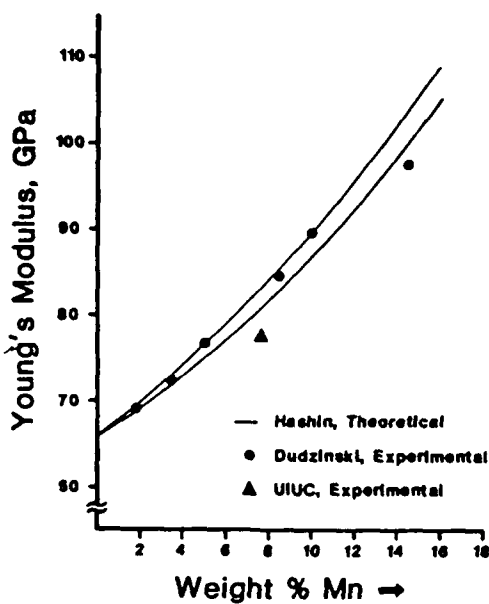


Figure 4. Variation of elastic modulus with Mn content. Theoretical bounds were calculated for a two-phase microstructure of Al and Al₆Mn using modulus and Poisson's ratio values of 66 GPa and 0.33, respectively, for Al and 150 GPa and 0.25 (determined by a best fit to Dudzinski's data), respectively, for Al₆Mn.

was associated primarily with solid solution effects.

The elastic modulus for the cast Al-7.5Mn-2Mo alloy fell outside the Hashin and Shtrikman (6) bounds (Figure 4). The low value of the elastic modulus in this material was associated with casting porosity. Brittle fracture of this cast alloy occurred and was attributed to the presence of large intermetallic particles. (7)

Elevated Temperature Al-8Fe-2Mo-Si Alloys

High purity Al-8Fe-2Mo alloy ingots containing 0, 0.5 and 1 wt.% Si were produced by induction melting in an argon atmosphere and casting into a copper mold. The ingots were sectioned, induction remelted in a quartz crucible under helium, and ejected by argon pressure onto a mild steel wheel rotating at a surface velocity of 35 m/s to produce rapidly solidified ribbons having a thickness of 25 to 50 mm and width of 3 to 6 mm. Cut ribbons were encapsulated in quartz under vacuum, and after heat-treating at 450°C for various times to 100 hrs quenched in water to arrest further transformation.

X-ray diffraction studies were performed on a Rigaku D-max diffractometer using Cu K α radiation. Heat-treated ribbons (450°C, 50 hrs) of the 0.5 and 1 wt.% Si alloys were mounted on a glass slide, placed in the diffractometer chamber, and the patterns recorded. The scan was repeated five times and the intensities summed each time. Transmission electron microscopy (TEM) studies were carried out in the Philips EM420 and EM430 microscopes operating at 120 and 150 keV, respectively. Energy dispersive x-ray (EDX) microanalysis of the precipitates was conducted in a Vacuum Generators HB5 STEM, equipped with a field emission gun. The concentration of different elements was determined from the intensity of x-rays using standard techniques.⁽¹³⁾ The proportionality constant relating the concentration ratios to the intensity ratios of the different elements⁽¹³⁾ was determined using Al₁₂Mo, Mo₃Si, and Fe₂Mo line-compound standards.

Transformation Behavior

The optical microstructure of Al-8Fe alloy particulate produced by RSP has been described by Jones⁽¹⁴⁾ as either Zone A or Zone B, depending on its response to etching by Keller's reagent; the microstructure of the former appears featureless, whereas that of the latter exhibits strong contrast characteristic of a decomposed microstructure. On a finer scale, the Zone A microstructure appears as a cellular-dendritic structure based on α -Al with intercellular regions composed of a randomly oriented refined dispersion of particles of the quasicrystalline T' phase.⁽¹⁵⁾ The as-rapidly solidified microstructure of all three alloys was completely Zone A, as shown, for example, in Figure 5 for the 0.5 wt.% Si alloy. The microstructural changes in ribbons heat-treated at 450°C for times ranging from 0.25 to 100 hrs are described in the following.

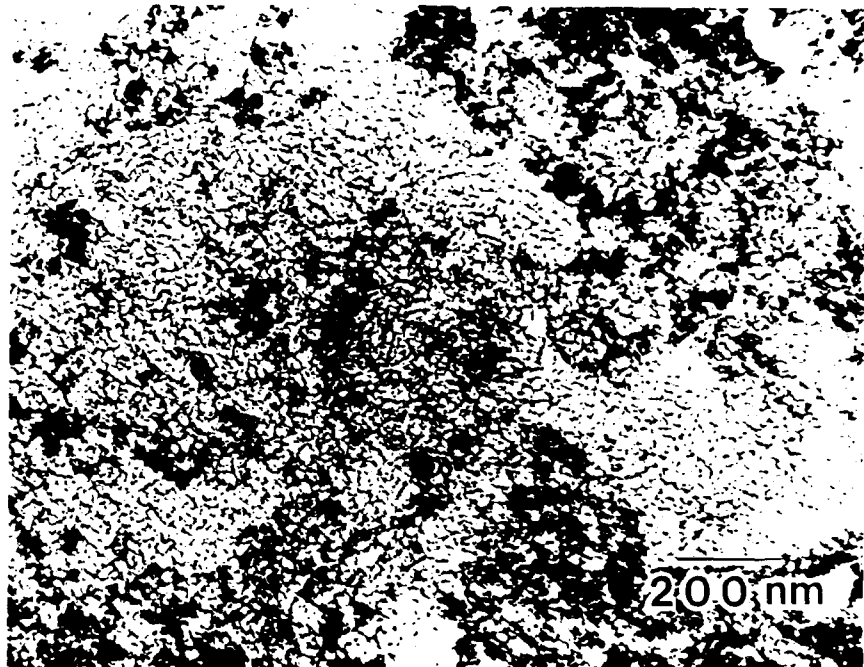


Figure 5. BF micrograph of as-rapidly solidified Al-8Fe-2Mo-0.5Si alloy ribbon.

Al-8Fe-2Mo Alloy

Within 0.25 hrs, precipitation occurred at grain boundaries, as shown in the bright field (BF) micrograph in Figure 6a. Two types of precipitates, the $\text{Al}_6(\text{Fe},\text{Mo})$ phase(14,16,17) and a body centered cubic (BCC) phase having a lattice parameter of 1.27 ± 0.005 nm, were identified; the latter phase was observed more commonly. A selected area diffraction (SAD) pattern from the grain boundary precipitate indicated by the arrow in Figure 6a is shown in Figure 6b. This and other patterns could be indexed consistently on the basis of a BCC lattice. Energy dispersive x-ray (EDX) microanalysis indicated that the BCC phase was based on Al and contained significantly larger amounts of Fe compared to Mo; small amounts of Si were also present. The exact stoichiometry has not been determined yet, but is tentatively described as $\text{Al}_p(\text{Fe},\text{Mo})$. Generally, other than a slight coarsening of the intercellular phase, the intragranular structure showed little or no change in most areas of the microstructure. However, thicker portions of the ribbon showed more decomposition, as seen in the example in Figure 6c. The grain boundary precipitate labelled P in Figure 6c was once again identified as the BCC $\text{Al}_p(\text{Fe},\text{Mo})$ phase (see associated SAD pattern in Figure 6d). On occasion, the BCC phase was also observed as faceted particles within grains.

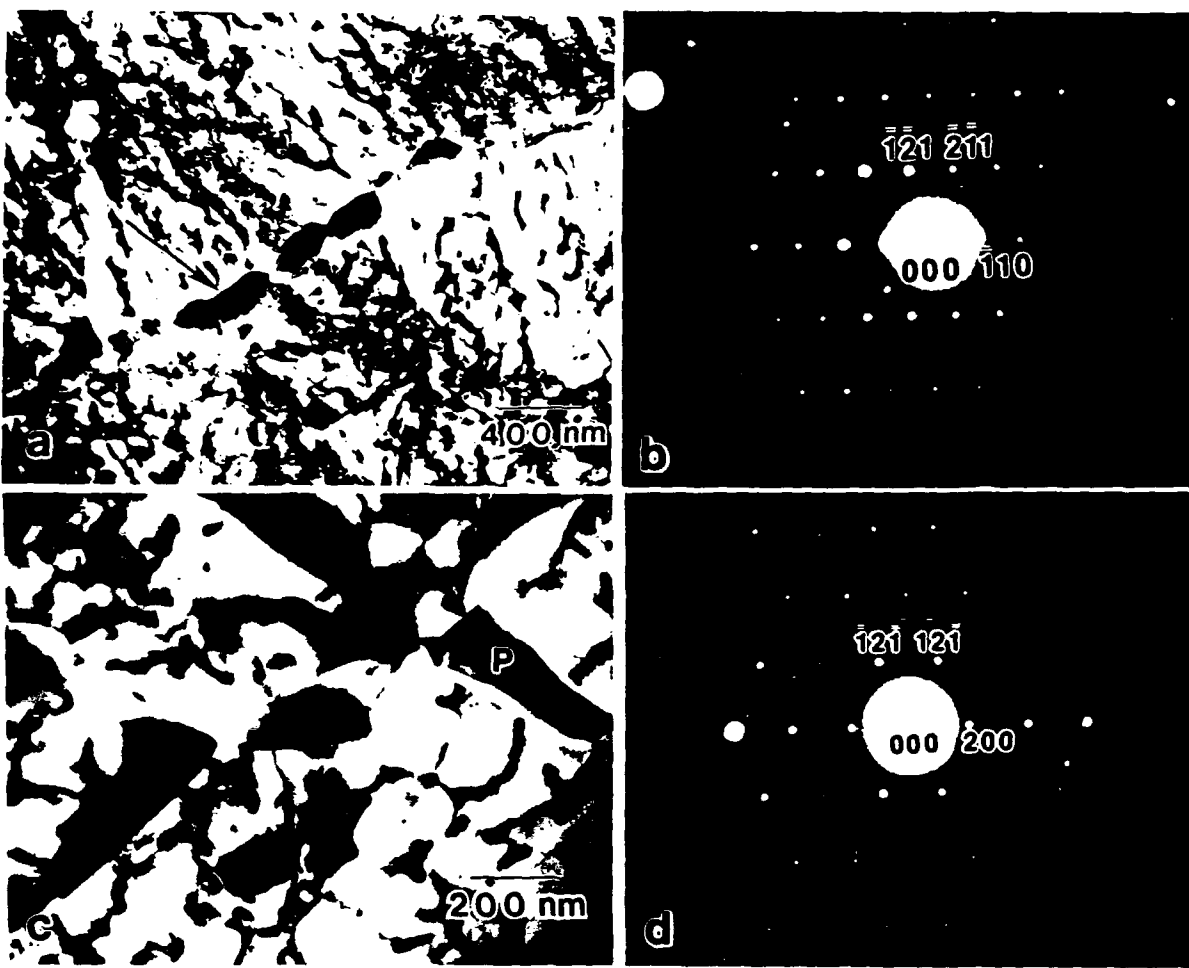


Figure 6. Al-8Fe-2Mo alloy ribbon aged at 450°C for 0.25 hrs. a) BF micrograph; b) [113] SAD pattern of precipitate indicated by arrow in "a"; c) BF micrograph from thicker area; d) [012] SAD pattern from precipitate labelled P in "c".

Further aging to 4 hrs led to additional precipitation of the $\text{Al}_6(\text{Fe},\text{Mo})$ and $\text{Al}_p(\text{Fe},\text{Mo})$ phases, together with transformation of the intragranular structure to needles of the orthorhombic θ' Al_3Fe phase.(16,17) Representative examples are shown in Figures 7a and 7b. The precipitate labelled A in Figure 7b was identified as $\text{Al}_6(\text{Fe},\text{Mo})$ (see SAD pattern in Figure 7c), whereas the one labelled B was identified as the BCC $\text{Al}_p(\text{Fe},\text{Mo})$ phase (see [001] SAD pattern in Figure 7d). The BCC Bravais lattice for this phase was confirmed by convergent beam electron diffraction.

On continued aging to 50 hrs, the orthorhombic θ' Al_3Fe needles disappeared; the microstructure at this stage consisted of a dispersion of rather coarse precipitates of the $\text{Al}_6(\text{Fe},\text{Mo})$, $\text{Al}_p(\text{Fe},\text{Mo})$ and the monoclinic Al_3Fe phases. In addition, a phase, tentatively identified as the BCC Al_{12}Mo (lattice parameter of 0.758 nm), was also detected. TEM micrographs showing the $\text{Al}_6(\text{Fe},\text{Mo})$, $\text{Al}_p(\text{Fe},\text{Mo})$ and Al_{12}Mo phases are presented in Figures 8a-d. Evidence for the monoclinic Al_3Fe phase is shown in Figure 9. This phase forms incoherently

and displays fine twins (Figure 9a), which produce extra spots and streaks in the diffraction pattern (Figure 9b); the streaks form normal to the thin dimension of the twins. It appeared that the Al₃Fe phase formed at the grain boundaries from the Al₆(Fe,Mo) and Al_p(Fe,Mo) phases.

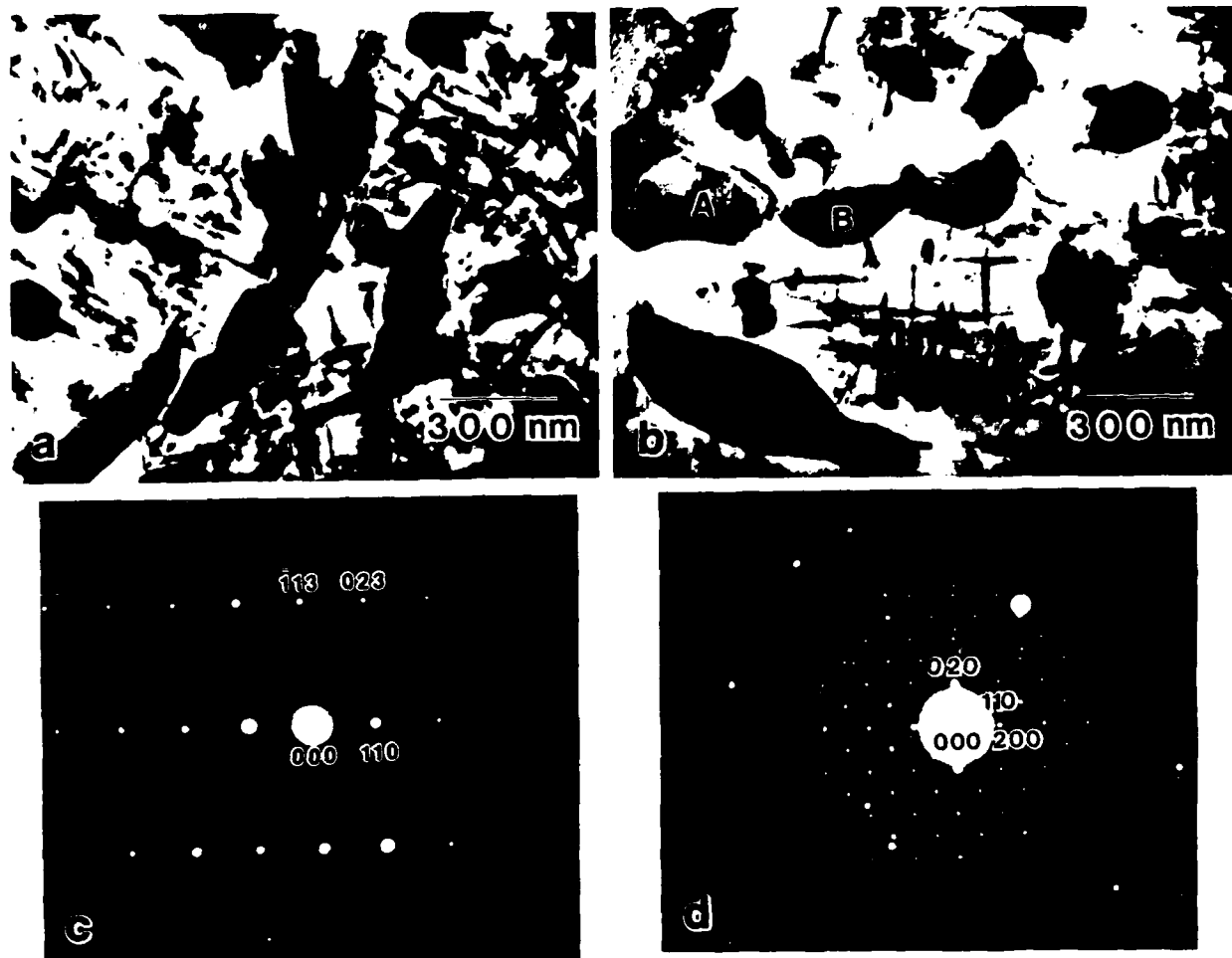


Figure 7. Al-8Fe-2Mo alloy ribbon aged at 450°C for 4 hrs. a), b) BF micrographs; c) [332] and d) [001] SAD patterns of Al₆(Fe,Mo) and Al_p(Fe,Mo) precipitates labelled A and B, respectively in "b".

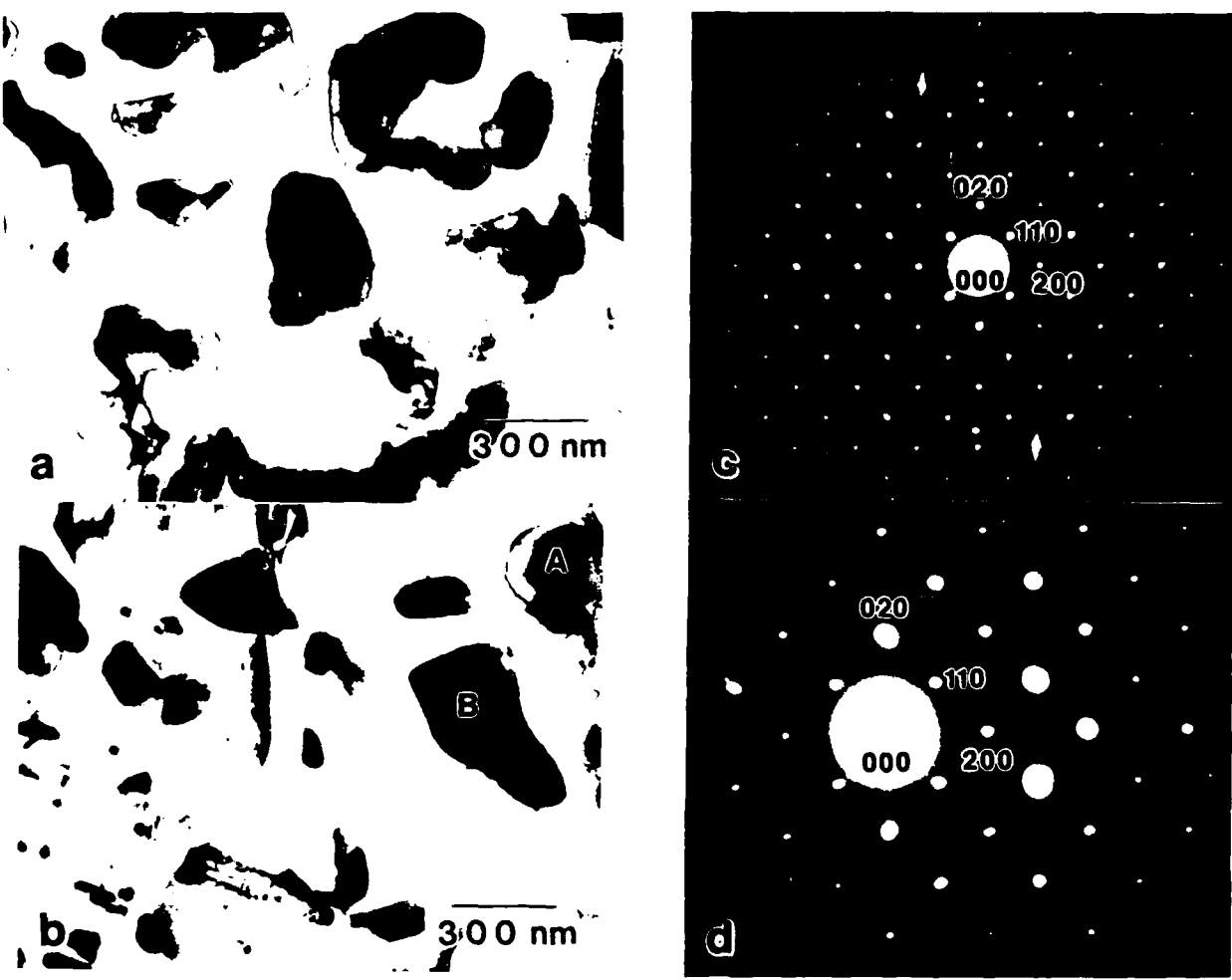


Figure 8. Al-8Fe-2Mo alloy ribbon aged at 450°C for 50 hrs. a) BF micrograph showing Al₆(Fe,Mo) precipitates; b) BF micrograph showing the Al₁₂(Fe,Mo) (labelled A) and the Al₁₂Mo (labelled B) phases; c), d) [001] SAD patterns of the precipitates labelled A and B in "b".

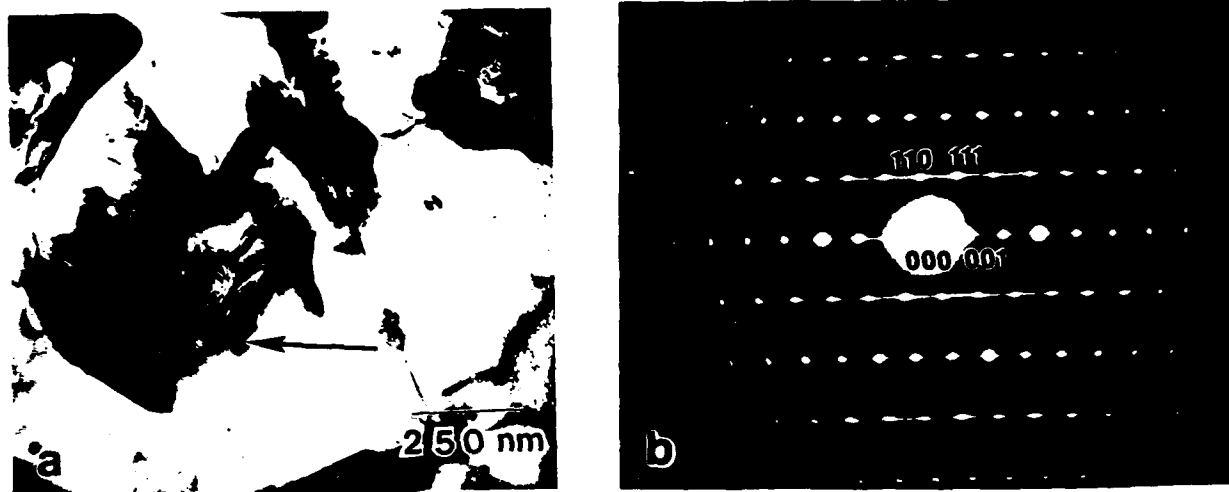


Figure 9. Al-8Fe-2Mo alloy ribbon aged at 450°C for 50 hrs. a) BF micrograph showing the monoclinic Al₃Fe phase (see arrow); b) [110] SAD pattern.

Al-8Fe-2Mo-Si Alloys

The aging response of these alloys was markedly different from that of the Al-8Fe-2Mo alloy. In contrast to the behavior of the ternary alloy at 0.25 hrs, precipitation was not limited to the grain and subgrain boundaries alone, but instead spread throughout the microstructure. A BF micrograph demonstrating this effect is shown in Figure 10a for the 0.5 wt.% Si alloy. The precipitates which form at the grain and sub-grain boundaries are larger than those inside the grains; the latter appear with a straight-edged cuboidal/polygonal morphology, which indicates that nucleation may have taken place coherently.

Further aging to 4 hrs produced virtually no change in the microstructure (Figure 10b). Although the intragranular precipitation processes commenced somewhat earlier in the Si-containing alloys relative to the Si-free alloy, the overall thermal stability was markedly superior, as evident from Figures 10c and 10d, where the microstructures after a 50 hr aging are shown. There is some evidence of particle coarsening and spheroidization; however, the microstructures do not show the marked coarsening characteristic of the Al-8Fe-2Mo alloy. Moreover, no evidence

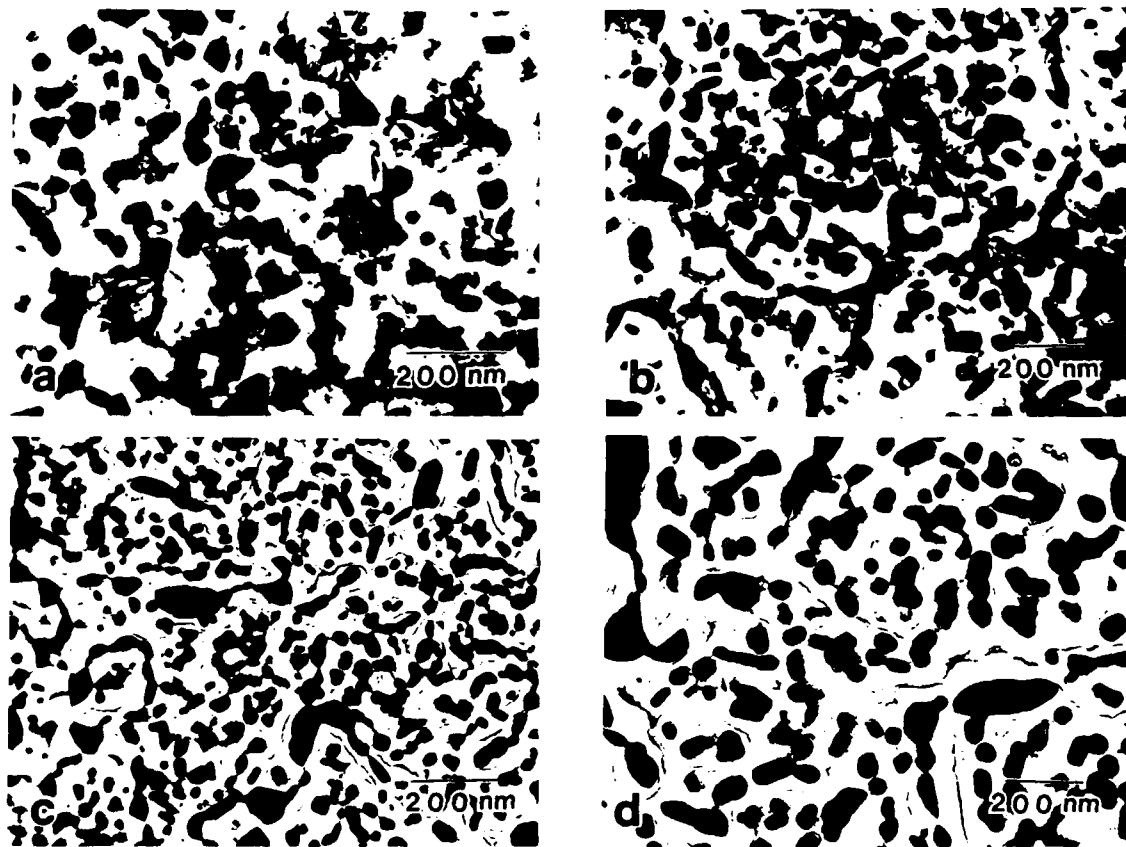


Figure 10. BF micrographs of Al-8Fe-2Mo-Si alloy ribbons aged at 450°C. 0.5 wt.% Si alloy—a) 0.25 hrs; b) 4 hrs; c) 50 hrs; d) 1 wt.% Si alloy, 50 hrs.

was seen for either the Al₆Fe or the incoherent monoclinic Al₃Fe phases even after 100 hrs aging.

A typical x-ray diffraction pattern showing the variation of intensity (cps) as a function of 2θ is presented in Figure 11 for the 1 wt.% Si alloy. The results of peak position, intensity, indexing and d-spacing of the various reflections are summarized in Table 4. All the precipitate reflections could be consistently indexed on the basis of a BCC lattice ($h+k+l = 2n$) with $a_0 = 1.263 \pm 0.003$ nm, which closely matches the value of 1.256 nm for the BCC a-AlFeSi compound,(18) and that of the precipitates reported in Al-8Fe-V-Si alloys.(19) No apparent change in the lattice parameter with Si content was observed. It should be noted that the 532 reflection is the strongest, followed by the 530, in agreement with other reports.(20) Detailed calculations of the structure factors to enable evaluation of the intensities has not been attempted.

Electron diffraction studies were carried out to confirm the x-ray results. Examples of diffraction patterns recorded from individual precipitates, covering the [001]-[011]-[111] stereographic triangle, are shown in Figure 12. These and all other patterns could be consistently indexed on the basis of a BCC lattice with a lattice parameter almost identical to that determined by x-ray diffraction.

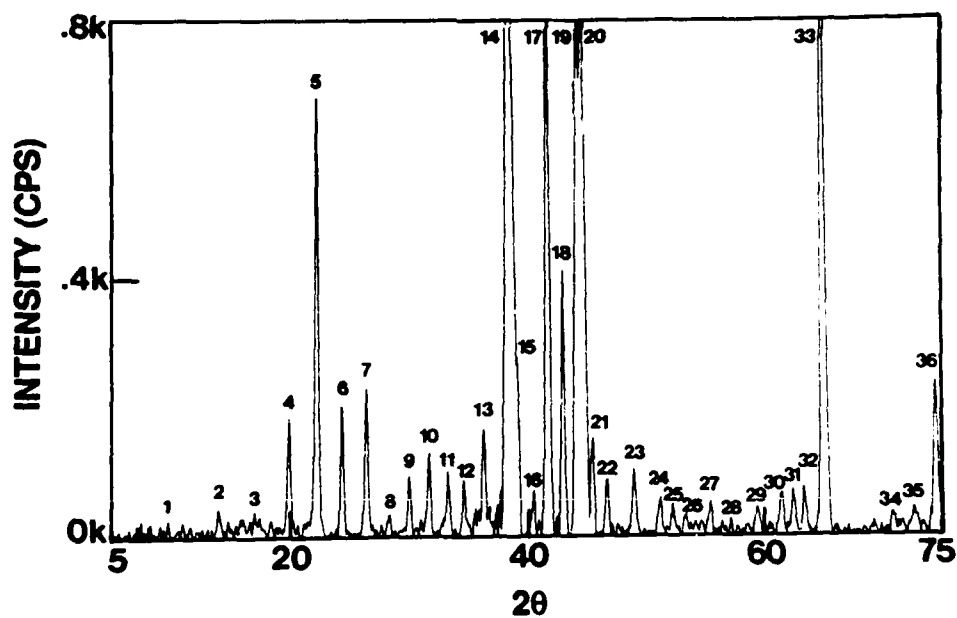


Figure 11. Variation of intensity as a function of 2θ for the 1 wt.% Si alloy heat-treated at 450°C for 50 hrs.

Peak No.	2θ	Intensity (cps)	I/I₀ ppt.	hkl	d, nm	a₀, nm
1	9.80	170	10	110	0.902	1.275
2	13.98	167	9	200	0.633	1.266
3	17.10	162	9	211	0.519	1.269
4	19.86	312	17	220	0.447	1.264
5	22.24	808	45	310	0.399	1.263
6	24.38	315	17	222	0.365	1.264
7	26.40	330	18	321	0.337	1.262
8	28.30	116	6	400	0.315	1.261
9	30.02	178	10	330/411	0.297	1.262
10	31.70	221	12	420	0.282	1.261
11	33.28	194	11	332	0.269	1.262
12	34.60	182	10	422	0.259	1.269
13	36.28	295	16	431/510	0.248	1.262
14	38.46	18837	--	111 Al	0.234	0.405
15	39.04	511	28	521	0.231	1.263
16	40.44	236	13	440	0.223	1.261
17	41.72	1287	71	433/530	0.216	1.261
18	43.00	594	33	600	0.210	1.261
19	44.24	1811	100	532/611	0.205	1.261
20	44.70	3094	--	200 Al	0.203	0.406
21	45.42	335	19	620	0.200	1.262
22	46.64	210	12	541	0.195	1.261
23	48.94	208	12	631	0.186	1.262
24	51.20	160	9	550/543/710	0.178	1.261
25	52.26	145	8	640	0.175	1.261
26	53.34	119	6	552/633/712	0.172	1.261
27	55.46	142	8	730	0.166	1.261
28	57.22	132	7	651/732	0.161	1.266
29	59.40	136	8	554/741	0.156	1.263
30	61.46	170	9	653	0.151	1.261
31	62.44	180	10	660/822	0.149	1.261
32	63.40	182	10	743/750/831	0.147	1.261
33	65.10	1260	--	220 Al	0.143	0.405
34	70.84	126	7	754/851	0.133	1.261
35	72.56	139	8	763	0.130	1.262
36	74.42	363	20	770/853/941	0.127	1.261

Average $a_0 = 1.263 \pm 0.003$ nm

Table 4. Summary of X-ray diffraction results.

To determine the point group and space group of the precipitates, convergent beam electron diffraction (CBED) was used. CBED patterns of the [001], [023], and [111] zone axes are shown in Figures 13a-c. The BCC Bravais lattice for the precipitates is once again confirmed by examining the spacings and positions of reflections in the Zero Order Laue Zone (ZOLZ) and the First Order Laue Zone (FOLZ) in the [001] pattern. For a BCC lattice, the ratio of the spacings of the FOLZ and ZOLZ is equal to $\sqrt{2}$.⁽²¹⁾ Measurements of these spacings from the patterns in Figure 13a gave $d_{\text{FOLZ}}/d_{\text{ZOLZ}} = 12.68/9.03 = 1.4 \approx \sqrt{2}$, thus confirming the BCC lattice. Symmetry information deduced from the CBED patterns in Figures 13a-c was compared to tables provided by Buxton et al.⁽²²⁾ The results are summarized in Table 5. For the [001] orientation, the projection diffraction and whole pattern symmetries are 2mm, which places the diffraction group as 2mm or 2mm1R. For the [023] zone axes, the projection diffraction, whole pattern and bright field (BF) symmetries are 2mm, m, and m, respectively, which gives 2RmmR as the diffraction group. For the [111] zone axes, the projection diffraction and whole pattern symmetries are 6 and 3, respectively, which gives the diffraction group as 6R. The possible point groups corresponding

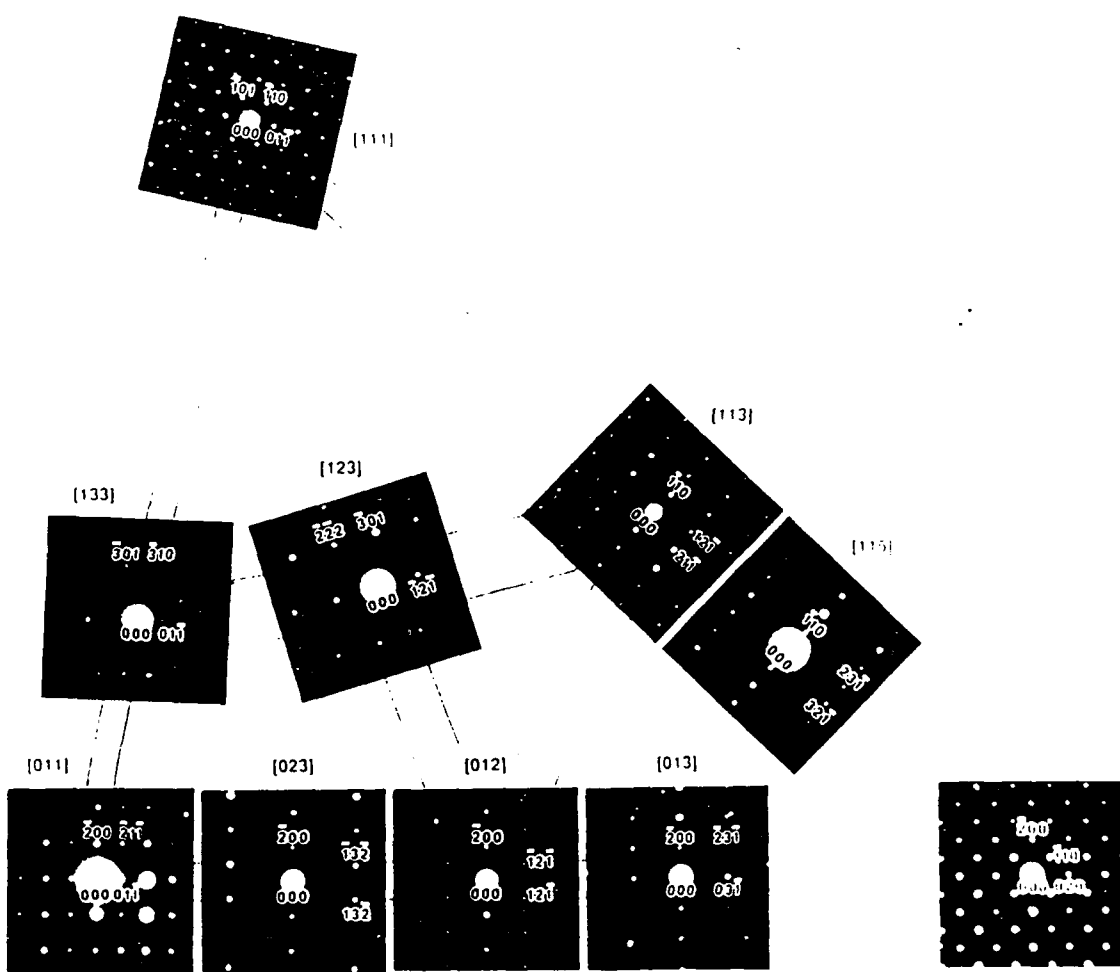


Figure 12. Examples of electron diffraction patterns recorded from individual precipitates.

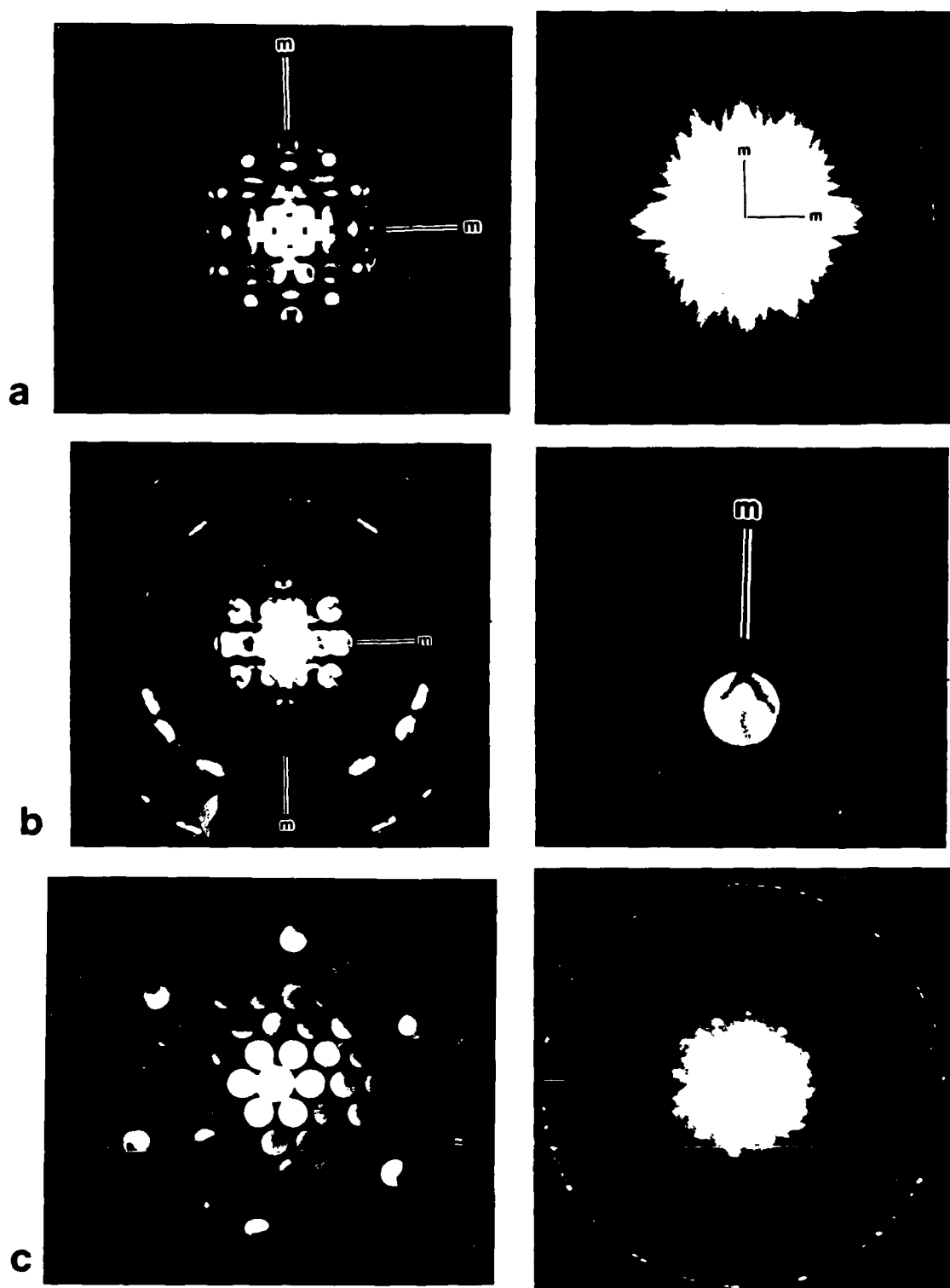


Figure 13. CBED patterns taken from precipitates. a) [001] showing 2mm projection and whole pattern symmetries; b) [023] showing 2mm projection symmetry and m whole pattern and bright field symmetries; c) [111] showing 6 and 3 projection and whole pattern symmetries, respectively.

Zone Axis	Observed Symmetry			Deduced Diffraction Group
	Projection	Whole Pattern	BF	
[001]	2mm	2mm	—	2mm or $2mm\bar{1}_R$
{023}	2mm	m	m	2_Rmm_R
{111}	6	3	—	6_R

Table 5. Observed symmetries and deduced diffraction groups.

Deduced Diffraction Groups	Possible Point Groups						
2mm	mm2		6m2				
$2mm\bar{1}_R$		mmm	4mmm	6/mmm		m3	m3m
2_Rmm_R	2/m	mmmm	4/m	4mmm	6/mmm	3m	6m
6_R		3				m3	m3m

Table 6. Possible point groups corresponding to the deduced diffraction groups.

to the above diffraction groups (Table 3 of Buxton et al.(22)) are summarized in Table 6, from which it is established that the point group of the precipitates is m3.

The possible space groups for this point group are Pm3, Pn3, Pa3, Fm3, Fd3, Im3, and Ia3.23 Since the lattice is BCC, the choice of space groups is reduced to the last two, namely, Im3 or Ia3. For the latter space group, reflections of type $0kl$ for which k and l are not multiples of 2, that is, of type $011, 033\dots$, are forbidden, which is not the case here. Thus, the space group of the precipitates is unambiguously established as Im3, in agreement with that reported for the cubic a-AlFeSi compound.(18)

EDX microanalysis of the precipitates in both alloys was carried out. A typical spectrum of the intensity (counts) as a function of energy (keV) is shown in Figure 14 for the 0.5 wt.% Si alloy. The average composition of the precipitates in both alloys, based on analyses of ten particles, is given in Table 7, together with that reported(24) for the cubic a-AlFeSi compound; it is evident that the compositions determined in this study are in excellent agreement. The structure, composition and morphology of these precipitates is identical to that of the precipitates reported in rapidly solidified and extruded in Al-Fe-V-Si alloys.(19)

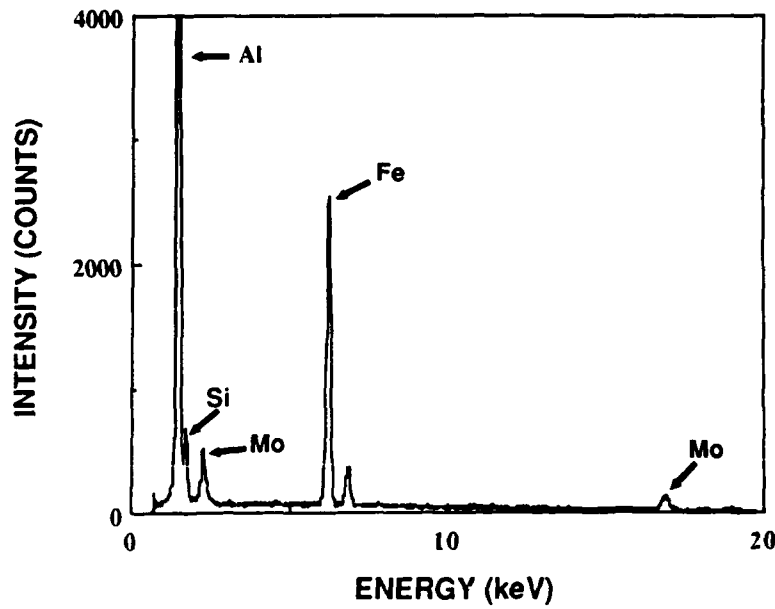


Figure 14. Typical EDX intensity spectrum taken from precipitates in the 0.5 wt.% Si alloy heat-treated at 450°C for 50 hrs.

Al.(25) A closer inspection of the composition reported by Phragmen(24) indicates a stoichiometry near Al₁₂Fe₃Si. The equilibrium a-AlFeSi compound has an HCP structure with $c=2.62$ nm and $a=1.23$ nm, but is modified to the cubic form with a_0 in the range of 1.25 to 1.27 nm by the presence of minor amounts (< 0.3 wt.%) of transition elements, notably Mn, V, Cr, W and Mo, substituting for the Fe.(26,27) The stoichiometric formula determined for the precipitates in this study corresponds to Al₁₉Fe₄Mo_{0.3}Si_{1.3} and Al₁₉Fe₄Mo_{0.3}Si_{1.7} for the 0.5 wt.% and 1 wt.% Si alloys, respectively, which is comparable to Al₁₉Fe₄MnSi₂ reported by Cooper(18) when trace amounts of Mn are present. On the assumption that the Mo atoms partially substitute for the Fe, the stoichiometry is obtained as Al₁₅Fe₄Si for the 0.5 wt.% Si alloy and as Al₁₁Fe₃Si for the 1 wt.% Si alloy, both being quite close to Al₁₂Fe₃Si.

Examination of the ternary Al-Fe-Si phase diagram(24,25) reveals that the equilibrium phases expected near 450°C for the alloy compositions used in this study are α -Al + Al₃Fe + cubic α -AlFeSi. However, the monoclinic Al₃Fe phase was not observed even after 100 hrs aging, although this phase is observed in the ternary Al-8Fe-2Mo alloy. Thus, an additional effect of Mo is to suppress the formation of this phase, either due to kinetic factors or thermodynamically by systematic alteration of the phase boundaries.

Mechanical Properties of Al-8Fe-2Mo-Si Alloys

The rapidly solidified ribbons of the Al-8Fe-2Mo-0.5Si alloy were reduced to powder, vacuum outgassed at 300°C for 4 hrs and sealed in an aluminum can. The can was subsequently extruded at 300°C using an extrusion ratio of 14:1. Optical microscopy revealed that full densification was achieved and that the zone A microstructure present in the original ribbons had decomposed. TEM revealed a relatively uniform and fine dispersion of bcc Al₁₂Fe₃Si particles of average size 30 to 40 nm in an Al matrix. The grain size was quite fine and numerous subgrains were present. In some areas of the extruded material, the particles were much larger and it was concluded that these corresponded to original ribbons with a coarser zone A structure, i.e., thicker ribbons.

Tensile samples, 3 inches long, 1/8 inch gage diameter and 1 inch gage length were machined from the extruded bar and pulled to failure under a strain rate of 10^{-4} s⁻¹. The yield strength as a function of temperature is shown in Figure 15. The data of an Al-Fe-V-Si alloy (??ref.??) is also included for comparison. The Fe and Si content of this alloy were somewhat larger than those in our alloy, so that the volume fraction of precipitates is larger. This gives rise to a higher strength compared to our alloy. The dislocation microstructure of the sample deformed at room temperature was examined using TEM. Both dislocation bowing and looping around particles was observed. On this basis, it was concluded that the room temperature strength could be

This Study				Phragmen (ref. 12)		
0.5 wt.% Si Alloy		1.0 wt.% Si Alloy				
	wt. %	at. %	wt. %	at. %	wt. %	
Al	62.1	75.9	62.6	75.5	62.5	
Fe	29.6	17.5	28.1	16.4	31.9	
	} 33.4		} 18.8		} 17.6	
Mo	3.8	1.3	3.4	1.2	—	
Si	4.5	5.3	5.9	6.9	5.6	
					6.5	

Table 7. Composition of the cubic α -AlFeSi compound.

The decomposition behavior of the Zone A microstructure in the Al-8Fe-2Mo alloy on aging is largely similar to that in binary Al-Fe alloys,(16,17) where the reaction takes place in three steps, namely: 1) formation of Al₆(Fe,Mo) at the grain boundaries, 2) transformation of the intragranular structure to needles of the orthorhombic θ' Al₃Fe phase, and 3) transformation of these two phases to the equilibrium monoclinic Al₃Fe phase. In contrast, the transformation progresses more slowly in the ternary alloy. In addition to the phases mentioned above, two other phases have been detected in the present study, namely, the BCC Al_p(Fe,Mo) and the BCC Al₁₂Mo. The Al_p(Fe,Mo) phase and the precipitates in the Si-containing alloys are identical in structure and have closely comparable lattice parameters. Since Si was detected in this phase, trace amounts of this element present as an impurity presumably cause its formation. The Al₁₂Mo phase forms possibly from the excess Mo which was not accommodated in the Al₆(Fe,Mo) and Al_p(Fe,Mo) phases.

The difference in transformation behavior between the Al-8Fe-2Mo alloy and the alloys containing Si can be understood on the basis of ternary Al-Fe-Si phase diagram. There is no published data on the Al-Fe-Mo phase diagram, but the present results suggest that with the addition of Si, the transformation behavior follows that in the Al-Fe-Si system, with Mo atoms substituting for the Fe.

The cubic α -AlFeSi compound is complex with 138 atoms per unit cell,(18) has a stoichiometry corresponding to Al₂₀Fe₅Si₂,(24) and a range of homogeneity of about 5 wt.%

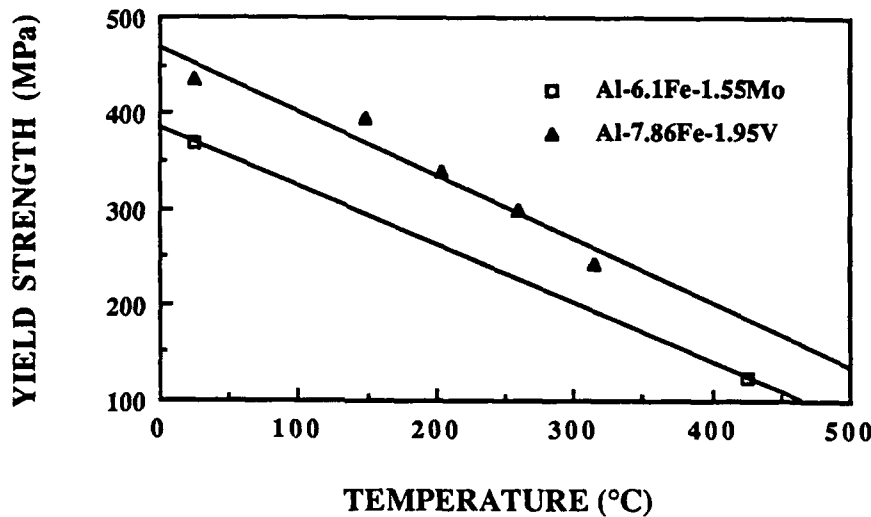


Figure 15. Variation of yield stress with temperature of extruded Al-8Fe-2Mo-0.5Si alloy ribbons.

accounted for by the Orowan mechanism. The mechanisms of strengthening at elevated temperatures was not determined. Cut samples of the extruded bar, 5x5x12 mm were creep tested at 400 and 500°C. The results, shown in Figure 16, indicated that the creep strength is comparable to Al-Fe-V-Si alloys. The dislocation structures of the crept samples have not been examined, so that mechanisms of creep of these alloys has not been ascertained. Studies of the deformation mechanisms at elevated temperatures are being carried out.

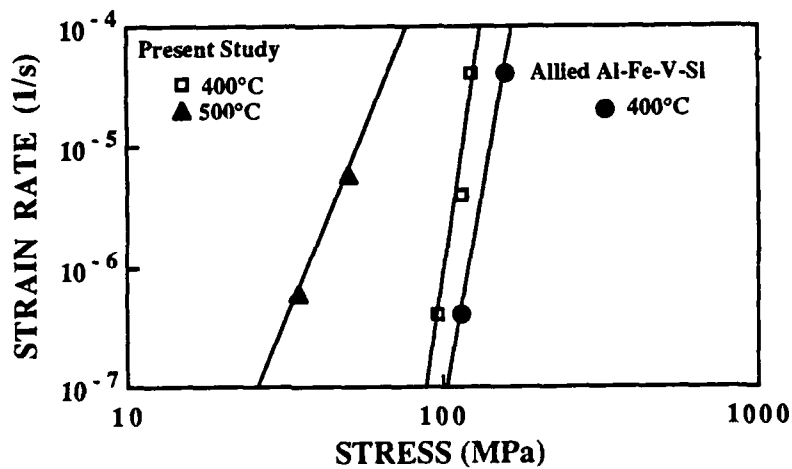


Figure 16. Creep properties of extruded Al-8Fe-2Mo-0.5Si alloy ribbons tested in the present study and those of a commercial Al-Fe-V-Si alloy.

Magnesium Alloy Studies

There is considerable interest in the development of the elevated temperature Magnesium (Mg) alloys for aerospace applications, since it is the lightest amongst all non-toxic metals. Mg is generally extracted from the sea water and commercial purity of 99.8% or better can easily be achieved. Mg is normally used as an alloying element in various metallic alloys. Although, Mg alloys possess excellent strength-to-weight ratio and machinability, their development and growth have been limited by three major factors: high cost, poor corrosion resistance and poor formability. The poor corrosion resistance of Mg alloys is related to their high chemical reactivity and to the segregation of alloying elements leading to localized cathodic centers. Poor formability is due to a limited number of slip systems in cph Mg alloys, which exacerbates the problem of polycrystalline ductility. It may be suggested that both of these potential limitations may be alleviated to certain degrees by Rapid Solidification Processing (RSP). For example, through the use of RSP, a more homogeneous material can be formed, thereby avoiding the segregation of the deleterious elements with an attendant improvement of the corrosion resistance. Also, it may be possible to improve the poor formability by alloying, reducing the grain size, and by the introduction of a refined dispersion of second phase particles. RSP plays a major role in this regard. RSP can result in the extension of solid solubility and in the formation of a refined dispersion of second phase particles. Thermal stability of the particles becomes important for the elevated temperature applications. Alloying elements such as Si and Y possess low solubilities and diffusivities in Mg and it is expected that the resulting precipitates will be thermally stable. In fact, it has been shown that in binary Mg-Si alloys, a thermally stable coupled eutectic structure consisting of rods of Mg₂Si in a Mg matrix can be obtained by melt spinning⁽²⁹⁾. The strength-to-weight ratio can be further improved by alloying Mg with Li. Mg-Li alloys are the lightest amongst all known alloys of Mg. Moreover, the addition of Li imparts ductility by reducing the c/a ratio of the cph (Mg) matrix. Based on the above, it appears that by combining the effects of Si and Li and utilizing the benefits of RSP, an optimum combination of properties may be achieved.

In order to understand the effect of RSP on Mg-Li-Si system, it is very important to understand the phase stability of the as cast Mg-Li-Si alloys. Attempts have been made to understand the equilibrium behavior of Mg-Li-Si system. This study also focusses on the evolution of the microstructure of RSP materials and their mechanical properties. Further experiments have been carried out to understand the oxidation behaviors of as cast Mg-Li-Si and several other Mg alloys.

In the case of the studies of Mg-Gd alloys, the following remarks may be made. Firstly, the aging sequence for alloys which had been solution-treated and quenched has been established. Thus, following quenching, decomposition of the super-saturated solid solution involves the

formation of coherent zones with a structure consistent with that of Mg₃Cd, with lattice parameters given by $a=6.43\text{\AA}$ and $c=5.2\text{\AA}$. These zones develop upon further aging into semi-coherent precipitates with an orthorhombic structure with lattice parameters given by $a=22.24\text{\AA}$, $b=6.42\text{\AA}$ and $c=5.21\text{\AA}$. Finally, the equilibrium phase Mg₂₄Gd₅ is formed. The highest hardness achieved during aging was ≈ 133 (Knoop microhardness), obtained by aging for 2hrs at 300°C. The microstructure corresponding to that condition consisted of ellipsoidal particles of the orthorhombic phase, mentioned above, in a Mg matrix. This microstructural condition also gave rise to the highest strengths in tensile tests.

The mechanical properties of these alloys was shown to be dependent on Gd content. Thus, although higher ultimate tensile strengths were realized in the case of alloys containing 20%Gd, a more satisfactory combination of properties were effected in the alloys containing 10%Gd. This was in part attributed to reduced grain boundary precipitation in the case of the more dilute alloy. In summary, the mechanical test results are indeed relatively exciting, and may be correlated in part to microstructure.

Alloys Based on Mg-Li

The work in this program was intended to emphasize the aspects of rapid solidification of the Mg-Li-Si alloy system; of particular interest are the microstructural development, the corresponding mechanical properties and also oxidation response. However, little is known about the phase equilibria in this system under conditions close to equilibrium, nor of the oxidation response of conventionally processed materials. As will be seen below, the mechanical properties of rapidly solidified alloys are rather disappointing, and so work has concentrated on the following topics: phase equilibria, microstructural development as a result of rapid solidification, mechanical properties and oxidation behavior, where rapid solidification is not the central interest. The results of these various studies are described below.

Phase Equilibria of Mg-Li-Si System

As stated above, there is little or no information available regarding phase equilibria in ternary Mg-Li-Si system. It has been speculated that Mg-Li-Si system may be similar to Mg-Li-Ge system⁽²⁹⁾. This speculation is based on the fact that both Si and Ge are in group IVB of periodic table. In order to understand the physical metallurgy of this alloy system it is necessary to be able to make reference to a ternary phase diagram of Mg-Li-Si system. An attempt has been made to draw a semi-quantitative ternary phase diagram of this system near the Mg corner. Development of this ternary phase diagram is based on optical microscopy, x-ray diffraction and DSC data.

In this study of the phase equilibria, the alloy compositions are chosen on the basis of binary Mg-Li phase diagram. The binary alloys of interest falls within the three principal phase fields, which are α -Mg, α -Mg + β -Li and β -Li. The optical micrograph of the as cast binary Mg-Li alloys are shown in Figure 17. Figure 17a shows the microstructure of Mg-5Li alloy consisting of a matrix of cph α -Mg phase with some bcc β -Li phase at the grain boundary area. The identity of the phases in the optical micrographs is established on the basis that the major phase (i.e. Mg based) in Figure 17a is light shaded, and moreover, there is a corrosive attack on the Li containing phase, which is dark shaded. Figure 17b is the microstructure of Mg-8Li alloy showing a divorced eutectic structure consisting of cph α -Mg phase, light shade and bcc β -Li phase, dark shade. Figure 17c shows the microstructure of Mg-12Li alloy with a matrix of β -Li phase. The small dark spots present in the microstructure of both Mg-8Li and Mg-12Li alloys are due to rapid corrosion of the β -Li phase. Si is added to these binary alloys to make the ternary alloys of interest. The optical micrographs of Mg-5Li-3Si, Mg-8Li-3Si and Mg-12Li-3Si alloys are shown in Figure 18, respectively. The optical microstructure of Mg-5Li-3Si alloy shows large particles of primary Mg₂Si phase and small particles of eutectic (binary) Mg₂Si phase present in a matrix of α -Mg. The as-cast microstructure of Mg-8Li-3Si alloy shows a divorced eutectic structure consisting of α -Mg and β -Li phases together with primary and eutectic (binary and ternary) Mg₂Si particles. The microstructure of Mg-12Li-3Si alloy shows a matrix of β -Li phase along with primary and eutectic (binary) Mg₂Si particles. The evolution of these microstructures is discussed in detail later with the help of the ternary phase diagram. The optical micrographs of Mg-Li alloys with 5 wt. % Si have already been published by Grensing(29).

Table 8 shows the various phases present in the binary and ternary alloys together with their lattice parameters. The identification of various phases and determination of their lattice parameters were carried out using XRD technique. It is interesting to note that the lattice parameter of Mg₂Si phase (determined by electron diffraction here to be 6.478 Å in the binary form) varies in an interesting way. Thus, it appears that in the presence of 3Si, the effect of Li is to reduce the lattice parameter at first, and then cause an increase with increasing Li content of the alloy; with 5Si alloys, the lattice parameters remain less than the binary value. This behavior is not understood at present, but the variation in lattice parameter is consistent at least with the solid solution of Mg₂Si containing some Li.

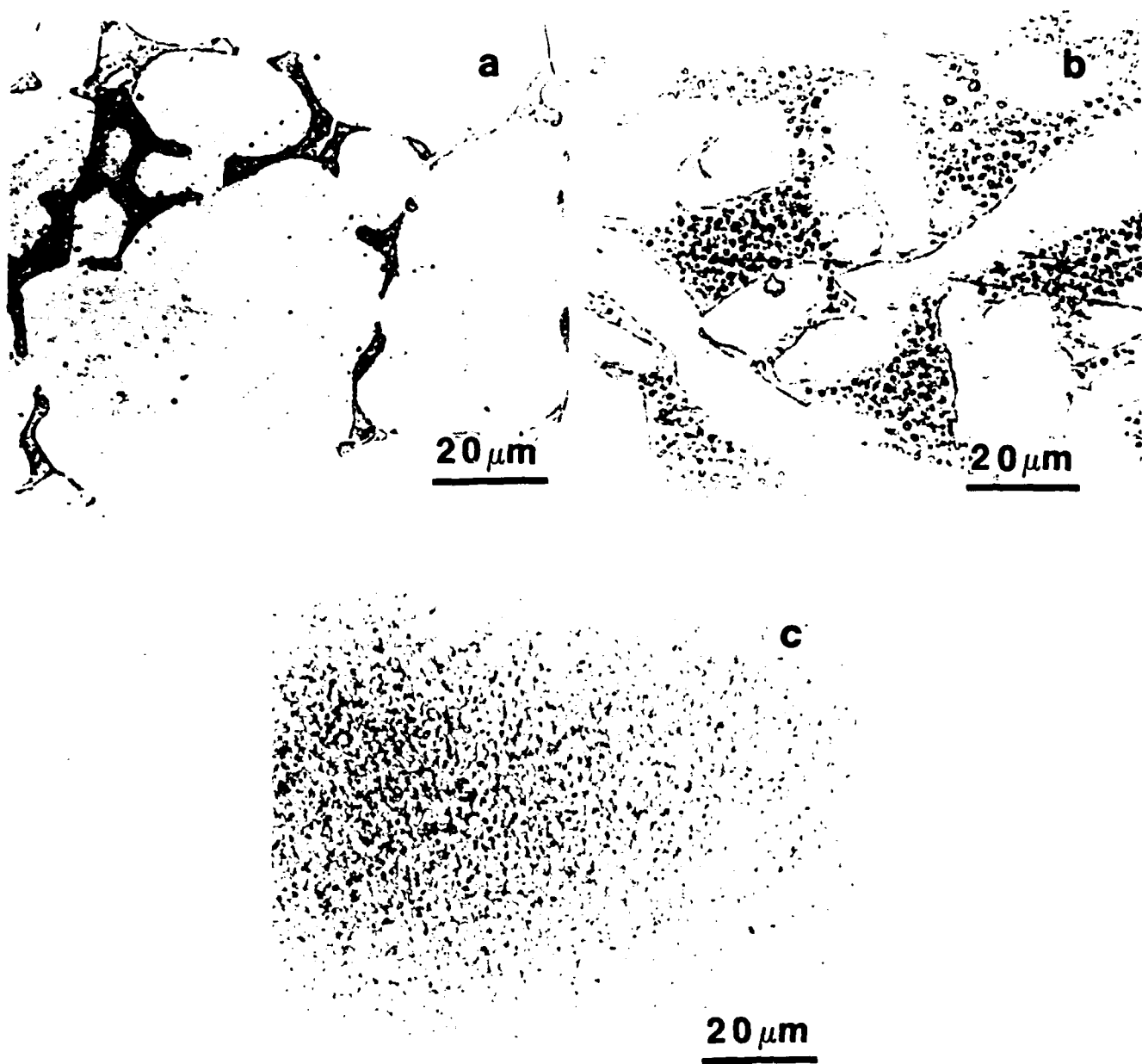


Figure 17. The optical micrographs of binary Mg-Li alloys of compositions a) Mg-5Li, b) Mg-8Li and c) Mg-12Li.

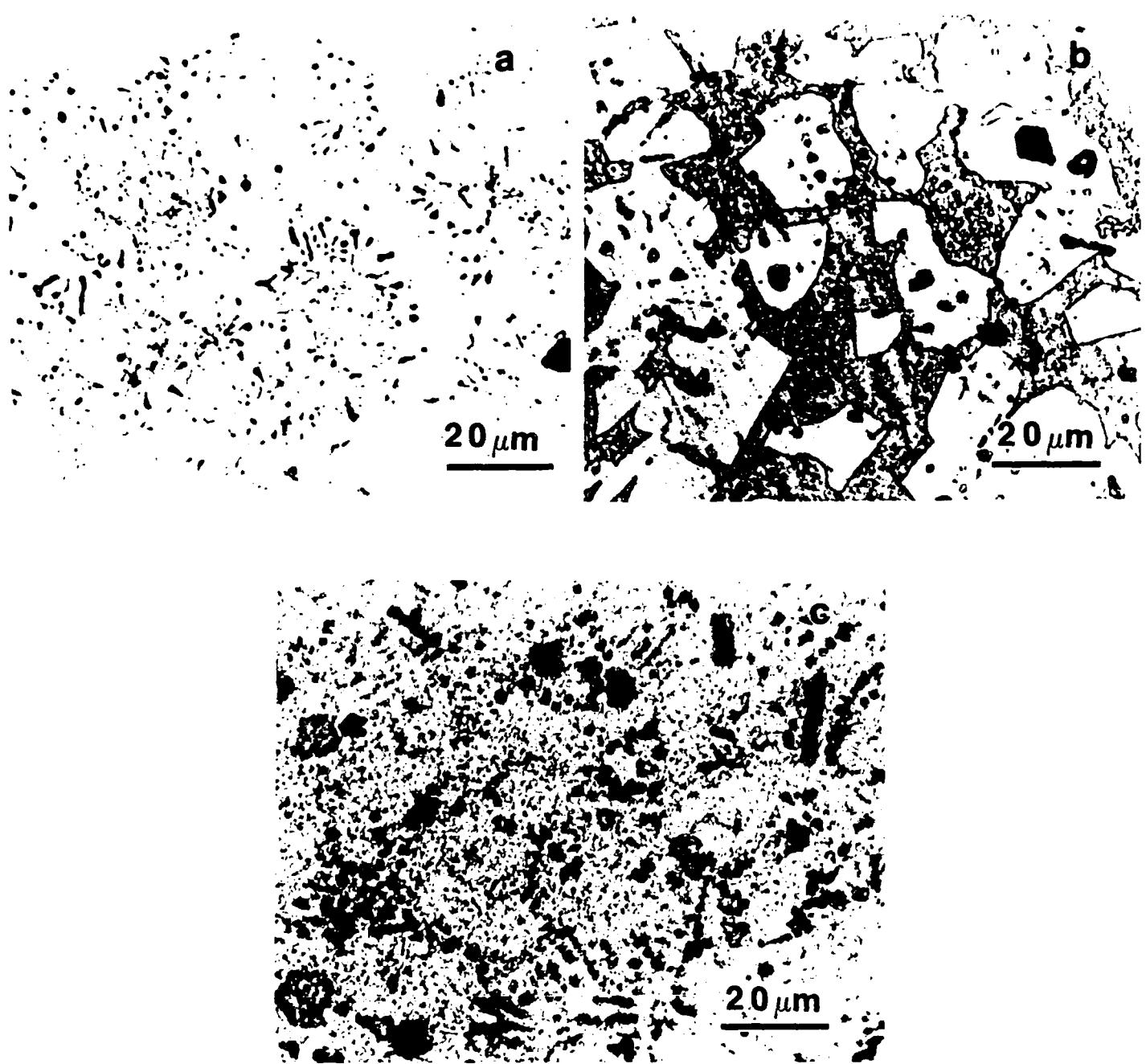


Figure 18. The optical micrographs of ternary Mg-Li-Si alloys of compositions a) Mg-5Li-3Si, b) Mg-8Li-3Si and c) Mg-12Li-3Si.

ALLOY	PHASE(S)	a (Å)	c (Å)	c/a
Mg-5Li	cph α -Mg	3.1970	5.1467	1.6099
Mg-8Li	cph α -Mg bcc β -Li	3.1705 3.5269	5.0902	1.6055
Mg-12Li	bcc β -Li	3.5168		
Mg-5Li-3Si	cph α -Mg CaF_2 type Mg_2Si	3.1929 6.2478	5.1352	1.6083
Mg-8Li-3Si	cph α -Mg bcc β -Li CaF_2 type Mg_2Si	3.0929 3.5306 6.5810	5.0355	1.6281
Mg-12Li-3Si	bcc β -Li CaF_2 type Mg_2Si	3.5269 6.6542		
Mg-5Li-5Si	cph α -Mg CaF_2 type Mg_2Si	3.1909 6.3491	5.1467	1.6129
Mg-8Li-5Si	cph α -Mg bcc β -Li CaF_2 type Mg_2Si	3.1991 3.5713 6.3317	5.2170	1.6308
Mg-12Li-5Si	bcc β -Li CaF_2 type Mg_2Si	3.5195 6.4063		

Table 8. Various phases present in the binary and ternary alloys together with their lattice parameters.

Table 9 presents the DSC data of Mg-xLi-3Si alloys. These values represent the temperatures where the respective alloys start melting. These temperatures may be compared to the melting temperatures of binary Mg-Li alloys, of the same Li compositions as those given in the Table, determined using the binary phase diagram. From this, it is clear that these values are very similar to those for the binary alloys with the same amount of Li as the ternary alloys. Therefore, one may conclude that the effect of Si on the transformation temperatures of Mg-Li alloys is not significant.

ALLOY	TEMPERATURE WHERE MELTING STARTS (°C)
Mg-5Li-3Si	594
Mg-8Li-3Si	588
Mg-12Li-3Si	589

Table 9. DSC data of ternary Mg-Li-Si alloys showing the temperatures where melting starts.

On the basis of this information, attempts have been made to draw a semi-quantitative ternary phase diagram of Mg-Li-Si system near the Mg corner. Figure 19 shows the binary eutectic valleys and the primary phase fields of Mg-Li-Si phase diagram. From Figure 19 it is clear that all the six alloy compositions of our interest fall within the primary Mg₂Si phase field. The optical micrographs of all these six alloys reveal the presence of primary Mg₂Si particles. During solidification the composition of the liquid changes continually along a line connecting the alloy composition point and the point showing the composition of Mg₂Si phase. Now the solidification paths of various alloys will be discussed as follows:

Mg-5Li-3Si and Mg-5Li-5Si alloys: At first, primary Mg₂Si particles will start solidifying until the liquid composition reaches the eutectic valley AB. Then the following binary eutectic reaction starts taking place:



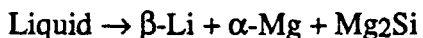
The liquid composition changes continually along AB towards B. The binary eutectic

reaction as mentioned above continues until the liquid composition reaches the point B. For these alloys the solidification reaction completes before the liquid composition reaches the point B. Therefore no ternary eutectic reaction takes place. The optical microstructure shows the presence of both primary and eutectic (binary) Mg₂Si particles in the matrix of α -Mg. No lamellar eutectic structure is visible due to very small amount of Mg₂Si phase compared to the amount of α -Mg phase. The amount of α -Mg or Mg₂Si can be determined by using the lever rule.

Mg-8Li-3Si and Mg-8Li-5Si alloys: At first primary Mg₂Si particles start to solidify. Then the liquid composition reaches the binary eutectic valley AB, where the following reaction starts taking place:

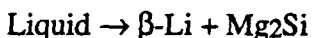


During such a reaction the liquid composition changes continually along AB towards B. The above mentioned binary eutectic reaction continues until the liquid composition reaches the ternary eutectic point B where the following ternary eutectic reaction takes place:



The optical microstructure clearly shows a divorced eutectic structure. This is presumably due to a problem concerning nucleation of one of the phases.

Mg-12Li-3Si and Mg-12Li-5Si alloys: At first, primary Mg₂Si particles solidify until the liquid composition reaches the binary eutectic valley DB where the following reaction takes place:



This binary eutectic phases are not lamellar because of very small amount of Mg₂Si compared to that of β -Li. The liquid composition changes continually along DB towards B. The binary eutectic reaction continues until the liquid composition reaches the point B. For these alloys solidification is completed before the liquid composition can reach the point B. Therefore, no ternary eutectic reaction takes place for this alloy. The optical micrographs of these alloys show the presence of primary and eutectic (binary) Mg₂Si particles present in β -Li matrix.

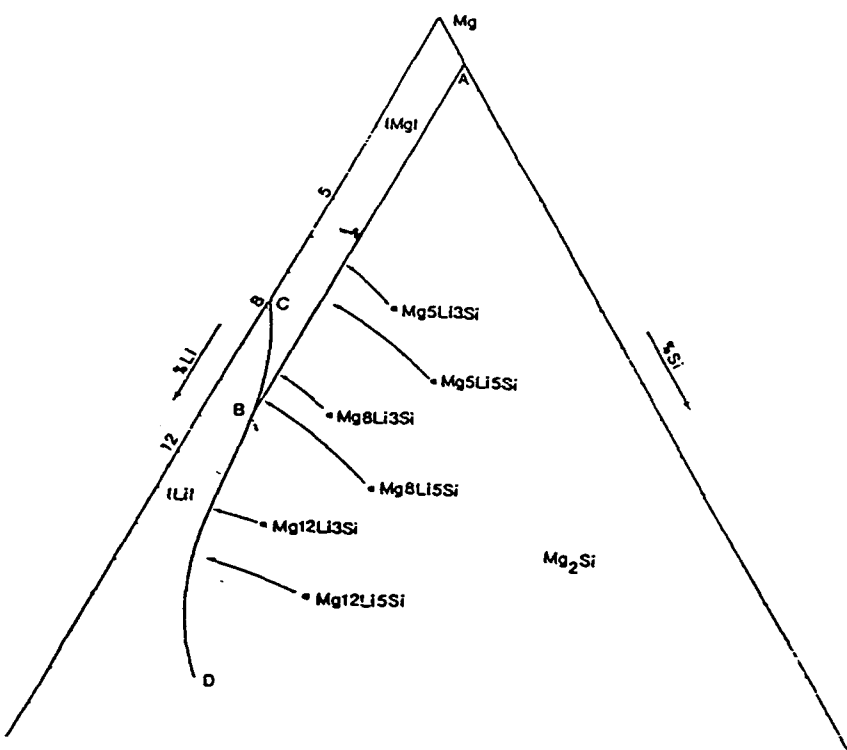


Figure 19. The Mg corner of the ternary Mg-Li-Si phase diagram showing the binary eutectic valleys and the primary phase fields.

Figure 20 shows an isotherm from a temperature just above the ternary eutectic point but below all the binary eutectic points. Various phase fields present at that temperature are indicated on the diagram. The ternary eutectic temperature is at approximately 588°C. Therefore, the binary eutectic valley CB is almost horizontal.

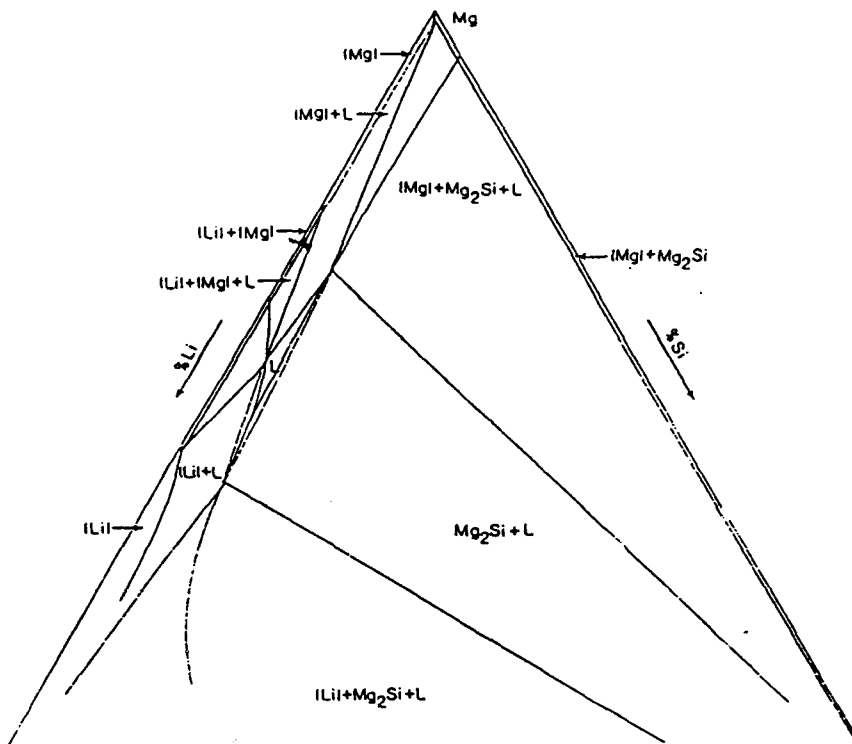


Figure 20. An isotherm, near the Mg corner of the Mg-Li-Si ternary phase diagram, taken from a temperature just above the ternary eutectic points. The binary eutectic valleys are also indicated on the diagram.

Figure 21 shows the various phase fields present at room temperature. From Figure 21 it is clear that only Mg-8Li-3Si and Mg-8Li-5Si alloys fall within the three phase region, α -Mg + β -Li + Mg₂Si. Therefore they are the only alloys which show a ternary eutectic structure. Mg-5Li-3Si and Mg-5Li-5Si alloys fall in the two phase fields of α -Mg + Mg₂Si. In contrast, the ternary alloys with 12 wt.% Li fall in the two phase fields of β -Li + Mg₂Si.

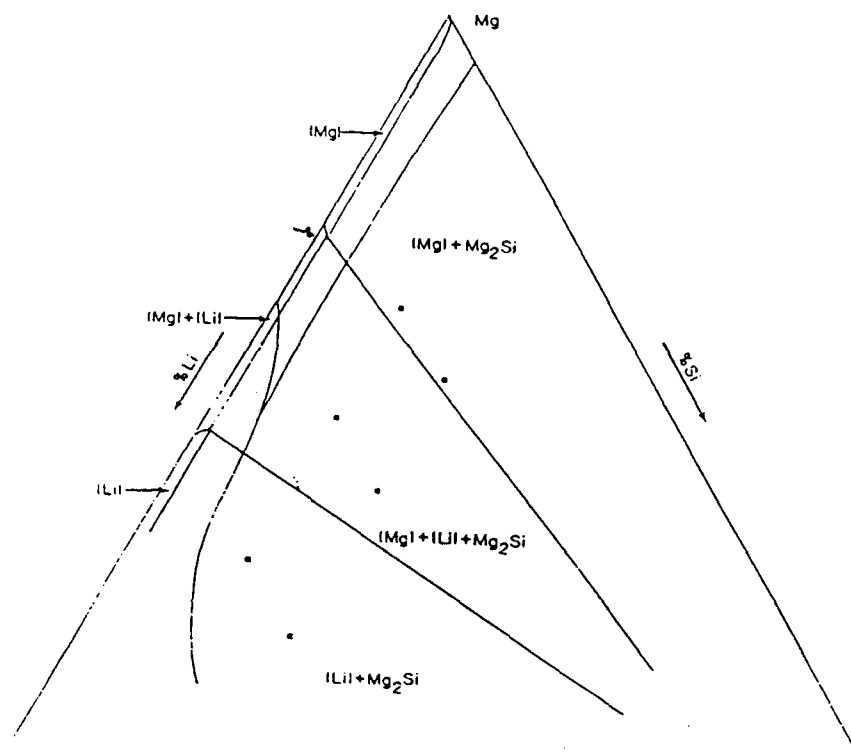


Figure 21. The Mg corner of the Mg-Li-Si ternary phase diagram showing various phase fields present at room temperature. The binary eutectic valleys are also indicated.

Microstructures of Rapidly Solidified Mg-Li-Si Alloys

The alloys studied have been chosen on the basis of past work on the rapid solidification of Al-transition metal alloys, where it has been established that a coupled growth morphology may be effected in hyper-eutectic alloys of certain compositions(30). These microstructures are very attractive from the point of view of mechanical properties, and it is of both scientific and technological interest to investigate whether such structures may be effected in Mg-Si alloys to which Li is added to reduce the density. Therefore, the microstructures of rapidly solidified Mg-Li-Si alloys have been studied. It is interesting to note that the microstructures of rapidly solidified

binary Mg-Si alloys are very similar to those of Al-transition metal alloys⁽³⁰⁾, and the mechanism of formation of the various microstructures in Mg-Si alloys has been described on the same basis as that in these Al alloys^(29,30). Thus, a metastable phase diagram is constructed based on the equilibrium Mg-Si phase diagram⁽²⁹⁾; the Mg-Si equilibrium phase diagram shows an eutectic point and temperature of 1.16 wt.% Si and $\approx 638^{\circ}\text{C}$, respectively (see Figure 22 (31)). Figure 23 shows the appropriate metastable Mg-Si phase diagram (29). The solidification sequences for alloys which are rapidly cooled depends on the degree of undercooling achieved in a given volume of liquid alloy. Thus, the undercooling produced by rapid extraction of heat tends to suppress nucleation of the intermetallic phases involved in the phase equilibria for hyper-eutectic alloys, this being due in part to the difficulty in nucleating such faceted phases. For hyper-eutectic alloys, if the liquid is undercooled below the extended α -Mg (in this case) liquidus, thermodynamically the α -phase may nucleate. Of course, some further kinetic undercooling is necessary before nucleation occurs. Nucleation of the α -phase, which in these conditions of rapid heat extraction is normally supersaturated, results in the enrichment of the solute concentration in the liquid. This encourages subsequent nucleation of the intermetallic phase, and depending on the relative growth rates of the two phases, a coupled eutectic may form. In this way, one can construct a metastable "phase field" corresponding to a region of coupled growth, which is asymmetrically skewed in composition

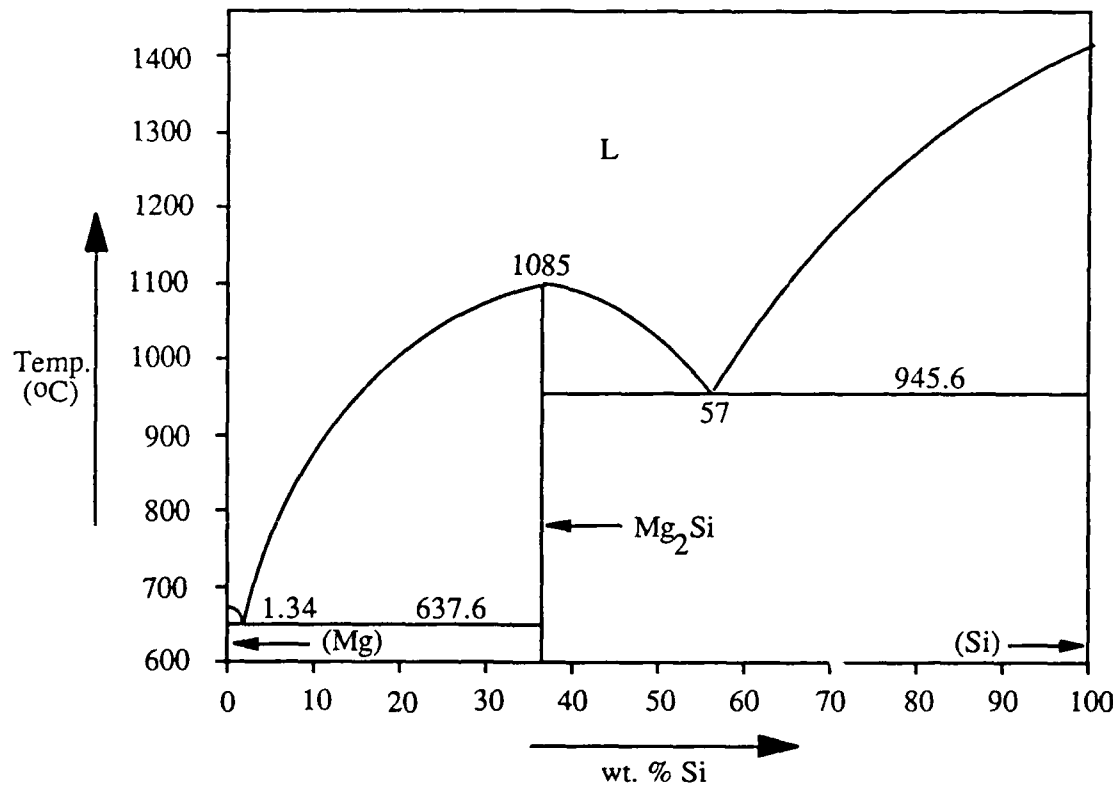


Figure 22. The equilibrium Mg-Si phase diagram.

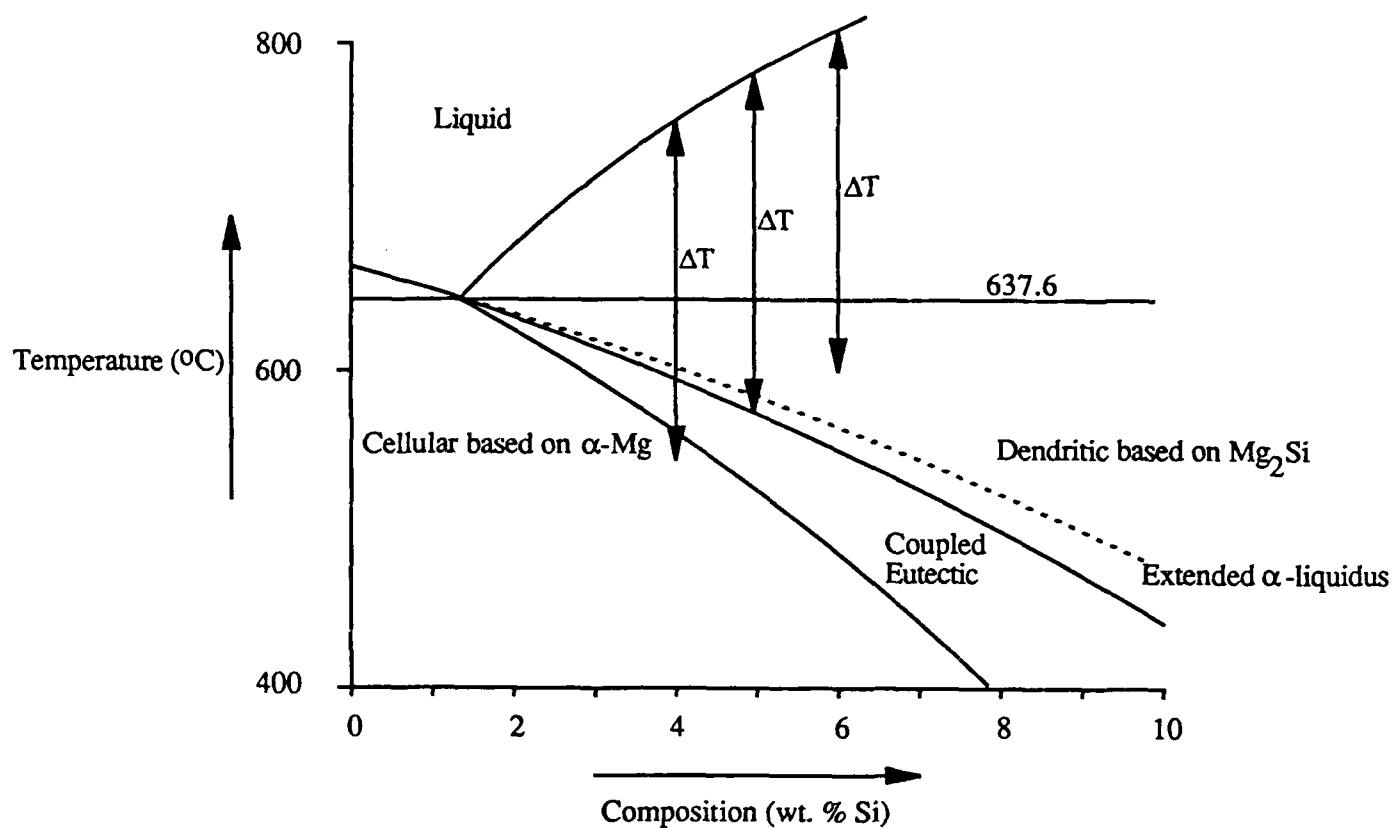


Figure 23. The metastable Mg-Si phase diagram showing a skewed coupled eutectic region.

toward the intermetallic phase, as shown in Figure 23. If a liquid alloy is undercooled into this region, a coupled growth morphology is expected to result. When nucleation occurs in the liquid, latent heat of fusion is liberated by the growing solid, and this will tend to cause recalescence in the remaining liquid, and for continued growth of a coupled morphology, the rate of extraction of heat must balance the rate of heat given off by fusion; although this appears to be a difficult task, in the case of melt-spun ribbon of Mg-Si alloys, this is achieved in ribbons which have thicknesses $\leq 20\mu\text{m}$.

Grensing and Fraser studied the microstructures of a series of melt spun Mg-Si alloys⁽³²⁾. Their results show that a coupled eutectic structure can be obtained in a melt spun ribbon containing 5 wt.% Si, which has about four times more Si than the equilibrium eutectic composition. These authors found a coupled eutectic structure only in a melt spun ribbon containing 5 wt.% Si. Since the processing condition is similar for all the alloys studied, the potential degree of undercooling achieved for each alloys can be considered to be fairly equivalent. Let us assume that an amount of undercooling, ΔT , may be achieved. It is known experimentally

that the 5 wt.% Si containing alloy gives a coupled eutectic morphology. Therefore, the quenching from the liquidus by an amount of ΔT will cause complete solidification reaction in the coupled region, as shown in Figure 23. Now consider the alloy containing 3 wt.% Si.; an undercooling of this alloy melt by an amount of ΔT will cause the solidification reaction in the primary α -Mg phase field, as indicated in Figure 23 and no coupled eutectic is expected to form. Similarly, for 6 wt.% Si containing alloy an undercooling by an amount of ΔT will cause solidification in the primary Mg_2Si phase field. Therefore to form a coupled eutectic structure it is necessary to effect solidification at a temperature corresponding to the coupled eutectic region. The solidification paths 1 and 2, as shown in Figure 24, will not cause the formation of a eutectic. These two paths will result in the formation of dendrites or cells of α -Mg or Mg_2Si , respectively, with a possibility of a coupled eutectic forming in the interdendritic (cellular) regions.

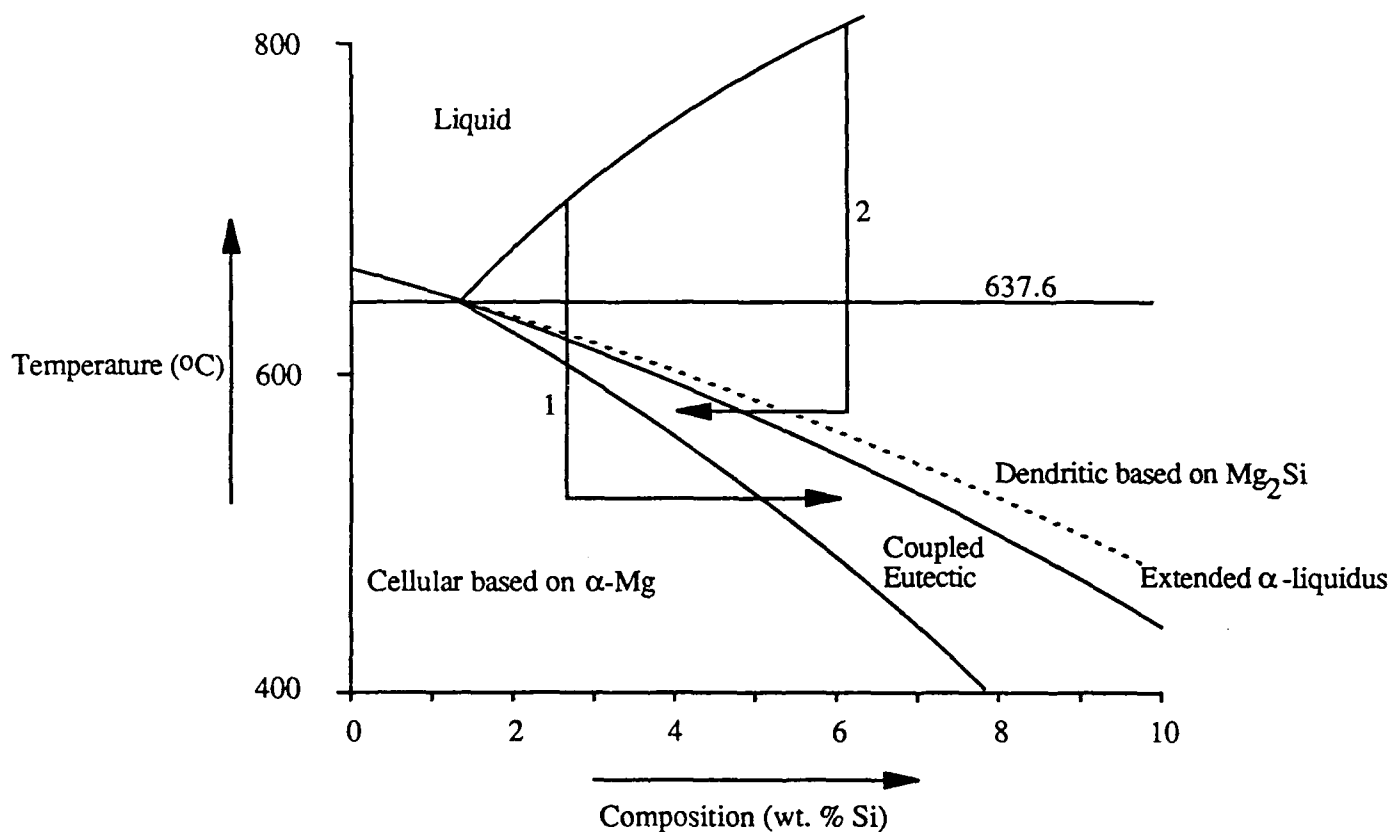


Figure 24. The metastable Mg-Si phase diagram showing various solidification path which do not produce a fully coupled eutectic structure.

Grensing made a preliminary study of the microstructure of Mg-Li-Si alloys⁽²⁹⁾; of particular interest was the effect of various amounts of Li on the microstructure of Mg-5Si alloy, since a coupled eutectic morphology could be produced for this alloy composition, as described

above. In fact, no coupled eutectic was observed in any Li containing alloy. A central question concerns the rôle of Li on the solidification sequences of rapidly solidified Mg-Si alloys, and this is studied as part of the present work. The fact that a coupled eutectic does not form in the lithium containing alloys based on Mg-5Si when rapidly solidified implies that an insufficient degree of undercooling was developed to maintain the temperature of the liquid in the coupled growth region during solidification. This is consistent with Li acting in such a way as to reduce the eutectic temperature and shift the eutectic point to a more dilute concentration of Si. Thus, with reference to Figure 25, it may be seen that if such modifications to the eutectic temperature and composition occur, then the degree of undercooling for coupled growth in a 5Si alloy, for example, becomes significantly larger than in the case of the binary. Justification to support these modifications may be obtained as follows. Firstly, the effect of Li is to reduce the melting point of α -Mg, as may be seen by reference to the binary Mg-Li phase diagram (Figure 26). Therefore, it is expected that the eutectic temperature will be reduced accordingly. This is supported by work involving DSC, where it has been shown that the eutectic temperature in as-cast Mg-Li-Si alloys is $\approx 588^\circ\text{C}$, compared to 638°C for the Mg-Si binary system, see Table 9. This is supported by the work described earlier in this thesis concerning the phase equilibria of the Mg-Li-Si system. If the presence of Li does not alter the slope or position of the Mg_2Si liquidus, then a slight change in the eutectic composition is expected, and has been estimated to be $\approx 1\%$ Si. If, on the other hand, Li reduces the melting point of the intermetallic compound, Mg_2Si , and so modifies the liquidus curve, then a smaller change

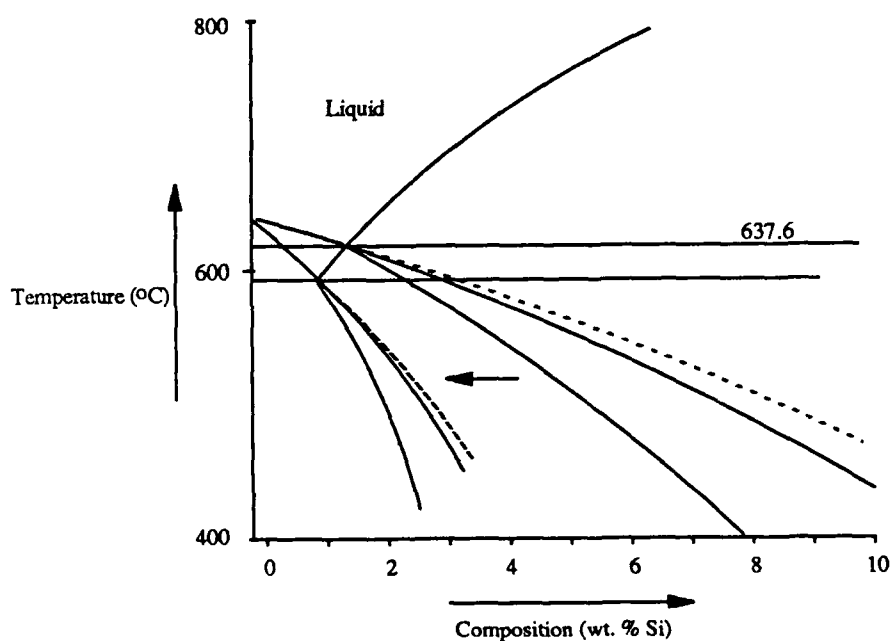


Figure 25. The predicted effect of Li on the metastable Mg-Si phase diagram.

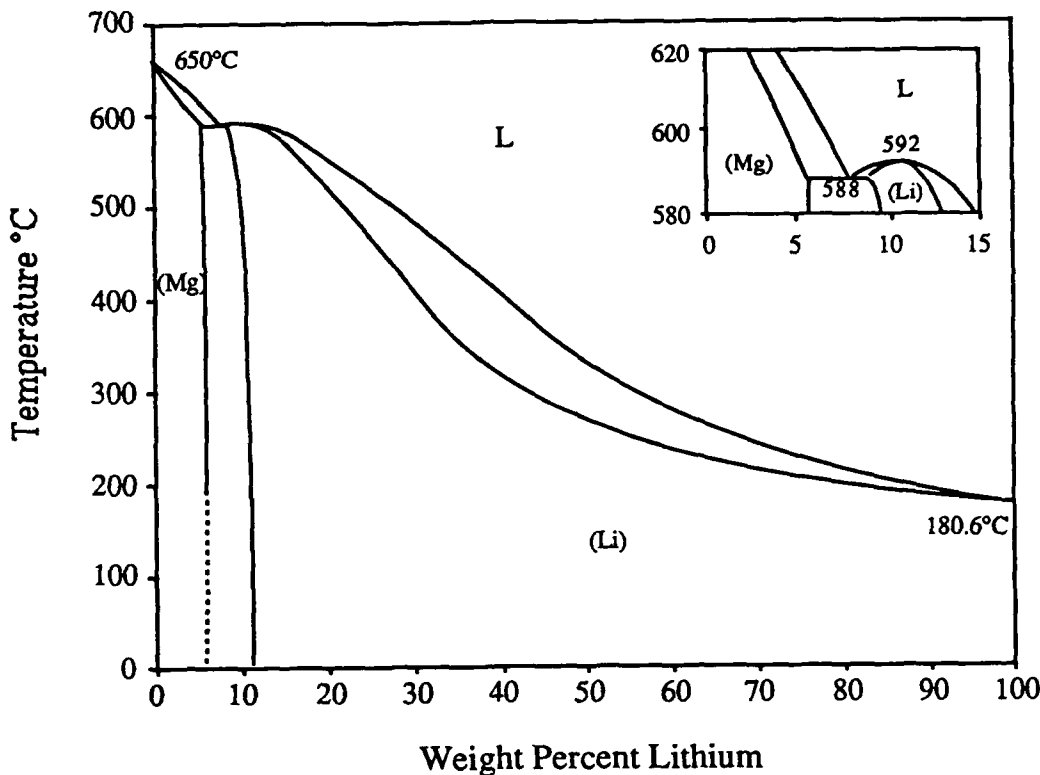


Figure 26. The equilibrium phase diagram of Mg-Li system.

in the eutectic composition is expected. It has not been possible in the present work to estimate these possible modifications to the Mg₂Si liquidus, but in any case on the basis of the arguments given above, it is expected that this change in the eutectic composition will be less than 1% Si. It is possible then, on the basis of Figure 25, to expect that a significantly increased undercooling is required to effect a coupled eutectic morphology in Mg-5Si alloys containing Li. However, if more dilute Mg-Si alloys are employed in these experiments, then the degree of undercooling may be sufficient to permit solidification to occur in the region of coupled growth. To validate this prediction, alloys of Mg-Li-Si with a Si content of 3% have been reduced to ribbon by melt-spinning, and the results of these experiments are detailed below.

Figures 27 and 28 show the transmission electron micrographs of melt spun Mg-xLi-3Si alloys. Figure 27 shows a coupled eutectic structure present in the Mg-5Li-3Si alloy, which consists of rods of Mg₂Si in the matrix of hexagonal α -Mg. It is interesting to note that such a coupled eutectic structure can only be seen in the thin region of the foil. These samples used for electron microscopy studies have been prepared by ion milling but the thinnest regions of the foils correspond to the thin pieces of ribbon, which are subjected to the most rapid rate of heat

extraction. Therefore, the liquid alloy in these regions will have experienced the largest degrees of undercooling, and so a coupled eutectic may form in these hyper-eutectic alloys. Similar coupled eutectic structure can be seen in melt spun ribbons of Mg-8Li-3Si and Mg-12Li-3Si alloy. It is important to note that the coupled eutectic structure occurs only in the thin regions of the ribbon which experience large undercoolings. In the thick region of the foil a cellular microstructure can be observed presumably due to insufficient amount of undercooling. This cellular structure consists of cells of cph α -Mg phase with Mg₂Si particles at the grain boundary region. Figure 28 shows the presence of both cellular and coupled eutectic regions in a relatively thicker region of the ribbon of Mg-12Li-3Si. All the alloys show a similar type of coupled eutectic structure in the thin regions of the ribbons, and α -Mg cellular dendrites in the thick areas; no β -Li has been observed, despite the fact that for some of the concentrations of Li used, such a phase would be expected. This surprising result has been attributed to loss of Li during processing. The basic difference between these various types of structure lies in their differences in lattice parameters. Table 10 shows the difference in lattice parameters of the matrix of melt spun ribbons of Mg-5Li-3Si and Mg-8Li-3Si. Mg-8Li-3Si ribbon has a lower c/a ratio than that of Mg-5Li-3Si ribbon. Therefore, the effect of Li is to decrease the c/a ratio of the hexagonal matrix, as would be expected.

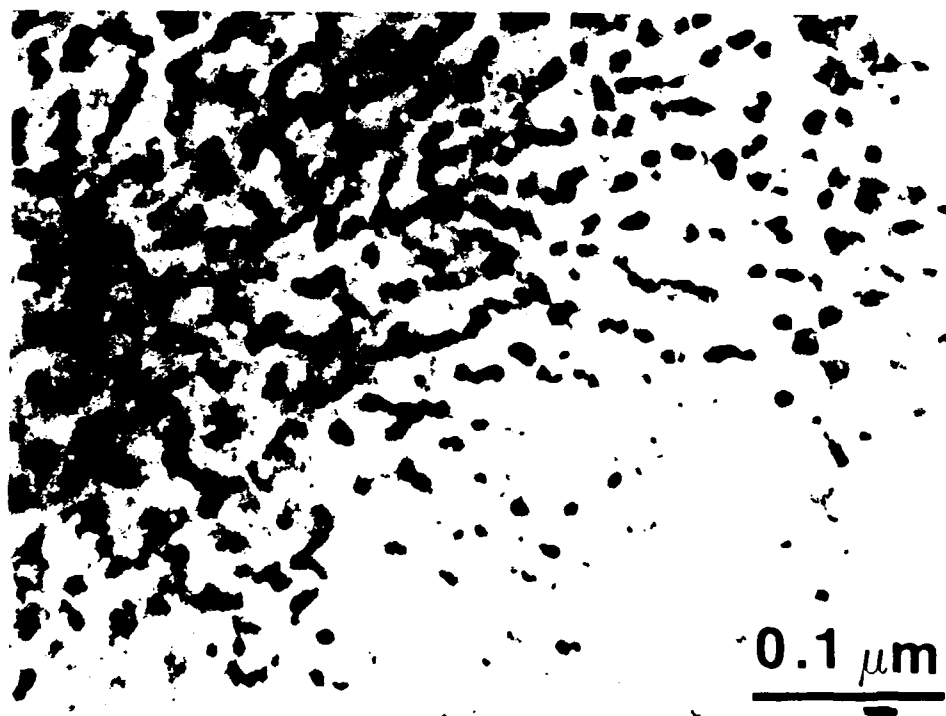


Figure 27. The transmission electron micrograph of melt-spun Mg-5Li-3Si ribbon showing a coupled eutectic structure consisting of rods of Mg₂Si in the matrix of cph α -Mg.

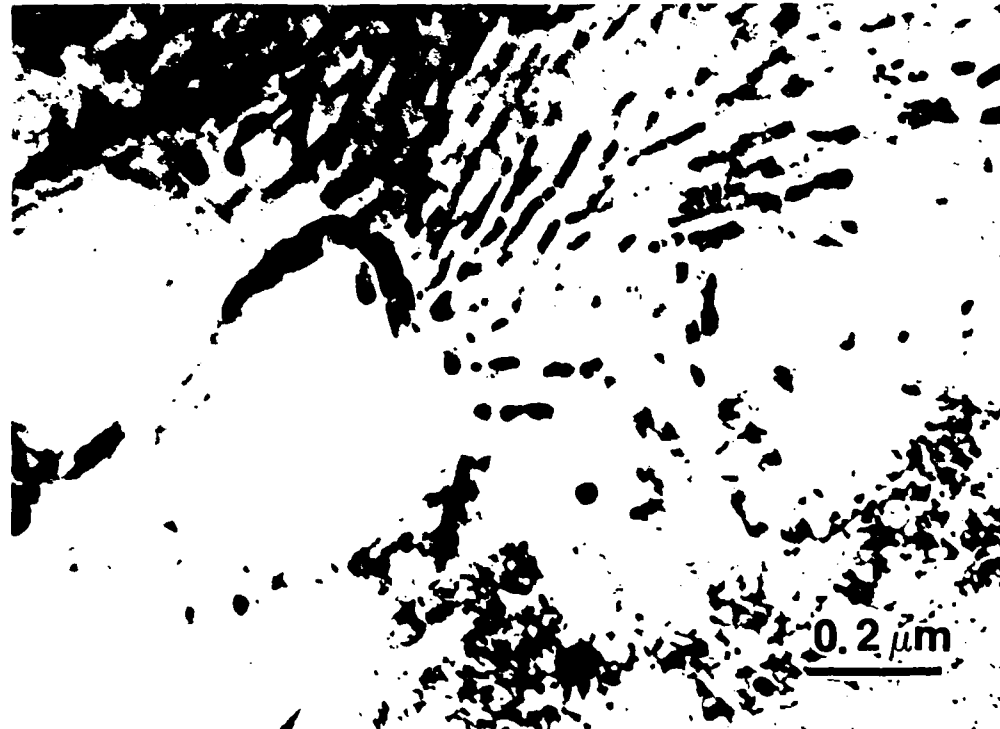


Figure 28. The transmission electron micrograph of melt spun Mg-12Li-3Si ribbon showing the presence of both cellular and coupled eutectic structure present in the thicker region of the ribbon.

ALLOY	PHASE(S)	a (Å)	c (Å)	c/a
Mg-5Li-3Si (Melt Spun Ribbon)	cph α -Mg	3.1991	5.1698	1.6160
Mg-8Li-3Si (Melt Spun Ribbon)	cph α -Mg	3.1970	5.1582	1.6135

Table 10. The difference in lattice parameters of the matrix of melt-spun ribbons of Mg-5Li-3Si and Mg-8Li-3Si alloys.

The thin regions of all the melt spun ribbons of these dilute Mg-Li-Si alloys exhibited a coupled eutectic structure. These observations are consistent with the predictions made on the basis of Figure 25. The microstructural development that occurs when Mg-Li-Si alloys are rapidly solidified is now well understood, and consistent with the development of microstructures of rapidly solidified other Al and Mg alloys of hyper-eutectic composition.

Tensile Properties of Rapidly Solidified Materials

The study of microstructural development of rapidly solidified Mg-Li-Si alloys has shown that it is possible to obtain a coupled growth morphology in melt-spun ribbons providing the Si content is held at \approx 3wt.%. This morphology is attractive from the point of view of mechanical properties, and so it is of interest to assess these properties. However, as stated above, this morphology was only observed in thin ribbons and so it is difficult to ensure that pieces of rapidly solidified alloys possess only this microstructure in the "gauge sections" of the test samples. Consequently, great care was taken to choose ribbon that appeared to maximize the volume fraction of the coupled growth microstructure; also, laser surface melted materials were used to assess the mechanical properties, as the microstructures of these samples were fairly uniform. Laser surface melted samples have also been used; although the microstructural variations observed in the ribbons are not repeated in the laser surface melted samples, presumably because of the shortness of the heating pulse resulting in incomplete melting of the particles of Mg₂Si, these samples permit a determination of the effect of Li on the strength of these alloys.

At first, pieces of melt-spun ribbon were tested in tension. Since these ribbons possess many defects, it is possible only to obtain the fracture strength of these types of samples. Table 11 shows the fracture strength of various melt spun ribbons. Some melt spun ribbons of binary Mg-Si alloys are also tested in order to develop a better understanding of the fracture behavior of ternary alloys of Mg-Li-Si. This is particularly helpful to understand the effect of lamellar eutectic structure on the fracture mode of this type of materials. It should be noted at first that all the fracture strengths listed in Table 11 are lower than that expected for pure Mg. Indeed, the alloy expected to give useful mechanical properties, i.e. Mg-5Si with a fully eutectic microstructure, yielded a lower fracture strength value than those of the Mg-3Si ribbon, which possesses a cellular microstructure. It may be argued that this is a result of defects in the ribbon, but may also be due to decohesive rupture along the lamellae interface. This may be resolved in part by inspection of the fracture surfaces using scanning electron microscopy. Thus, examples of fractographs of the tested Mg-5Si ribbons are presented in Figure 29. The failure may be fluted, and therefore somewhat brittle in nature, as shown in Figure 29. To compare the fracture behavior of alloys not possessing the coupled eutectic microstructure, the surfaces of Mg-3Si fractured

ALLOY	FRACTURE STRENGTH (M Pa)
Mg-3Si	150
Mg-5Si	92
Mg-5Li-3Si	114
Mg-8Li-3Si	171

Table 11. Fracture strength of various melt spun ribbons.

ribbons have been studied. An example of a fractograph taken from the surfaces of these ribbons is shown in Figure 30. As can be seen, the fracture surface is dimpled implying increased ductility compared to the case of the 5% alloy; the fracture surface is not fluted, but some evidence of quasi-cleavage failure is present. It appears then that the coupled eutectic microstructure may indeed be prone to brittle failure. However, it is not possible at this time to resolve whether this behavior is typical of this microstructure, or whether large stress concentrations from defects in the ribbons are responsible for the mode of failure.

The ribbons of Mg-8Li-3Si alloy show higher fracture strengths than those of the ribbons of Mg-5Li-3Si. This is probably due to the higher Li content of this alloy. The effect of Li on the mechanical properties of Mg is not well understood. Li is known to decrease the c/a ratio of hexagonal α -Mg matrix of these alloys, and so slip of dislocations with Burgers vectors (b) given by $b=1/3<11\bar{2}0>$ is expected to occur more easily on the prism ($\{10\bar{1}0\}$) and pyramidal ($\{10\bar{1}1\}$) planes, as well as on the basal planes. This should lead to an increased ease of slip accommodation at grain boundaries during plastic flow of these materials. This reasoning is consistent with the result that ribbons of Mg-8Li-3Si show higher fracture strength than that of the ribbons of Mg-5Li-3Si. The principal difference between the fracture modes of Mg-8Li-3Si and Mg-5Li-3Si ribbons is the presence of much lower amount of quasi-cleavage facets in Mg-8Li-3Si. Therefore one can infer that Li is acting in a way to increase the deformability of Mg-8Li-3Si ribbons compared to that of Mg-5Li-3Si ribbons, and this is presumably due to the increase in slip activity.

45



Figure 29. The SEM fractograph taken from the tensile sample of Mg-5Si showing a brittle failure.



Figure 30. SEM fractograph taken from the tensile sample of Mg-3Si MSR showing a mixture of both ductile and brittle failure.

A comparison of the effect of Li on the mechanical properties of these alloys may be obtained from a consideration of tensile tests on samples cut from laser surface treated materials. Table 12 shows the tensile strengths of laser surface melted (LSM) pure Mg and various binary Mg Li and ternary Mg-Li-Si alloys, together with that of the alloy K1A-F, a very dilute casting alloy (containing 0.7Zr)(33). Three specimens were tested for each alloy and average values are reported, and stress values were calculated from the undeformed specimen dimensions. The sample geometry was chosen such that the stress-concentrations arising from this factor was less than ≈ 1.0 . Yield strengths calculated correspond to a 0.2% offset strain from initial linear deformation. The length of the hour-glass section ($\sim 15\text{mm}$) was employed as the gauge length for this approximate calculation. If this amount of plastic strain was not observed, only the ultimate strength is reported in the table. It is interesting to note that the pure Mg sample following laser surface melting does not exhibit a region of plastic strain, but breaks before yielding. In terms of .

yield stresses, four of the alloys exhibited yield stresses, and these may be compared to that of the casting alloy, K1A-F. As can be seen, all the alloys are stronger than this simple Zr containing alloy. The highest and lowest yield strengths exhibited by alloys in the present study both contain 12Li; in the case of the weaker alloy, namely the binary Mg-12Li, the structure is (or should be) bcc, and may therefore exhibit lower strength. When Si is present, the Li is thought to be dissolved in the Mg₂Si particles present in the microstructure, and therefore the structure may contain some cph phase. Of course, it is possible that a solidification defect has effected the present results. In any case, the effect of Li on the yield stress of Mg is demonstrated, a significant increase being observed for each alloy. The strengthening effect of Li in these alloys is most likely due to a grain size effect; the value reported for K1A-F corresponds to the as-cast condition, and therefore rather large grains, whereas in the rapidly solidified condition the microstructure is very refined. Alloys with the hcp structure are most likely to exhibit relatively strong Hall-Petch effects, and realize significant strength from a refinement of microstructure. The value of k (material constant) calculated from the Hall-Petch equation is ≈0.17 for these binary Mg-Li alloys.

ALLOY	σ_u (M Pa)	σ_y (M Pa)
Mg	192	
Mg-5Li	156	115
Mg-8Li	161	136
Mg-12Li	108	78
Mg-5Li-3Si	170	
Mg-8Li-3Si	191	
Mg-12Li-3Si	159	140
Mg-5Li-5Si	172	
Mg-8Li-5Si	108	
Mg-12Li-5Si	166	
Alloy K1A-F (0.7 % Zr)	180	55

Table 12. The tensile strengths of laser surface melted (LSM) pure Mg and various binary Mg-Li and ternary Mg-Li-Si alloys, together with that of the alloy K1A-F, a very dilute casting alloy (containing 0.7Zr)(33).

In summary, it appears that the microstructure of all alloys studied could not be produced in a sufficiently homogeneous manner, and also the size of the Mg₂Si particles could be maintained below that necessary for improvement of the tensile properties. Thus, the tensile strengths of the Si containing alloys are reduced compared to expectation based on pure Mg, and this has been attributed to decohesion between Mg₂Si and the matrix, and also to brittle failure of larger particles of Mg₂Si.

Oxidation Behavior of Some Mg Alloys

The literature review on the oxidation behavior of Mg alloys reveals that not much work has been done in this field, especially on Mg-Li alloys. An attempt has been made here to understand the mechanism(s) of oxidation in various as cast Mg-Li and Mg-Li-Si alloys.

Thermogravimetric Analysis (TGA)

The oxidation behavior of these alloys has been studied by thermo-gravimetric analysis. Figure 31 shows the results of these experiments for some binary Mg-Li alloys, where the change of weight per unit area is plotted as a function of time for oxidation at 300°C. From Figure 31, it is clear that Mg-5Li and Mg-8Li alloys oxidize very rapidly; their oxidation behavior is almost linear. The physical examination of these two oxidized samples reveals that they have been oxidized completely. It has also been observed that the oxide layer was fractured in several layers parallel to the surface and spalled off to some extent. It would be tempting to speculate that it is the Li which is principally responsible for the poor oxidation property of these alloys, but the oxidation behavior of Mg-12Li alloy is not consistent with such speculation. Indeed, it seems that the microstructure of these alloys may have more effect on the oxidation behavior than the presence of Li. Thus, the optical micrographs of these alloys reveal that only Mg-12Li alloy has a single phase structure of b-Li. Mg-5Li and Mg-8Li alloys exhibit a two phase microstructure, the more dilute alloy consisting of a matrix of α -Mg with a small amount of β -Li in the grain boundary area. In contrast, the Mg-8Li alloy has a divorced eutectic structure consisting of grains of α -Mg and β -Li. From the TGA data shown in Figure 31, it is clear that a single phase microstructure offers superior oxidation resistance than the two phase microstructure. This may be due to the difference in thermal expansion coefficient of the two phases and the oxidation rate of two different phases. This perhaps causes the spalling and the cracking of the oxide layer leading to a very high rate of oxidation. A strong and adherent layer of oxide is required to slow down the oxidation rate, which appears to be characteristic of the oxide layer that forms on the Mg-12Li since no spallation occurred.

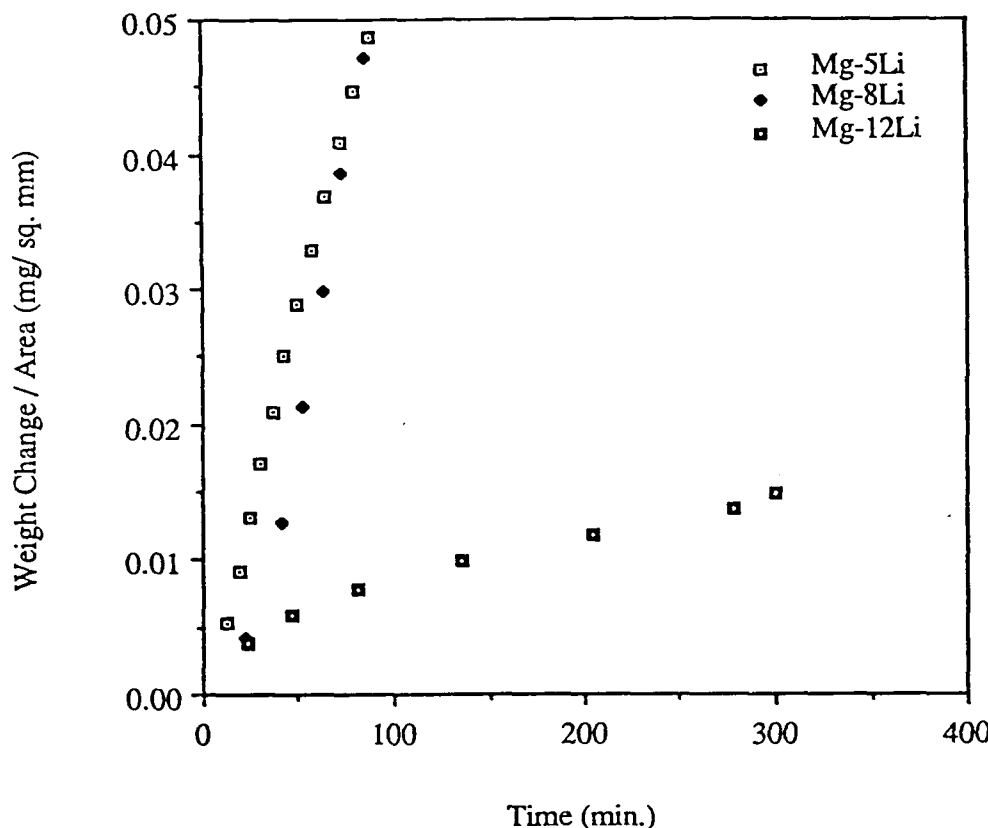


Figure 31. The weight gain versus time data, obtained for the oxidation of some binary Mg-Li alloys at 300°C.

Figure 32 shows results of thermo-gravimetric experiments which permit the oxidation behavior of some ternary alloys of Mg-Li-Si to be assessed. The kinetics of oxidation is of a parabolic nature. In contrast to Mg-5Li and Mg-8Li alloys, these ternary alloys develop a strong and adherent oxide layer, since no sign of oxide spallation is evident. This result can also be explained in terms of the effect of microstructure. Si in Mg results in the formation of Mg₂Si particles. The shape of many Mg₂Si particles are like Chinese Script. These Mg₂Si particles effectively key the oxide layer and thus prevent spalling. This keying effect is similar to the pegging effect of Hf in many superalloys. One interesting thing is that the effect of increasing Li content in the ternary alloys is to increase the rate of oxidation. This is probably due to the diffusion of Li from the metal towards the metal-oxide interface.

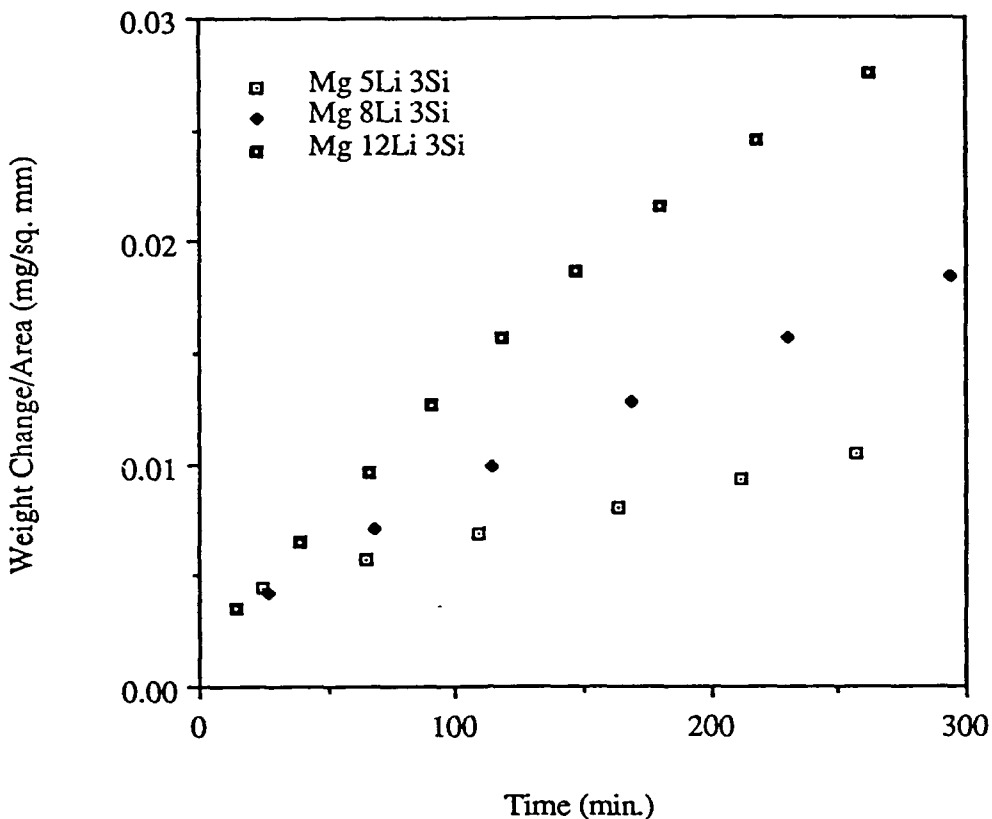


Figure 32. The weight gain versus time data, obtained for the oxidation of some ternary Mg-Li-Si alloys at 300°C.

Figures 33 and 34 compare the oxidation behavior of Mg-5Li and Mg-8Li alloys with or without Si, respectively. Note that for these compositions of Li, the microstructure consists of two phases (the β -Li in the former alloy being not expected and at the grain boundaries). From these figures it is clear that the addition of Si to these particular alloys has a beneficial effect in terms of oxidation resistance. Therefore, for a two phase alloy the presence of Mg_2Si is beneficial in reducing the oxidation rate by preventing the spalling of the oxide layer. In contrast, Figure 35 illustrates that the single phase structure of β -Li is superior than the two phase α -Mg + β -Li with respect to oxidation resistance. In case of Mg-12Li alloy, the presence of Mg_2Si particles is responsible for the increase in oxidation rate. This may be due to crack formation inside the oxide layer, due to uneven expansion of Mg_2Si and β -Li phases. Although Mg_2Si particles aid in preventing oxide spallation in two phase alloys, they do not have any beneficial effect on single phase Mg-12Li alloy, where spalling is not a problem. Therefore, one can infer that the keying effect of Mg_2Si particles is beneficial when spalling of the oxide layer is a major problem.

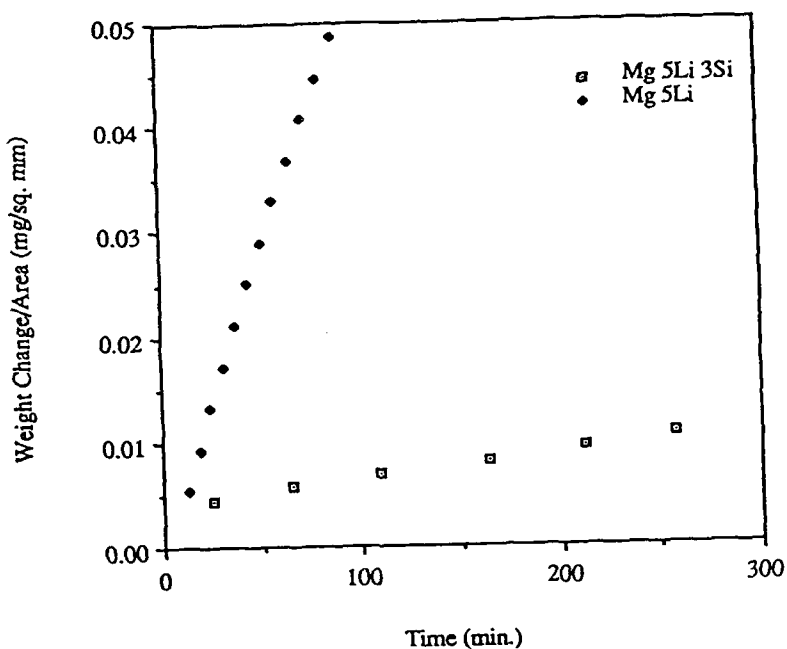


Figure 33. A comparison between the weight gain versus time data, obtained for the oxidation of Mg-5Li and Mg-5Li-3Si alloys at 300°C.

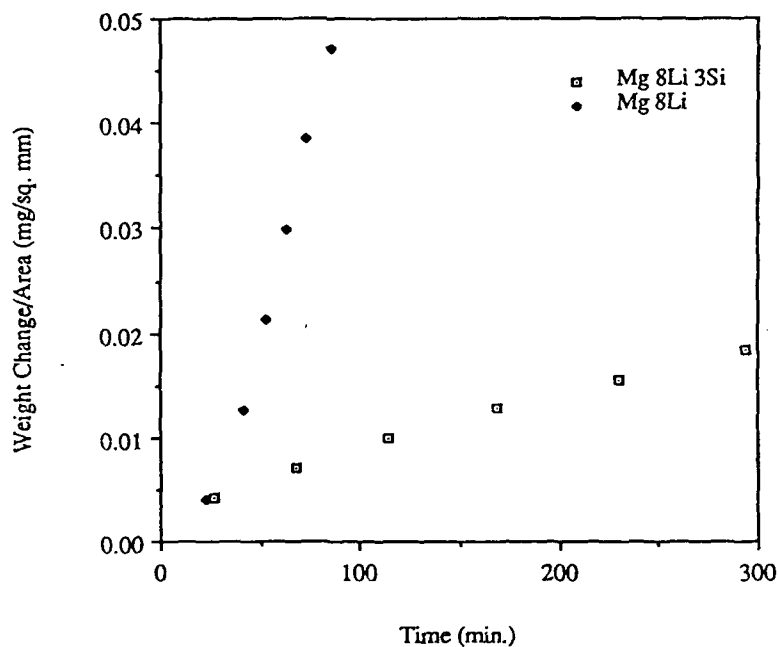


Figure 34. A comparison between the weight gain versus time data, obtained for the oxidation of Mg-8Li and Mg-8Li-3Si alloys at 300°C.

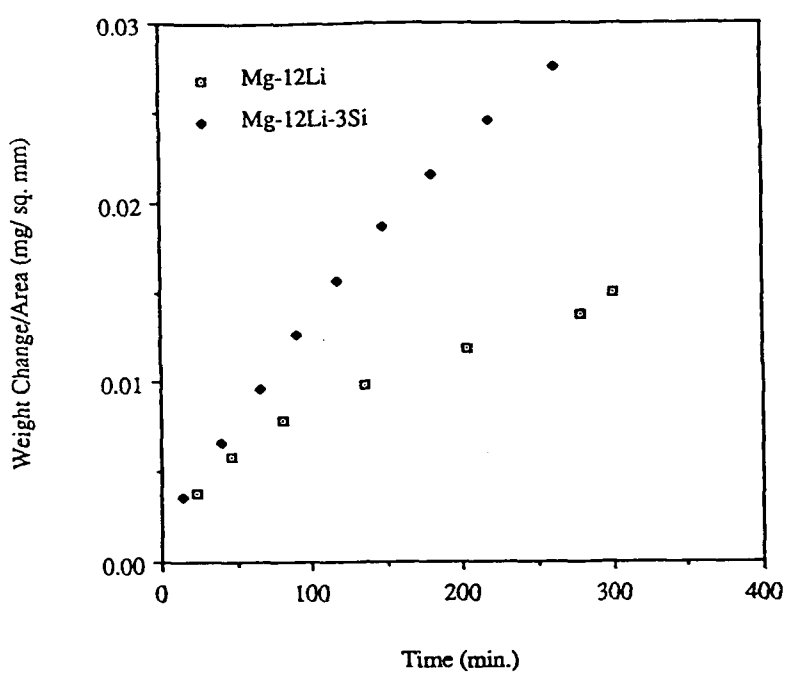


Figure 35. A comparison between the weight gain versus time data, obtained for the oxidation of Mg-12Li and Mg-12Li-3Si alloys at 300°C.

The service temperature of these alloys would be much lower than the test temperature used in the present study. Figure 36 presents a comparison between the oxidation behavior of Mg-12Li-3Si alloy at two different temperatures. It is very clear that a decrease in oxidation temperature by 50°C drastically reduces the oxidation rate.

The activation energy values for oxidation of Mg-5Li-3Si and Mg-12Li-3Si alloys have also been determined by carrying out the oxidation tests at two different temperatures only, and so these data should be used with caution. The activation energy values for Mg-5Li-3Si and Mg-12Li-3Si alloys are 50 k. cal. and 46 k. cal., respectively. Figure 32 shows that Mg-12Li-3Si alloy oxidizes at a higher rate than Mg-5Li-3Si alloy. This result is in full agreement with these activation energy data. These activation energy data are also very similar to those for some other Mg alloys as published by Leontis and Rhines(34).

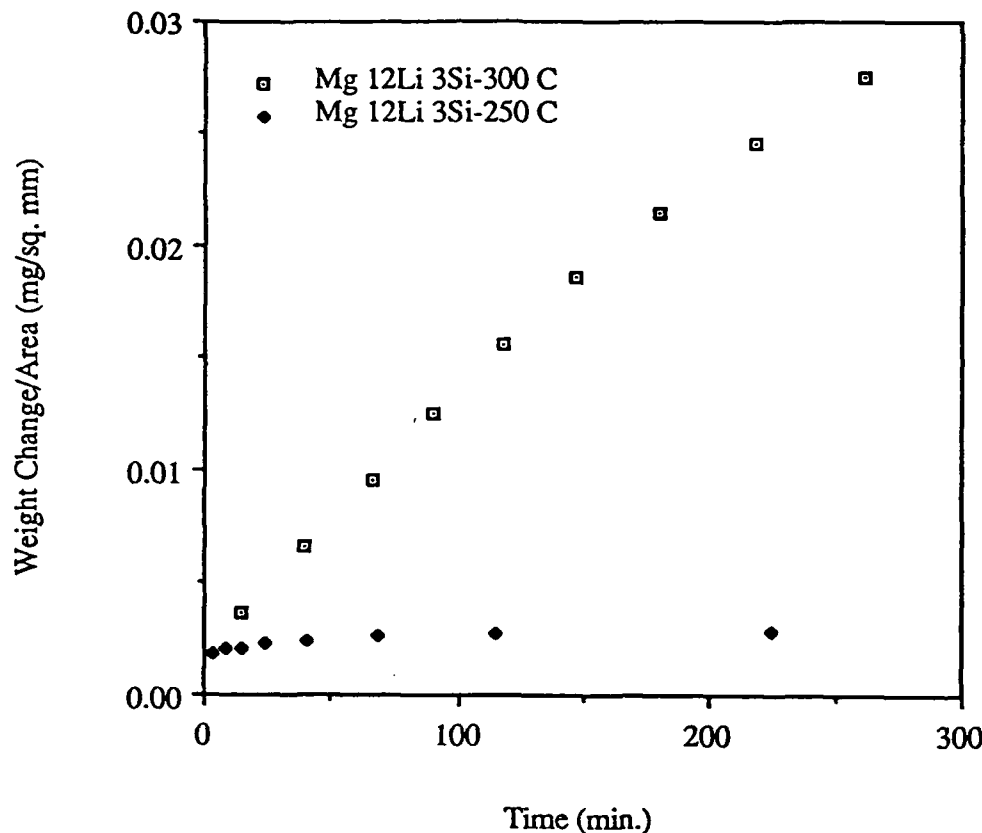


Figure 36. A comparison between the weight gain versus time data, obtained for the oxidation of Mg-12Li-3Si alloy at two different temperatures, 250 and 300°C.

Identification of Oxidation Products Using XRD and XPS Techniques

An attempt has been made to identify the various compounds present in the oxide layers of the samples tested in the TGA. Another purpose of this study is to determine the effect of Si on the formation of various compounds. The various compounds observed in the oxide layers of these alloys are listed in Table 13. In x-ray powder diffraction the signal is obtained from a considerable volume of material, i.e. from a depth of several μm from the surface. Therefore, x-ray powder scan reveals the information about the bulk material, and so in each alloy studied, peaks from Mg and Li have been recorded, as well as from Mg_2Si in the alloys containing Si. As can be seen from the table, the following compounds have been identified; Li_2CO_3 , Li_2O , MgO , LiMgN , and from the Si containing alloys Mg_2SiO_4 . A detailed discussion of these compounds is given below. Firstly, an attempt has been made to detect the type of compounds present at the surface of the material, and secondly, some in-situ studies of the oxidation process have been undertaken; the results of these experiments are described initially.

ALLOY	COMPOUNDS AND ELEMENTS PRESENT IN THE OXIDE LAYER
Mg-12Li	Li ₂ CO ₃ , LiMgN, Li ₂ O, MgO, Mg and Li.
Mg-5Li-3Si	Li ₂ CO ₃ , LiMgN, Li ₂ O, MgO, Mg ₂ Si, Mg ₂ SiO ₄ , Mg and Li.
Mg-8Li-3Si	Li ₂ CO ₃ , LiMgN, Li ₂ O, MgO, Mg ₂ Si, Mg ₂ SiO ₄ , Mg and Li.
Mg-12Li-3Si	Li ₂ CO ₃ , LiMgN, Li ₂ O, MgO, Mg ₂ Si, Mg ₂ SiO ₄ , Mg and Li.

Table 13. A list of compounds present in the oxide layers of various alloys.

X-ray Photoelectron Spectroscopy (XPS) data give chemical information about the top few atomic layers, to a depth of 15 to 60 Å. The XPS spectrum obtained from a Mg-12Li-3Si TGA sample is presented in Figure 37, and interpretation is accomplished by inspection of the partial spectra shown in Figures 38 and 39. Figure 37 shows the oxygen, carbon and lithium peaks. Significantly, no Mg peak is obtained from the surface. The nature of the surface compound containing Li may be determined by reference to Figure 38 which shows the presence of a carbonate peak in the spectrum. Since there is no Mg peak present in the spectrum (Figure 37), this carbonate peak must come from the Li₂CO₃ phase, which is consistent with the x-ray data described above. The presence of the hydrocarbon peak is presumably due to surface contamination. Figure 39 shows the O1s peak. The expected binding energy shift for O1s is that from the carbonate phase. It is interesting to note that there is no evidence to suggest that lithium oxide is present at the surface. The shape of the Li peak is consistent with only one type of Li compound being present at or near the surface. If it has more than one compound of Li there then broadening (>2 eV) of the Li peak, or the presence of two peaks or a shoulder, would be expected to be manifested in the spectrum.

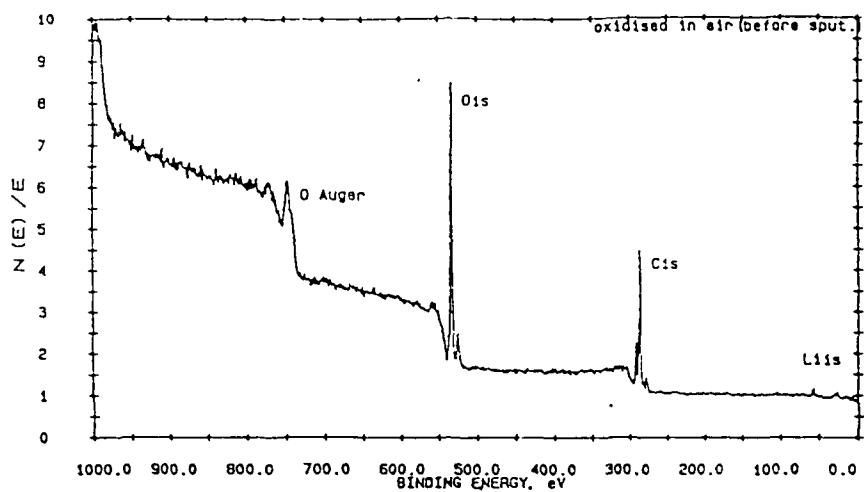


Figure 37. The XPS data from an oxidized (TGA) Mg-12Li-3Si sample showing the oxygen, carbon and lithium peaks.

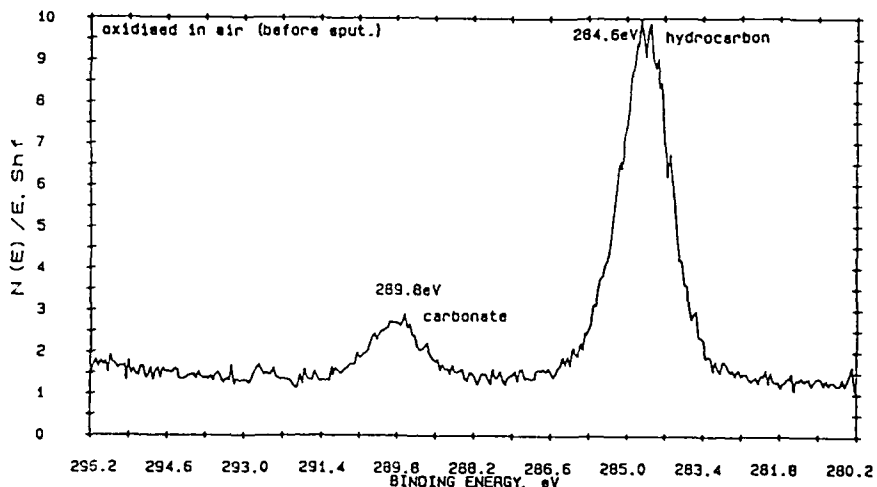


Figure 38. The XPS data from an oxidized (TGA) Mg-12Li-3Si sample showing the presence of carbonate (Li_2CO_3) peak. The hydrocarbon peak arises due to contamination.

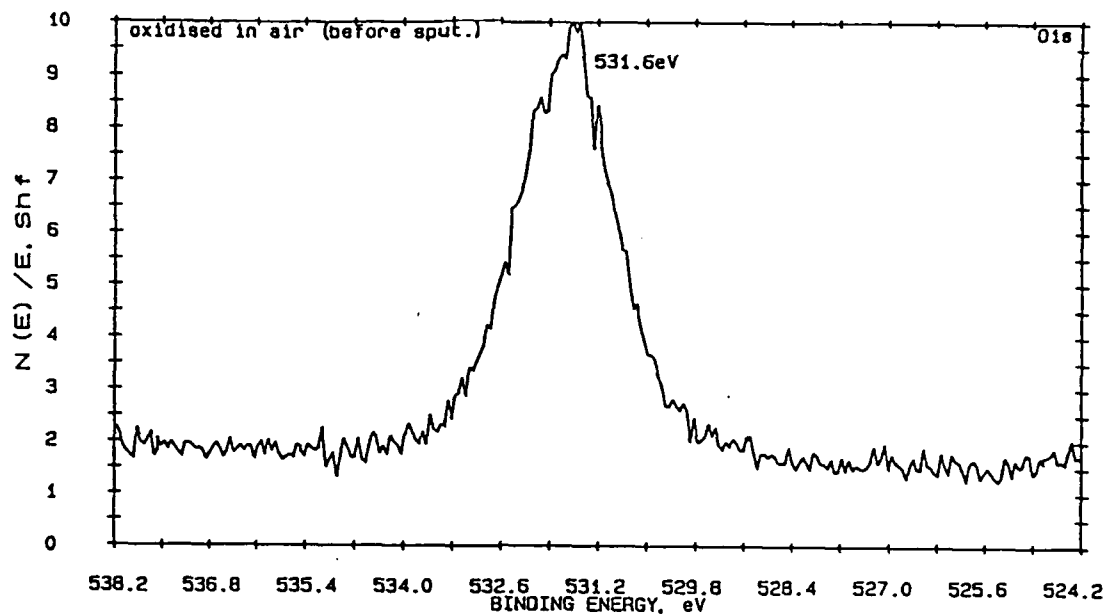


Figure 39. The XPS data from an oxidized (TGA) Mg-12Li-3Si sample showing the O1s peak. The expected binding energy shift for O1s is from the carbonate phase.

In-Situ Oxidation Tests

The purpose of this study is to determine whether various oxides form simultaneously or in different stages. Therefore, successive "powder scans" were recorded while the sample was being oxidized inside the hot stage of the diffractometer. Samples of Mg-5Li-3Si, Mg-12Li and Mg-12Li-3Si were used for this experiment. The Mg-5Li-3Si sample was tested at 250°C, whereas Mg-12Li and Mg-12Li-3Si were tested at 300°C. The results of these experiments were identical, in that the compounds observed in TGA samples were again identified in these experiments (as expected), but that all the compounds were observed from the onset of oxidation. An example of successive x-ray scans are shown in Figure 40. As can be seen, there is essentially no change in the spectra. Incidentally, the Cu peaks come from the sample holder.

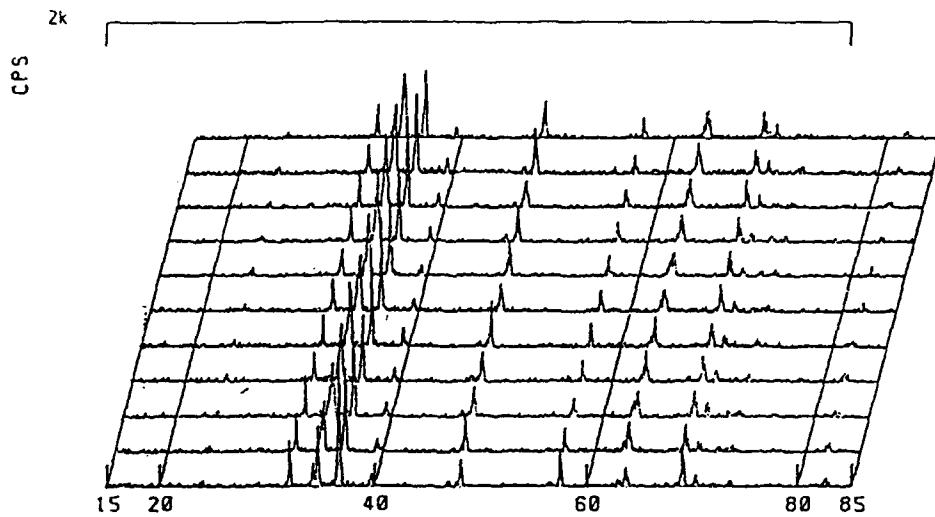


Figure 40. Successive x-ray spectra of oxidized Mg-5Li-3Si alloy obtained by hot stage XRD technique.

Oxidation Model

The TGA data can give useful information about the oxidation rate of various materials. It is interesting to discuss the oxidation mechanism of these alloys. However, oxidation is a very complex process, particularly when considering the case of complex alloys. A simple model is proposed in the following discussion. Compositional profiles through the oxide layers have been determined using Secondary Ion Mass Spectroscopy (SIMS) and Auger Electron Spectroscopy (AES).

In order to determine the concentration profile of various alloying elements, depth profiling has been done for various alloys in SIMS or AES. Figures 41 and 42 show the elemental distribution in the oxide layer of various alloys, as determined by depth profiling in SIMS. From these figures it is clear that the concentrations of Mg, Li and Si remain almost constant, as does that of oxygen, although the profile of this latter element does decrease somewhat in the case of Mg-12Li. In contrast, it appears that the concentrations of carbon and nitrogen are decreasing with increasing distance from the gas-oxide interface.

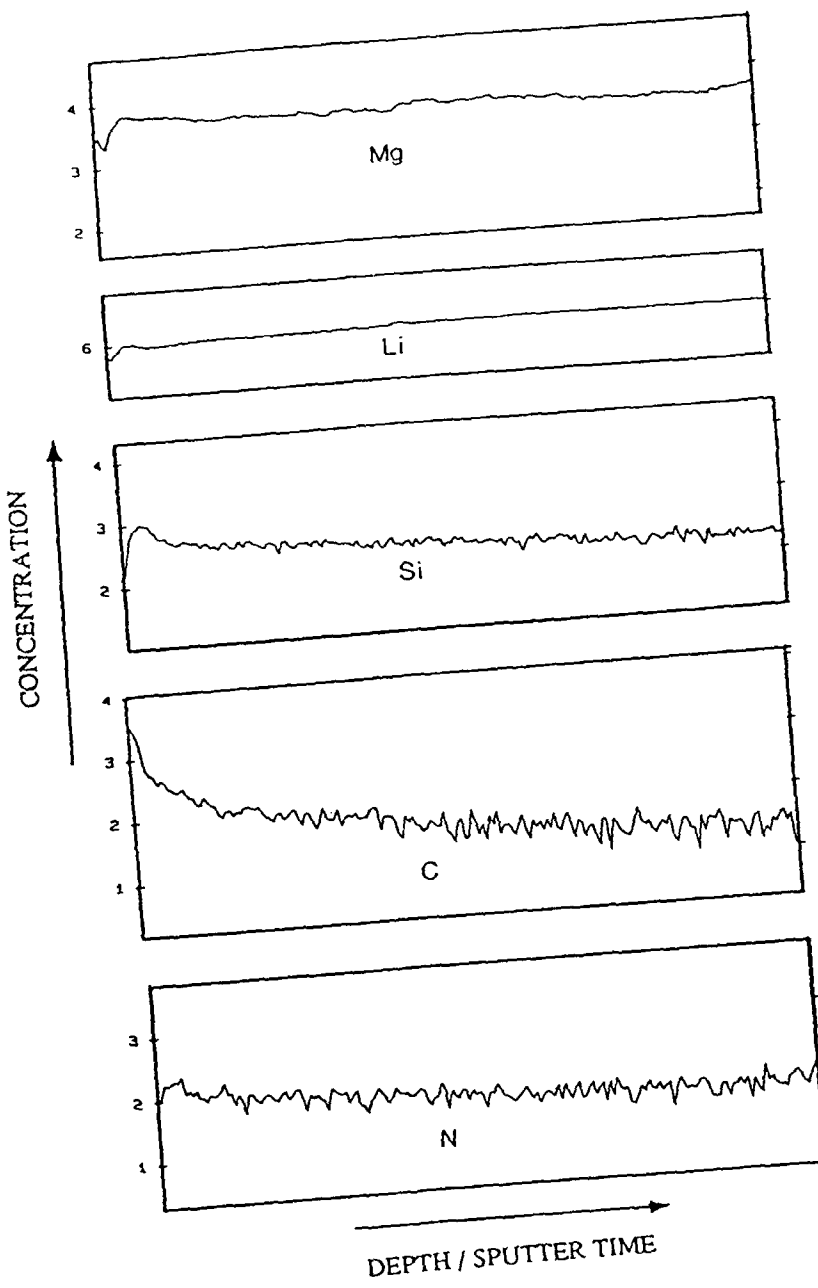


Figure 41. The distribution of various elements in the oxide layer of Mg-8Li-3Si alloy, as determined by depth profiling in SIMS.

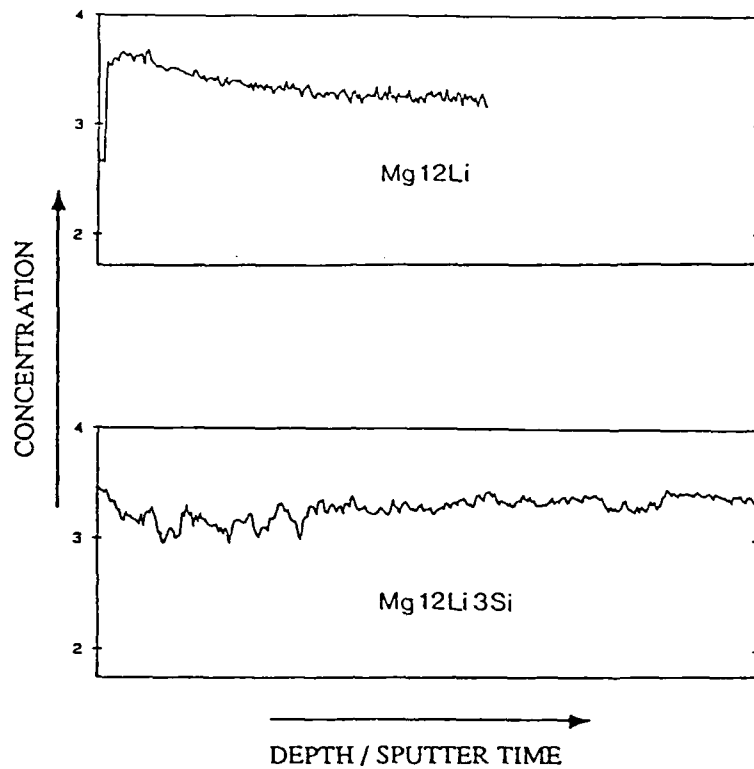


Figure 42. The distribution of oxygen in the oxide layers of various alloys, as determined by depth profiling in SIMS.

In summary of the various results, the following compounds form during oxidation: Li_2CO_3 , Li_2O , MgO , LiMgN , and from the Si containing alloys Mg_2SiO_4 . Also, these compounds all form at the onset of oxidation. The surface layer, i.e. that at the oxide/gas interface, corresponds to Li_2CO_3 . The concentration of alloying elements, namely Mg, Li and Si appears to remain constant through the oxide layer, as, in the main, does oxygen. The concentrations of carbon and nitrogen decrease through the layer. These various results suggest the following model. Thus, the growth of an oxide layer on pure Mg occurs by the diffusion of Mg through the oxide to the oxide/gas interface. In the case of the alloys studied in the present work, the various data are consistent with the opposite behavior, i.e. that oxygen diffuses through the oxide to the oxide/metal interface where oxidation occurs. Thus, the surface is covered with the Li_2CO_3 compound; it may be kinetically more favorable for the oxygen, rather than the various metallic species to diffuse through this compound. This surface compound most probably forms during room temperature oxidation, being a result of the rapid diffusion of Li to the surface and its combination with surface impurities. Oxidation would then proceed by oxygen diffusing through this layer, and forming MgO and Li_2O , two rather stable oxides (with free energies of formation of

-258 and -250 kcal.mole-1, respectively), and Mg₂SiO₄, this latter oxide presumably forming at the Mg₂Si particles. In addition, a nitride is formed, this being due to the diffusion of nitrogen, from the air at the gas/oxide interface, through the oxide to the metal surface. The compositional profiles are consistent with this model since no diffusion gradients of the alloying are established in the oxide layer. Moreover, the concentration of carbon and nitrogen decrease with distance from the oxide/gas interface through the oxide layer, suggesting that the oxide is growing away from the source of these elements.

Oxidation Behavior of Mg Alloy "Standards"

The purpose of this study is to determine the effect of various alloying elements, other than Li and Si, on the oxidation behavior of Mg. Al, Zn and Y have been chosen for this purpose. The reason behind this choice is that they are most frequently found in many commercially available alloys of Mg. The oxidation behaviors of these alloys are determined by using a thermo gravimetric analyzer. The compositions of these alloys, reported in terms of atomic percent, are as follows:

1. Mg-8Al
2. Mg-1Zn
3. Mg-8Al-1Zn
4. Mg-8Al-0.5Zn-0.5Y

The weight change per unit area of these alloys is plotted as a function of time in Figure 27. From Figure 43, it is clear that Mg-1Zn has the highest rate of oxidation. In the case of Mg and Zn, oxidation occurs by the metal atoms diffusing through the oxide layer to the gas/oxide interface. It has been established that in the case of the alloys discussed above that the opposite behavior may occur. Therefore, it is reasonable to assume that in Mg-Al alloys, Al reduces the oxidation rate of Mg by forming a protective layer of Al₂O₃, and causes the oxidation mechanisms to change, the oxygen atoms diffusing through the oxide layer for oxidation at the oxide/metal interface. If we add Zn to Mg-8Al, the oxidation rate increases to some extent due to very high mobility of Zn. The addition of Y along with lowering of the amount of Zn, improves the oxidation resistance. The alloys containing Al and/or Y show a very strong and adherent layer of oxide. It would seem prudent to design an oxidation resistance Mg alloy on the basis of additions of Al and Y.

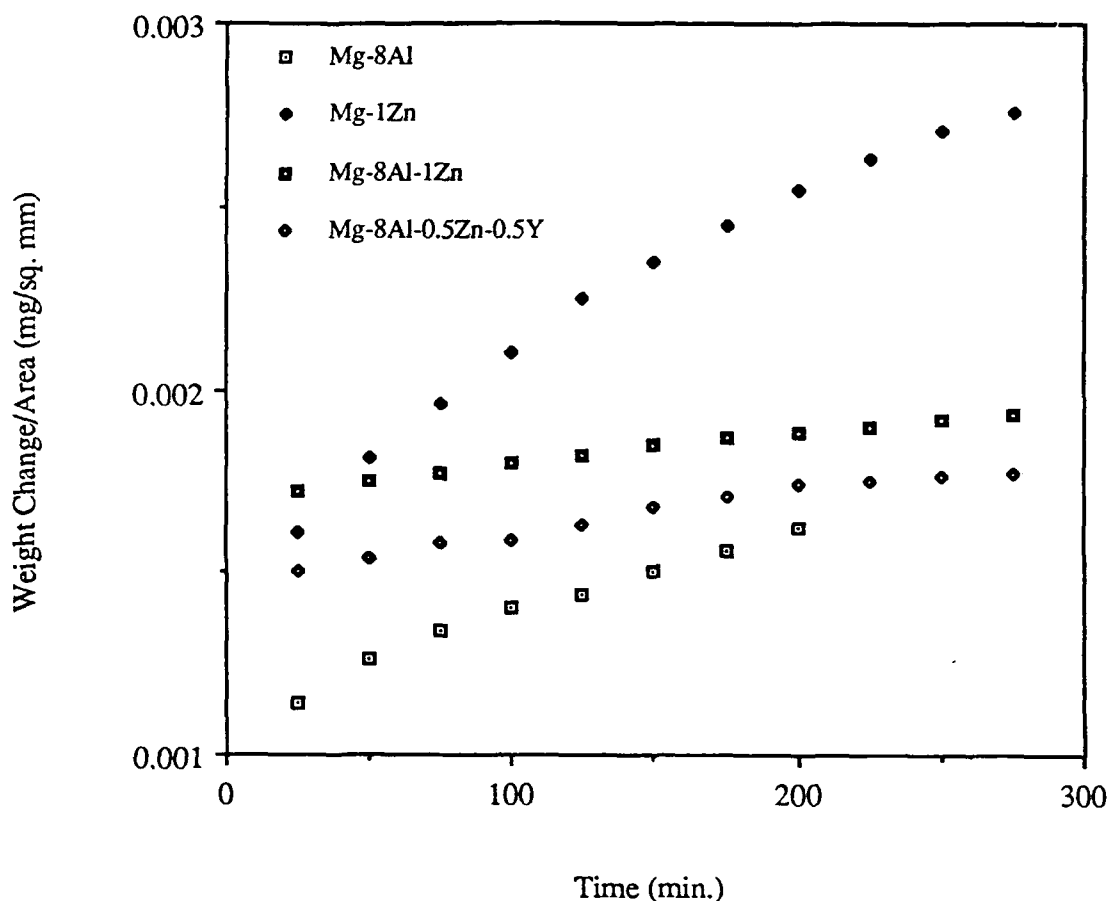


Figure 43. The weight gain versus time data, obtained for the oxidation of some alloys of Mg at 300°C.

Conclusions

1. An attempt has been made to determine the Mg corner of ternary phase diagram of the Mg-Li-Si system. This ternary diagram has been drawn semi-quantitatively, on the basis of the XRD, DSC and optical metallography data. It has been observed that the effect of Si on the transformation temperature of Mg-Li system is negligible. Most of the Si forms the Mg₂Si phase. Li probably goes into the solid solution in Mg₂Si and changes its lattice parameter. The various phases present in the binary and the ternary alloys of Mg-Li and Mg-Li-Si respectively have been identified by XRD technique. The ternary eutectic is present only in those alloys containing 8 wt.% Li together with Si.
2. The effect of Li on the metastable Mg-Si phase diagram has been determined. Li reduces the eutectic temperature and may shift the eutectic to a slightly more dilute eutectic composition. A coupled eutectic structure has been found in the melt spun Mg-xLi-3Si alloys. The coupled eutectic

structure consists of the rods of Mg₂Si embedded in the matrix of cph α -Mg phase. The effect of Li on these materials is only to change the c/a ratio of the cph α -Mg phase. A coupled eutectic structure can only be seen in the thin region of the ribbon where the degree of under cooling is much higher than that in the thick region.

3. The tensile properties of the melt spun Mg-xLi-3Si ribbons have been determined. In the Mg-Si system, melt-spun ribbons of Mg-5Si exhibit a coupled eutectic structure and have a lower fracture strength than ribbons of Mg-3Si. This has been attributed to decohesion along the interface between the matrix and particles of Mg₂Si. In case of ribbons of Mg-xLi-3Si, Li increases the fracture strength, and this has been attributed to the effect of Li on the axial ratio of the cph α -Mg, which is decreased, which inturn is expected to permit the activation of additional slip systems.

4. The tensile properties of laser surface melted Mg-xLi-3Si alloys have also been determined. Among all alloys only four exhibited yield stress, three of which are the binary alloys of Mg-Li. Their yield strength is significantly higher than that of the casting alloy K1A-F. This can be attributed to the finer grain size of the rapidly solidified materials than the casting alloy. When Si is added to the binary Mg-Li alloys the tensile strength increases significantly. This may be due to dispersion of the intermetallic compound Mg₂Si. But the tensile strengths of the Si containing alloys are reduced compared to expectations based on pure Mg, and this has been attributed to decohesion between Mg₂Si and the matrix, and also to brittle failure of larger particles of Mg₂Si.

5. The microstructure has been shown to have a significant effect on the oxidation behavior of Mg-Li and Mg-Li-Si alloys. A single phase material appears to offer a superior resistance to oxidation than does a two phase material. The effect of Li is to increase the oxidation rate of the two phase materials. The ternary alloys of Mg-Li-Si show a parabolic type oxidation behavior. The activation energy for oxidation of various Mg-Li-Si alloys are similar to those of many commercial alloys of Mg. It has been proposed that oxidation takes place at the oxide-metal interface, requiring the diffusion of oxygen through the growing oxide layer. The oxide contains the following compounds: Li₂CO₃, Li₂O, MgO, LiMgN, and from the Si containing alloys Mg₂SiO₄. The first of these covers the surface of the oxide layer, i.e. in contact with the gaseous environment. It has also been found that these compounds form at the beginning of the oxidation test.

Alloys Based on Mg-Gd

The microstructures and mechanical properties of Mg alloys containing 10 and 20 wt.% Gd were described in detail in the previous AFOSR report. These results are summarized as follows.

Aging Behavior

Samples of the alloys were solution treated at 532°C for 12 hours followed by an oil quench and then aged at different temperatures and times to develop aging curves. The results of the study are plotted in Figure 44. The hardness of alloy specimens aged at 200°C increased slowly and leveled off after a hardness increase of \approx 10%. Specimens aged for two hours at 300°C exhibited the maximum increase in the microhardness after aging.

TEM examination of the heat treated specimens was conducted to determine the identity and precipitation sequence in the Mg-Gd alloys. In the case of Mg-20 wt.% Gd alloy specimens aged at 200°C hardening was determined to be caused by the formation of ordered precipitates having the hexagonal DO₁₉ structure. The precipitation behavior was different at higher temperatures. At 300 and 350°C, initial aging resulted in formation of ellipsoidal precipitates \approx 500Å in diameter and \approx 4000Å along their major axes. Diffraction patterns taken from these precipitates could be indexed on the basis of an orthorhombic cell with lattice parameters $a = 22.24\text{\AA}$, $b = 6.42\text{\AA}$, and $c = 5.21\text{\AA}$.

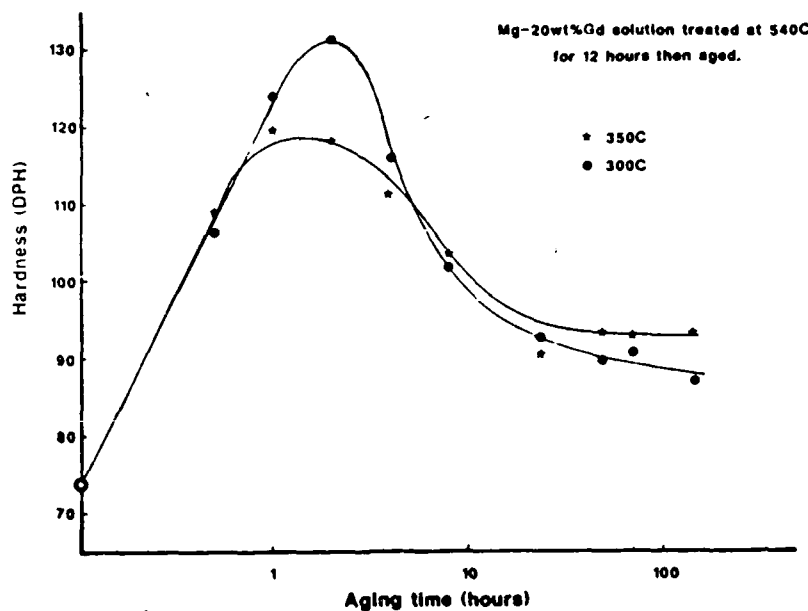


Figure 44. Knoop microhardness (50 gram load) of Mg-20wt.% Gd aged for various times and at different temperatures.

The value of the c parameter of the orthorhombic phase was found to be identical to that of Mg, and the value of the a parameter was the same as the lattice parameter of the equilibrium Mg₂₄Gd₅ phase. The orientation relationship between the matrix and precipitate was established to be [0001]Mg // [001]orth ppt and (10T0)Mg // (100)orth ppt. There are three variants possible with this relationship, and three variants of the orientation relationship between the precipitate and the matrix were observed. Aging for longer times resulted in transformation of the orthorhombic phase into platelets of the equilibrium, fcc Mg₂₄Gd₅ precipitate. The orientation relationship between Mg and this phase was determined to be [0001]Mg/[011]Mg₂₄Gd₅ and (2110)Mg//(1T1)Mg₂₄Gd₅. Further aging of the specimens resulted in coarsening of the Mg₂₄Gd₅ precipitates.

Mechanical Behavior

Mechanical test specimens of Mg-10 and 20 wt.% Gd after various heat treatments were tested at room temperature and 200°C. The results of the tests are tabulated in Table 14. The ductility of the samples was quite dependent on the concentration of Gd in the alloys. There was no set of conditions where an alloy containing 20 wt.% Gd was more ductile than a more dilute alloy. In fact, the best combination of properties for the Mg-20 wt.% Gd alloys was observed in the as-cast condition. The grain size in these alloys was small, therefore many grains were favorably oriented for slip. The ductility of these a-Mg grains was large since very few precipitates were present within the matrix. The heat treated alloys had acceptable strengths at temperature, yet their ductilities were only 1 or 2%. The grain size in these alloys was very large due to grain growth during solution-treatment. It was concluded that the combination of large grain size and an unfavorable precipitate morphology were responsible for the poor ductilities observed in this material after heat treatment. The Mg-10 wt.% Gd alloys had a much better combination of tensile properties. Although the decrease in the Gd content of the alloy lowered the yield strength of the as-cast material, the ultimate strength and ductility were higher. This was attributed to smaller amounts of the grain boundary Mg₂₄Gd₅ in this alloy. Solution-treating and aging this alloy did not noticeably improve either of the tensile properties, although the ductility of the aged specimens was much improved in all test conditions for all specimens. The thermal stability of the tensile properties of the 10 wt.% Gd alloys were excellent. The alloys retained on average 91% of their room temperature yield and ultimate strength at 200°C. The ductility of the alloys was doubled by the increase in test temperature. This associated with the activation of pyramidal slip systems which operate at elevated temperatures, and an increase in thermally activated cross slip of basal dislocations onto adjacent slip planes.

Alloy	Condition	Test Temp (°C)	0.2%Y.S. MPa (Ksi)	U.T.S. MPa (Ksi)	ϵ_f
Mg-20wt%Gd	as-cast	25	136.2	154.4	3.36
	535/8/OQ	25	72.3	157.0	7.47
	535/8/OQ	25	fol	214.3	0.05
	300/2/FC	200	81.2	212.3	1.74
	535/8/OQ	25	fol	139.6	0.052
	350/2/FC	200	82.5	195.0	0.94
Mg-10wt%Gd	as-cast	25	88.3	176.6	7.6
	535/8/OQ	25	*	*	*
	535/8/OQ	25	97.2	187.4	11.6
	300/2/FC	200	68.8	167.1	22.05
	535/8/OQ	25	83.0	174.7	9.35
	350/2/FC	200	85.4	165.9	19.64
	525/8/OQ	25	92.3	168.1	10.3
	300/2/FC	200	86.3	159.0	25.5

* Inclusion present at fracture surface.

fol - failed on loading

Condition legend - solutioning temp (°C)/aging time (hours)/cooling medium

Table 14. Tensile data for Mg-Gd alloys following various heat-treatments.

The effect of grain size on improving the ductility was studied by solution treating specimens of the 10 wt.% Gd alloy at 525°C rather than 535°C. The specimens were aged at the same temperature to produce identical precipitate distributions within the matrix. As can be observed in Table 14, the tensile properties were largely unaffected, while the ductility of the alloy was improved by about 12%. This result would be expected since the ductility of Mg is highly dependent on the grain size.(35)

Intermetallic Compounds Based on Al₃X

There is currently a great interest in intermetallic compounds (IMC) which combine excellent mechanical properties such as strength, stiffness and oxidation resistance, with desirable physical properties such as low density and high melting point. This interest is driven primarily by the aerospace and aeronautics industries for which weight considerations are of utmost importance. For intermediate temperature applications, ordered alloys based on Al₃X, where X is a group IVA or VA transition metal, have the desired properties and therefore a number of studies have been undertaken in this area⁽³⁶⁻⁴³⁾. The attractive properties found in IMC's result largely from long-range atomic ordering which may also be responsible for the primary shortcoming of many intermetallics, that being the low ductility observed at ambient temperatures. A knowledge of the common behavior of Al₃X compounds and similar IMC's can be used to gain a better understanding of the mechanical behavior of the aluminides. For example, a great deal of work has been conducted on materials with the L₁2 type crystal structure(eg.44-49) from which valuable insight can be gained toward understanding the deformation behavior of the Al₃X intermetallics.

It is anticipated that some amount of alloying will be needed to effect mechanical property changes. Thus, the most feasible way to modify intrinsic properties of intermetallics, since alloying elements will affect the electronic configuration (i.e. bonding) and so crystal structures, anti-phase boundary and superlattice stacking fault energies, etc. In order to reduce segregation effects and provide an homogeneous distribution of the alloying elements, it is important to employ a processing technique such as rapid solidification. It is not surprising therefore that previous studies suggest that rapid solidification (RS) processing of these ordered alloys may be the most promising route for production of bulk material^(50,51). RS techniques result in several microstructural modifications which may prove important for IMC's to become technologically useful materials. As referred to above, one effect of increasing the solidification rate is in a reduction of elemental segregation. RS techniques also lead to extended solid solubilities of certain microalloying elements such that subsequent microstructural decomposition can result in the controlled precipitation of a dispersed phase. Finally, RS processing can lead to the formation of metastable crystalline or amorphous phases which may again provide some beneficial properties.

Background

Crystal Structures

Intermetallic compounds of the type Al₃X listed in Table 15 all have the DO₂₂ or DO₂₃ crystal structure, both of which are closely related to the L1₂ structure. The DO₂₂ and DO₂₃ structures, shown schematically in Figure 45b) and c), are closely related to the L1₂ type crystal structure in Figure 45 a), often referred to as the Cu₃Au structure. For an A₃B compound with the L1₂ structure, corner atomic sites of the basic face centered cubic lattice are occupied by B atoms and face centered sites by A atoms. The DO₂₂ structure can be derived from the L1₂ structure by introducing an $a/2 [110]$ shear displacement on every {001} plane. It is noted that in the tetragonal structures, the asymmetric convention for designating planes and directions is employed, such that $\langle hkl \rangle$ and $\{uvw\}$ imply that only h and k , and u and v may be permuted, and \pm is implicit. The DO₂₃ structure, on the other hand, results from the introduction of the same shear displacement on every second {001} plane. The resulting tetragonal unit cells have a c/a ratios near 2 for the DO₂₂ cell and 4 for the DO₂₃ cell as listed in Table 15. The crystallographic indices will be given with respect to the fcc based partial unit cell for convenience.

<u>Compound</u>	<u>Crystal Structure</u>	Lattice Parameter (Å)		
		<u>a</u>	<u>c</u>	<u>c/a</u>
Al ₃ Ti*	DO ₂₂	3.848	8.596	2.234
Al ₃ Zr	DO ₂₃	4.014	17.320	4.315
Al ₃ Hf	DO ₂₃ (LT)	3.919	17.653	4.504
	DO ₂₂ (HT)	3.893	8.925	2.293
Al ₃ V*	DO ₂₂	3.780	8.321	2.201
Al ₃ Nb	DO ₂₂	3.844	8.605	2.239
Al ₃ Ta	DO ₂₂	3.839	8.535	2.223

Table 15. Al₃X compounds formed between aluminum and the group IVA and VA transition metals with their related DO₂₂ and DO₂₃ crystal structures and lattice parameters.

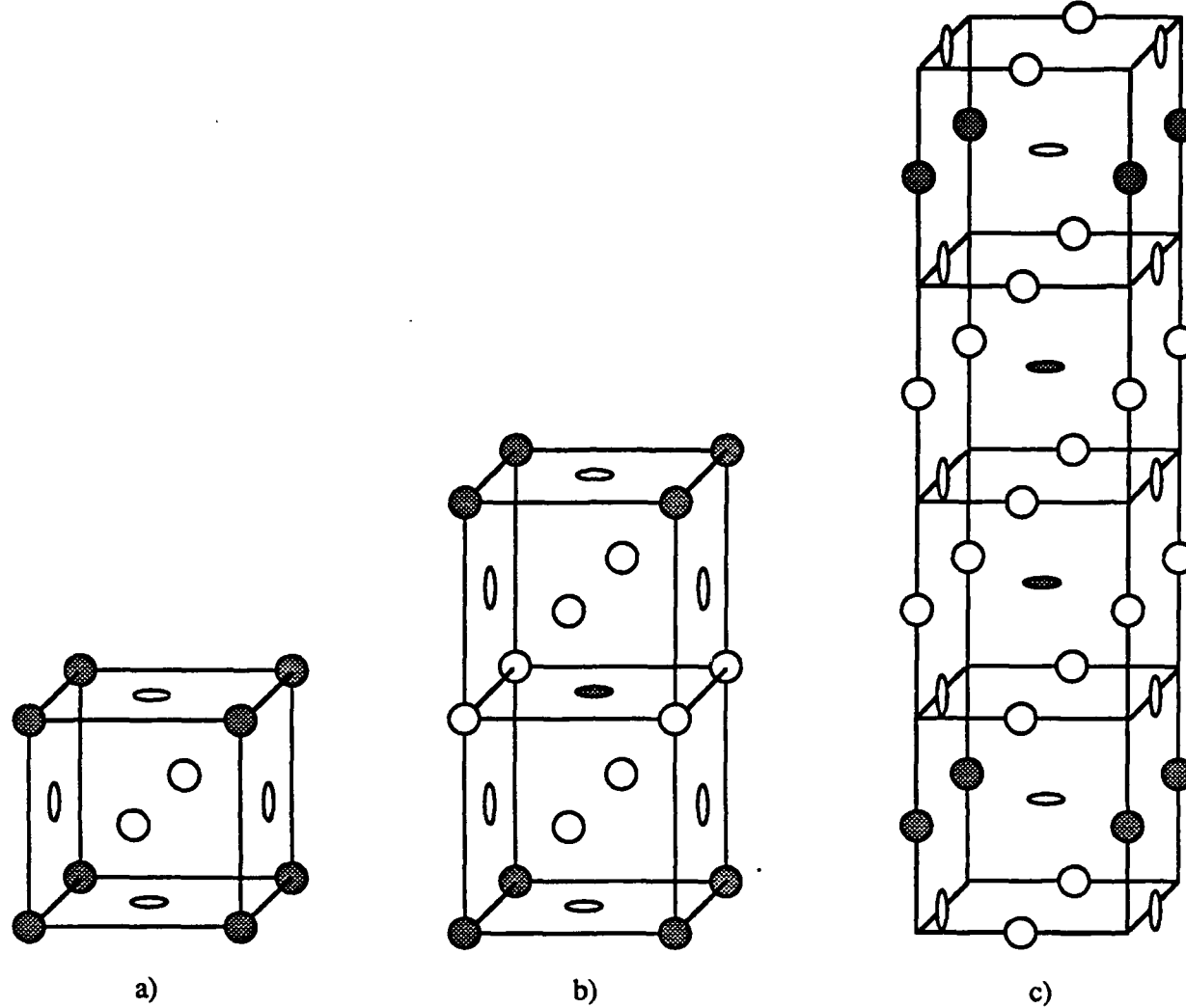


Figure 5. Unit cells of the L1₂, a), DO₂₂, b), and DO₂₃, c), crystal structures which are observed in the Al₃X-based alloy systems.

Deformation Behavior of Al₃Ti

Mechanical Properties of Al₃Ti

In order to understand the fundamental sources of brittle behavior in the IMC's, it is first necessary to identify the operative deformation modes and their underlying dislocation structures. The observed brittleness in intermetallics may be attributed to a number of factors. In any ordered material, dislocation motion is intrinsically difficult resulting from the possible alteration of the

chemical nature of bonds between atoms along a dislocation line segment, depending on the specific shear (i.e. Burgers vector) associated with the dislocation. Even when certain slip systems are energetically favorable, there may be an insufficient number of independent systems to allow for macroscopic deformation in a polycrystalline sample, that is, the von Mises criterion is not satisfied⁽⁵²⁾. The morphology of slip is also important in terms of planarity, i.e. a shortage of dislocation sources, so that significant stress concentrations on grain boundaries may result from the formation of dislocation pile-ups⁽⁵³⁾. Impurity elements such as oxygen, nitrogen and hydrogen have been associated with brittle behavior of other ordered alloys⁽⁵⁴⁾. Recently, the nature of the atomic bonding in certain IMC's has been shown to play an important role in the deformation process^(55,56). Strong covalent bonding in Ti₃Al and TiAl control the nature and mobility of defects in these ordered structures.

The intermetallic compounds of the Al₃X type (X= Ti, V or Nb) represent a new class of materials of interest for application in structural components for use at elevated temperatures. These compounds have an ordered DO₂₂ structure. Compared to Ti₃Al and TiAl, Al₃Ti is lighter and possesses superior oxidation resistance⁽⁵⁷⁾. Quite recently, Yamaguchi and co-workers⁽³⁶⁻³⁹⁾ have studied the deformation behavior of Al₃Ti and Al₃V. The brittleness at ambient temperatures is related to the observation that deformation takes place not by {111}<110> slip but by twinning of the type {111}<112̄>. At higher temperatures (\approx 600°C) {111}<112̄> twinning is augmented by slip of the types [100], [010] and [110] presumed to occur on the (001) plane, so that ductility increases⁽³⁷⁾; the $b=<110>$ dislocations are assumed to be dissociated into two $1/2<110>$ partial dislocations separated by a ribbon of APB. One of the aims of the present study is to examine in more detail the fine structure of dislocations in deformed Al₃Ti utilizing weak beam imaging techniques.

A feature of related interest is that partial substitution of Al with about 8-10 at.% Ni⁽⁵⁸⁾ or Fe⁽⁵⁹⁾ modifies the DO₂₂ structure to an L₁₂ structure, expected to slip on the {111}<110> systems. There have been two studies reporting on the mechanical behavior of these L₁₂ alloys. In the first the mechanical behavior in compression of an Al_{66.1}Ni₉Ti₂₄ alloy in the temperature range of 25° to 800°C was studied⁽⁶⁰⁾, and a weak positive temperature dependence of the yield stress, was noted. In the second, the room temperature deformation behavior in compression of an Al₆₇Ni₈Ti₂₅ alloy was studied, and it was observed that slip occurred on the {111}<110> systems, but was accompanied by brittle fracture by transgranular cleavage with little plastic strain⁽⁶¹⁾. A second aim of the present study is to examine in more detail the fine structure of

dislocations at room and elevated temperatures to gain further insight into the mechanisms governing the plastic deformation of these alloys.

Yamaguchi's work⁽³⁶⁾ on the binary compound has shown that the yield stress exhibits a functional dependence with temperature as shown in Figure 46. In the low temperature regime up to approximately 325 °C, the yield strength is seen to decrease slightly with increasing temperature. Within the intermediate temperature range, 325 °C to 620 °C, the yield stress decreases dramatically, while above 650 °C, it again decreases only gradually. From these observations, it is apparent that some type of transition between deformation modes is taking place within the intermediate range.

The stress-strain behavior in Figure 47 over the same range of temperatures supports the conclusion that two distinct deformation mechanisms must exist in Al₃Ti. Macroscopic plastic deformation is negligible near room temperature with fracture sometimes occurring before yielding. Within the intermediate temperature range, the stress-strain curves appear similar in that very little plastic deformation takes place prior to fracture. However, it has been noted that locally the degree of deformation can be very high and these are frequently observed near to sites of crack initiation.

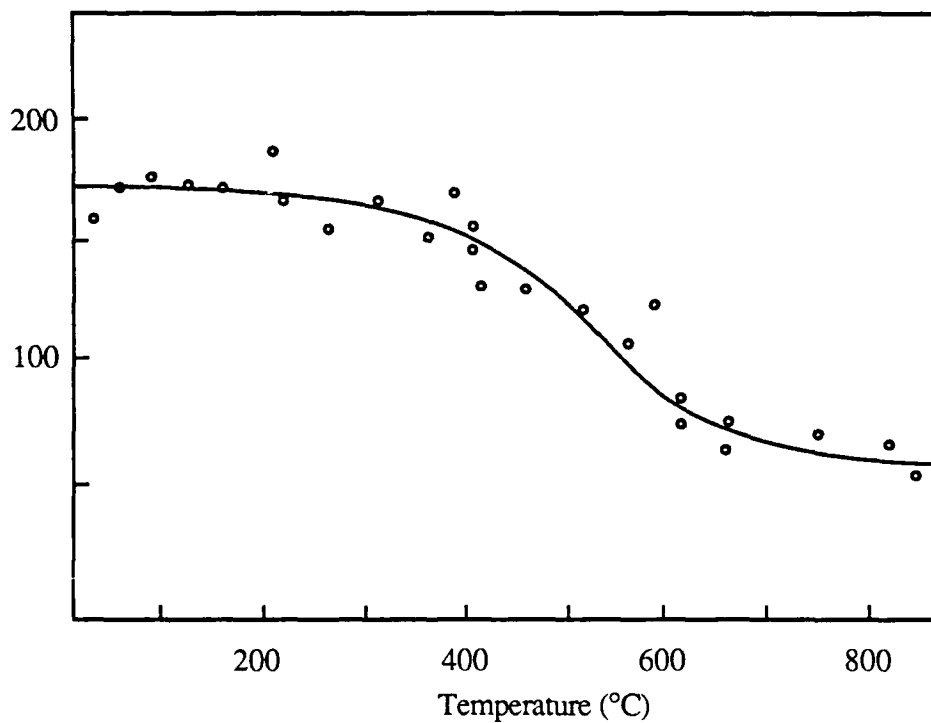


Figure 46. Plot of yield stress versus temperature for polycrystalline Al₃Ti compound.
(from Yamaguchi et. al. (36))

The absence of work hardening in these grains is not explained. Above 620 °C there is a marked increase in ductility, although at much lower stress levels. In general, the mechanisms of plastic deformation are not well understood.

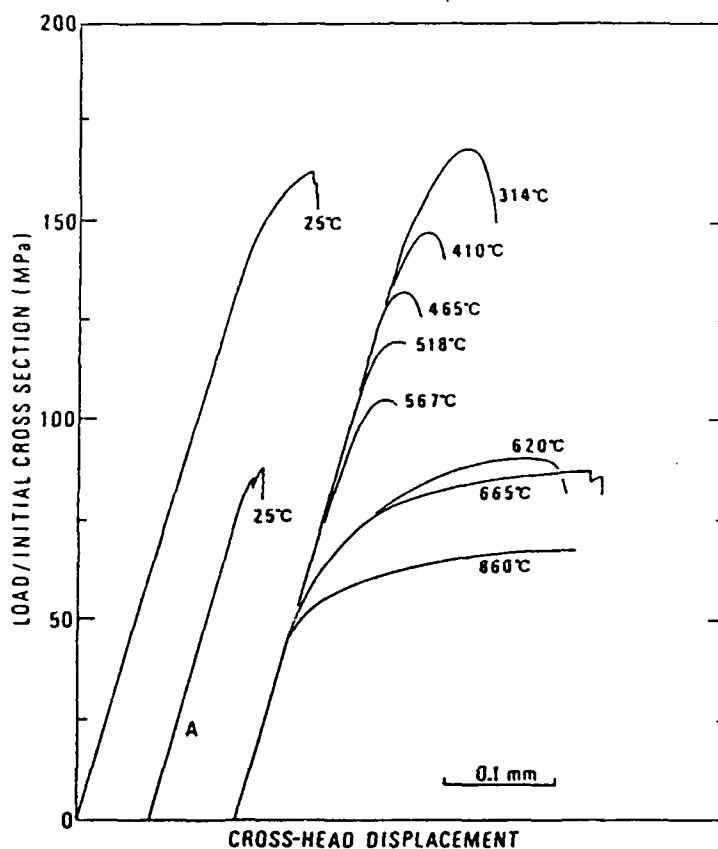


Figure 47. Stress-strain curves of polycrystalline Al_3Ti at various temperatures.

(from Yamaguchi et. al.(36)).

Defect Configurations in Al_3Ti

Over a temperature range of room temperature to $\approx 300^\circ\text{C}$, the deformation structure of Al_3Ti consists primarily of deformation microtwins lying on $\{111\}$ habit planes(36-38). These twins are unique in that the shear vector must not disrupt the local order of the DO₂₂ crystal. Only the $\{111\} < 112 \rangle$ type twinning shown in Figure 48 is allowed since the DO₂₂ symmetry is maintained at the twin boundary for both matrix and twin. This is not true for $\{111\} < 211 \rangle$ twins where the twin plane does not mirror the matrix and twin crystals. Twins with such orientational

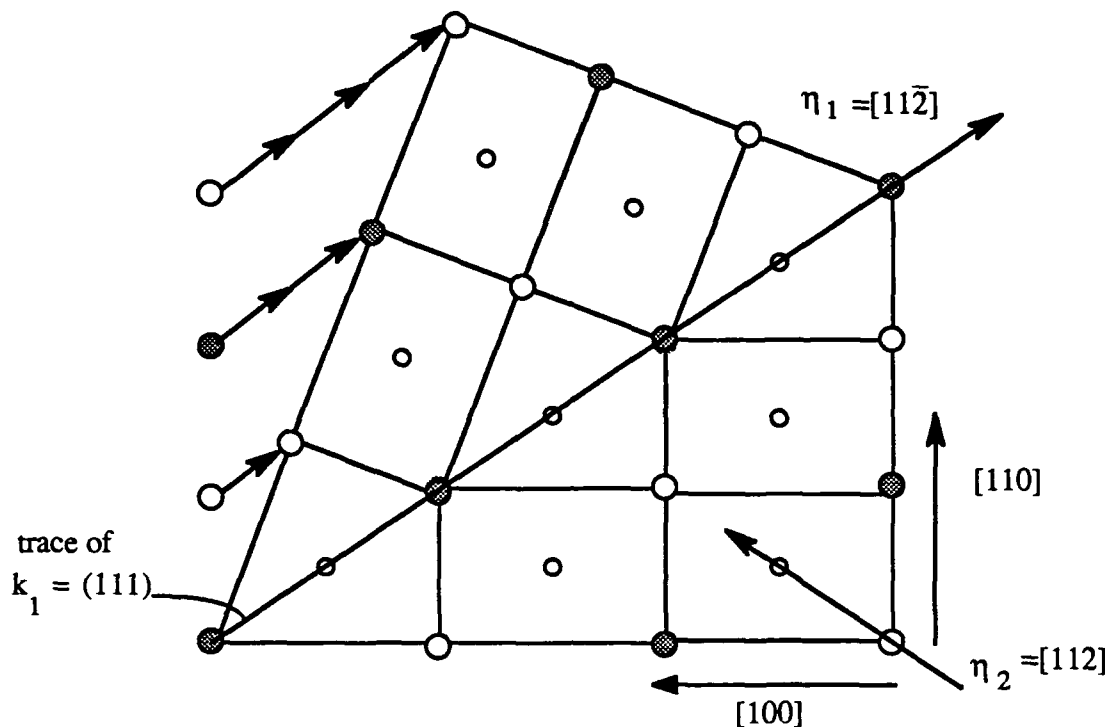


Figure 48. Schematic representation of twinning on (111) plane in an A₃B compound with the DO₂₂ structure. A type atoms are represented by open circles and B type atoms by filled circles with small circles lying in the second atomic layer.

dependency are termed order twins and are observed in Ni₃V (DO₂₂)⁽⁶²⁻⁶⁴⁾.

These twins are formed by the passage of Shockley partials with a Burgers vector, \mathbf{b} , parallel to $1/6<112]$ which bound a stacking fault⁽⁶²⁾. Here again, the Burgers vectors of the partials are restricted to a type which preserves the local order without creating incorrect nearest neighbor bonds. This microtwinning appears to be the only deformation mode containing a shear component normal to the {001} plane. These Shockley-type dislocations, with their associated stacking fault, are energetically favored over other possible dislocation configurations on {111} planes. These include $1/2<110]$ partials separated by an antiphase boundary (APB) and the $1/6<121]$ and $1/6<211]$ dislocations which bound a complex stacking fault⁽⁶²⁾. The various faults are discussed below for the case of the L₁₂ structure.

The current program involves two aspects. The first of these is aimed at characterizing the defects present in intermetallic compounds with related crystal structures, namely DO₂₂ and L₁₂. It should then be possible to gain a better understanding of the similarities between the defects

occurring in the DO₂₂ and L₁₂-based structures. An understanding of these defects and also the deformation mechanisms active in these Al₃X-based compounds with the DO₂₂ and alloyed modifications with the L₁₂ structures determined over a range of temperatures will be used to shed light on the factors influencing the ductility of these compounds.

Experimental Procedure

The Al₃X compounds indicated by an asterisk in Table 15 and certain ternary alloys based on these compounds are being considered in the current program. Powders of these alloys have been produced by a centrifugal atomization process. In this process a charge is first arc melted in a water cooled copper hearth within a chamber which has been evacuated and back filled with argon. The molten alloy is then poured onto a rapidly spinning graphite disk from which small liquid droplets are ejected and quenched in flight in a helium cooling medium. The powder is finally collected in a cyclone separator for screening and analysis. Bulk material was obtained by hot isostatic pressing (HIP) of powder screened to a diameter of less than 120 um. Consolidation was carried out in 1/2 inch diameter titanium cans which were approximately 4 inches long at a temperature of 1000 °C and a pressure of 27 ksi for 4 hours. All materials are to be characterized by Transmission Electron Microscopy (TEM).

The as-atomized powders have been prepared for TEM examination by first embedding the loose powder in electroplated nickel and then thinning in a standard manner. Thin foils of all of the alloy powders and bulk materials were electrochemically polished in a Fischione twin jet polishing unit using a solution of 7.5 vol % sulfuric acid in methanol. After HIP'ping, the consolidated billets were cut into three 0.75 inch sections. In the initial stage of the deformation study, it was deemed acceptable to leave the Ti can surrounding the sections intact in order to contain the brittle material during compression and allow for easier handling. The objective was simply to introduce a small amount of plastic deformation and to characterize the resulting dislocation structures. The removal of the can using a conventional high speed diamond wheel also leads to chipping and possible fracture of the as-HIP'ped blank. For more precise information on the stress-strain behavior in these alloys, compression samples will have to be cut by spark machining and then electropolished to remove surface damage.

The starting microstructures of the as-atomized powders have been characterized and related to the equilibrium phase diagrams. Samples of each composition have been deformed in compression at three elevated temperatures: 300 °C, 600 °C and 800 °C. The strain introduced was in excess of 1.5% in all cases. Investigation of the dislocation microstructures in several alloys has begun. TEM studies have been conducted on either a Philips CM12 or EM430 microscope.

Microstructural Studies

Al-25at%Ti Alloy

The microstructure of the as-atomized Al-25 at % Ti powder shown in Figure 50 consists of massive dendrites identified as the Al_3Ti phase with the DO₂₂ crystal structure and a small fraction of heavily dislocated α -Al along interdendritic regions. Phase identification was accomplished using selected area electron diffraction analysis. Although the equilibrium phase diagram does not generally describe phase stabilities under RS conditions, it can be useful in interpreting solidification structures. The Al-Ti constitutional diagram (see appendix A) indicates that Al_3Ti should form by a peritectic reaction near 1340 °C under equilibrium conditions. Since this type of reaction is known to progress rather slowly, a certain amount of untransformed

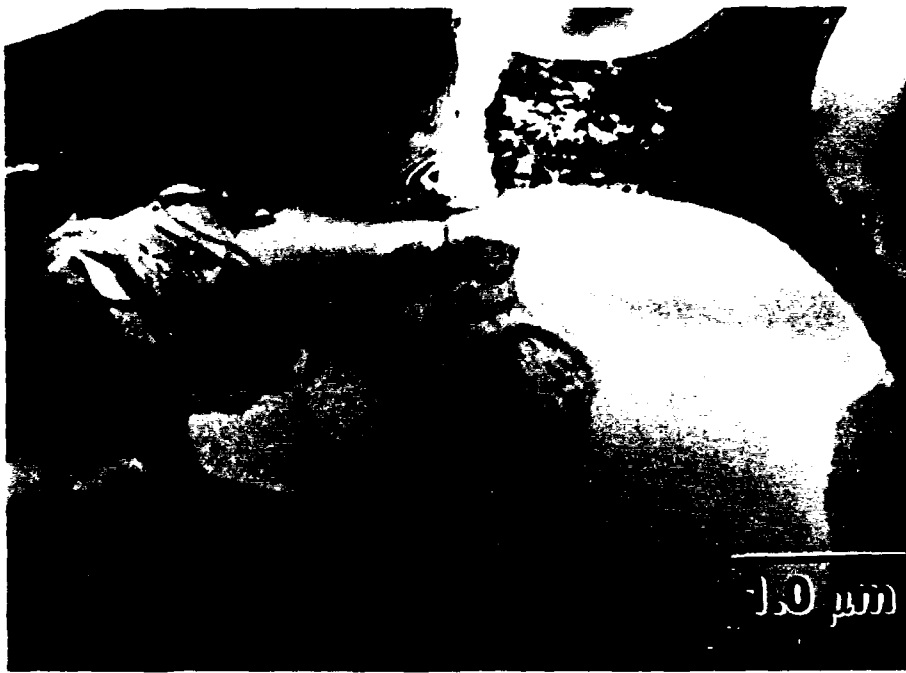


Figure 50. Bright-field transmission electron micrograph taken from an as-atomized Al_3Ti powder particle.

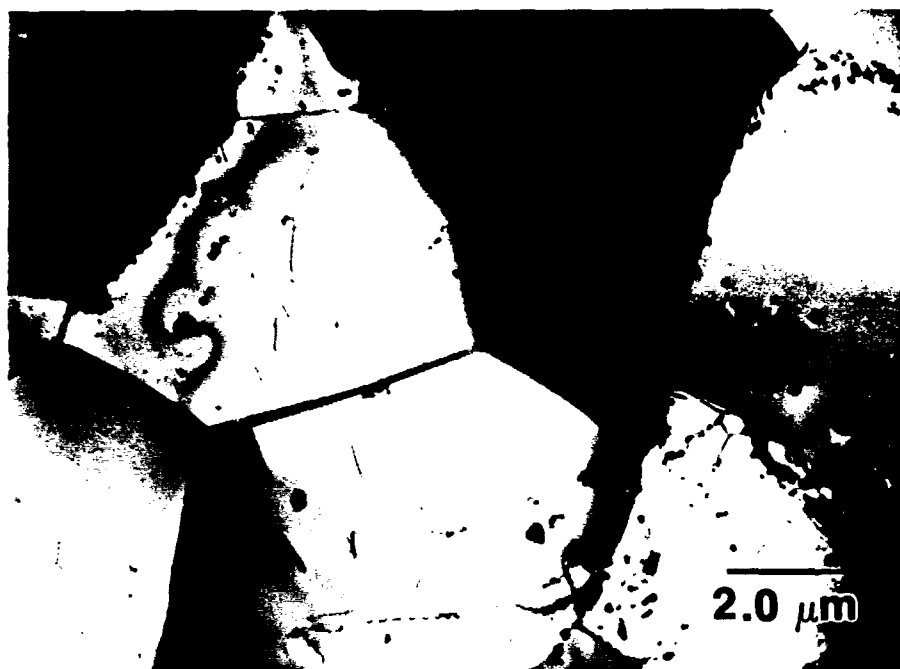


Figure 51. Bright-field electron micrograph taken from HIP'ped Al₃Ti material .

Al₁₁Ti₅ (DO₂₃ structure) phase might be expected on quenching the Al-25 at % Ti alloy. The observed absence of this phase suggests that the undercoolings in the particulate are in excess of 40°C. The as-HIP'ped microstructure of the Al-25 at % Ti in Figure 51, shows no evidence of α -Al but rather contains a small volume fraction of dispersed TiAl (L₁₀ structure) particles. This implies that the alloy may, in fact, be slightly rich in titanium and that the α -aluminum in the RS powder may have arisen from a broadening of the Al₃Ti phase field which lead to solute trapping of titanium and eventually an aluminum-rich liquid. The presence of the γ phase may also be due to diffusion of Ti from the HIP can to the powder.

Al-25at% V Alloy

There are three phases present in the microstructures of the atomized Al-25 (at %)V powder. In Figure 52 (a,b) the phase constituting the primary dendrites was identified as the Al₈V₅ (δ) phase which has an ordered bcc crystal structure with a lattice parameter of 9.234 Å (65). A second phase, identified as the Al₃V compound in Figure 52 (b), appears to have heterogeneously nucleated onto the prior δ dendrites. Finally, a small amount of α -Al was identified at the boundaries between dendrite arms in the same manner as that seen in the as-atomized Al₃Ti powder. The equilibrium phase diagram for the Al-V system can again help



Figure 52 a). Bright-field transmission electron micrograph taken from an as-atomized Al_3V powder particle illustrating the general dendritic solidification structure.



Figure 52 b). Bright-field transmission electron micrograph taken from an as-atomized Al_3V powder particle illustrating the morphology of the individual phases present.

explain the observed solidification structure. Similar to the Al-Ti system, the Al-V constitution diagram (see appendix B) contains a peritectic reaction near 1360°C close to the Al₃V composition. The steep liquidus above the peritectic results in a large temperature differential between the liquidus and peritectic temperature at the stoichiometric composition. Undercoolings in the liquid droplets near the Al₃V composition are not sufficient to bypass the peritectic reaction and hence primary δ dendrites form with the remaining liquid being depleted in vanadium. Finally, this liquid solidifies within the Al₃V + α-Al composition range. The HIP'ped material in Figure 53 is composed of a DO₂₂ matrix with particles identified as Al₈V₅. The presence of these particles appear to be due to incomplete transformation time during HIP'ping (4 hours at 1000 °C) since further heat treatment resulted in the dissipation of these particles. Little or no porosity was observed in either TEM or optical examination and particle bonding appears to be good.



Figure 53. Bright-field transmission electron micrograph taken from a sample of HIP'ped Al₃V material.

Al-8at% Ni-25at% Ti

The crystal structure of the Al₃Ti compound can be modified by macroalloying with nickel. The substitution of approximately 8 atom percent nickel for aluminum results in the stabilization of

the L₁₂ structure ($a_0 = 3.94 \text{ \AA}$). The range of composition for the L₁₂ (μ) phase varies with temperature and some disagreement exists as to the exact composition of this phase. The probable composition range lies between Al₆₇Ni₈Ti₂₅ (58) and Al₆₅Ni₁₀Ti₂₅ (66) at 800 °C (see appendix C). The microstructure of the as-atomized Al-8Ni-25-Ti (at %) powder in Figure 54 consists of primary μ dendrites and small interdendritic particles of Al₃Ni₂ (D5₁₃ structure type, $a = 4.036 \text{ \AA}$, $c = 4.901 \text{ \AA}$) such as those at A. This is not unexpected since the ternary phase diagram indicates the existence of a two phase field between the μ phase and Al₃Ni₂ at 800 °C. Nash further shows that the μ phase is not expected to undergo congruent melting which seems to suggest that a certain degree of undercooling is responsible for the existence of primary L₁₂ dendrites. On thermal exposure during HIP'ping, the microstructure transforms to an L₁₂ matrix with numerous second phase particles of Al₂NiTi (λ phase, L₂₁ structure with $a_0 = 5.87 \text{ \AA}$) as shown in Figure 55.

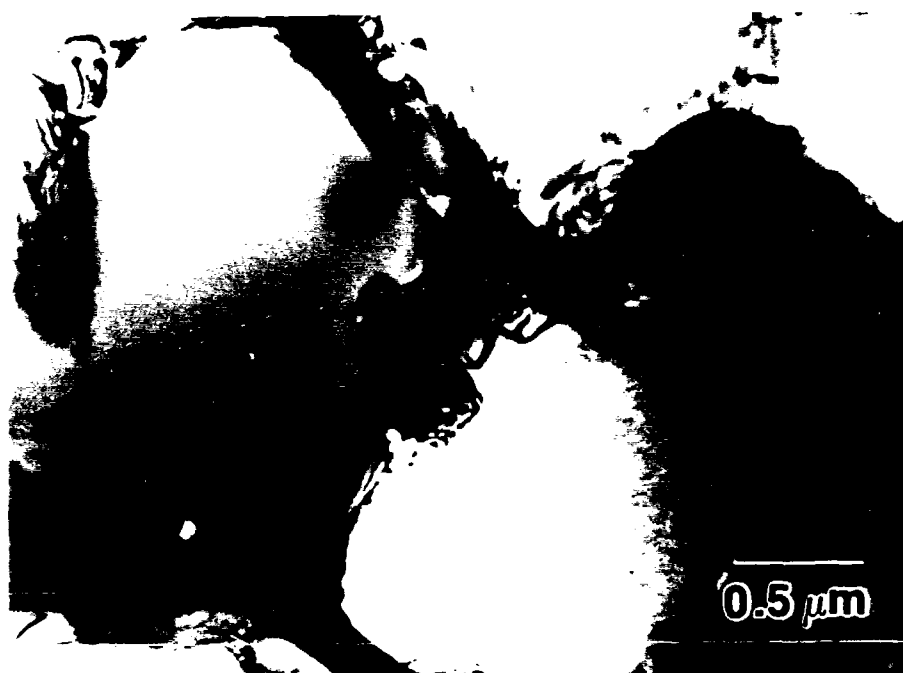


Figure 54. Bright-field electron micrograph of an as-atomized Al-8Ni-25Ti (at%) powder particle.

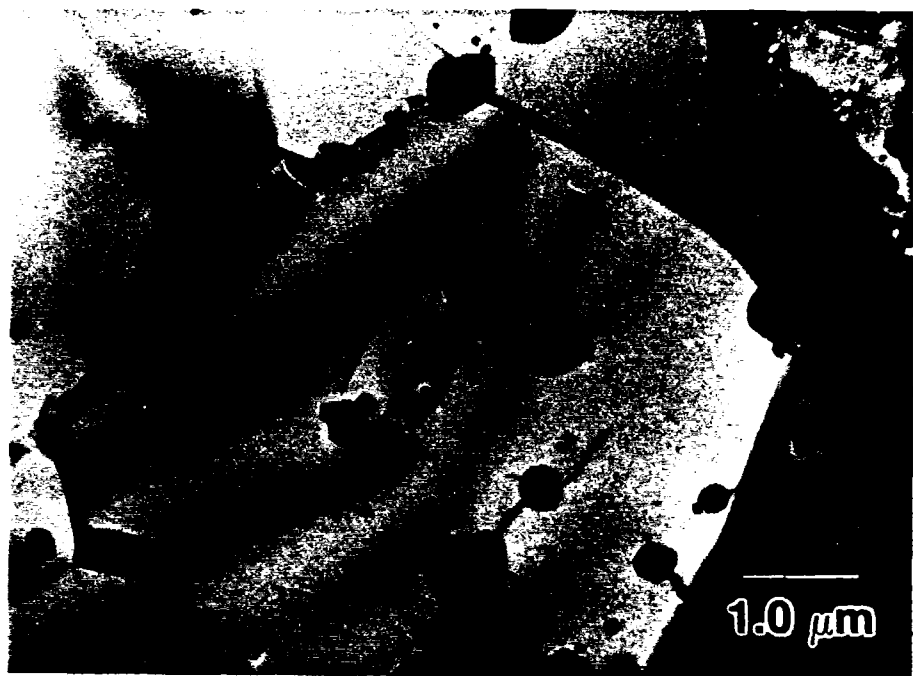


Figure 55. Bright-field transmission electron microscope image taken from HIP'ped Al-8Ni-25Ti (at%) alloy.

Elevated Temperature Deformation Studies

Al₃Ti Deformed at 300°C

Typical areas of a sample deformed in compression at 300°C are shown in the micrographs in Figures 56a–b. Two major features are evident. The first is the presence of stacking faults/order twins on {111} planes. Faults on three such planes, namely, (111), (11T), and (T11) are shown in the micrographs (Figure 56b) and are identical to those reported by Yamuguchi et al.(36-39). These faults are formed by the passage of dislocations with $b=1/6<112\bar{1}$. This can be understood on the basis of the atomic arrangement of Al and Ti atoms on two successive layers on the (1T1) plane shown in Figures 57a–b, where it is seen that only dislocations with $b=1/6[T12]$ will not change

the number of nearest neighbor bonds. The passage of these on successive parallel {111} planes leads to an overlapping stacking fault, which creates a thin layer of twinned crystal.



Figure 56. WBDF micrographs showing stacking faults/order twins on {1T1} planes and secondary slip on the (001) plane in Al_3Ti deformed at 300°C.

The second feature of significance concerns the faults labelled P in Figure 56b. Tilting experiments show that these faults are parallel to (001). The Burgers vectors of dislocations along these faults have been determined by diffraction contrast experiments⁽⁶⁷⁾ and, for example, those labelled A and B in Figure 56b have \mathbf{b} parallel to [T10] and [110], respectively. More specifically, these dislocations have $\mathbf{b}=1/2<110]$ and are connected by an APB ribbon with displacement vector $1/2<110]$. This is confirmed in the dark field images taken with a superlattice reflection (Figure 58) from another area in the sample; the observed fringe contrast is consistent with that expected from APB's. Further inspection of Figure 56a reveals that the faults on (001) generally form at points where {111} twins intersect or at some distance away along one of the {111} twins. The mechanism of formation of these faults, or more specifically, the bounding $1/2<110]$ dislocations is not well understood. A possible mechanism of formation of these dislocations involves cross-slip of the twinning partial dislocations from inclined {111} planes. Thus, the microtwins are formed by glide of partial dislocations with $\mathbf{b}=1/6<112]$; dislocations of the type $\mathbf{b}=1/6<211]$ are not expected to be present. Following the model of Vandershaeve and Escaig⁽⁶⁸⁾, an example of

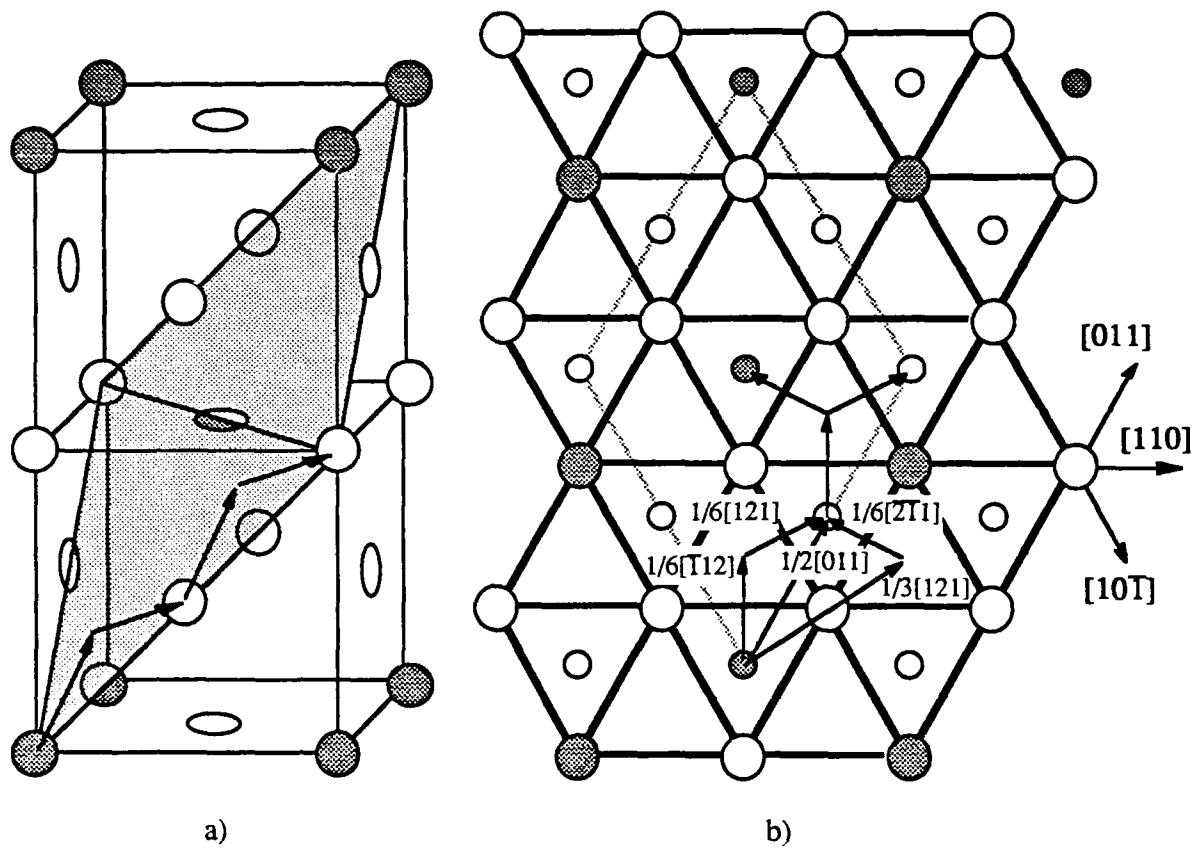


Figure 57. The unit cell (a) and atomic arrangement on the (1T1) plane (b) of the DO₂₂ structure. Open circles denote Al atoms and shaded circles Ti atoms. Atoms on two layers are shown by large and small circles.

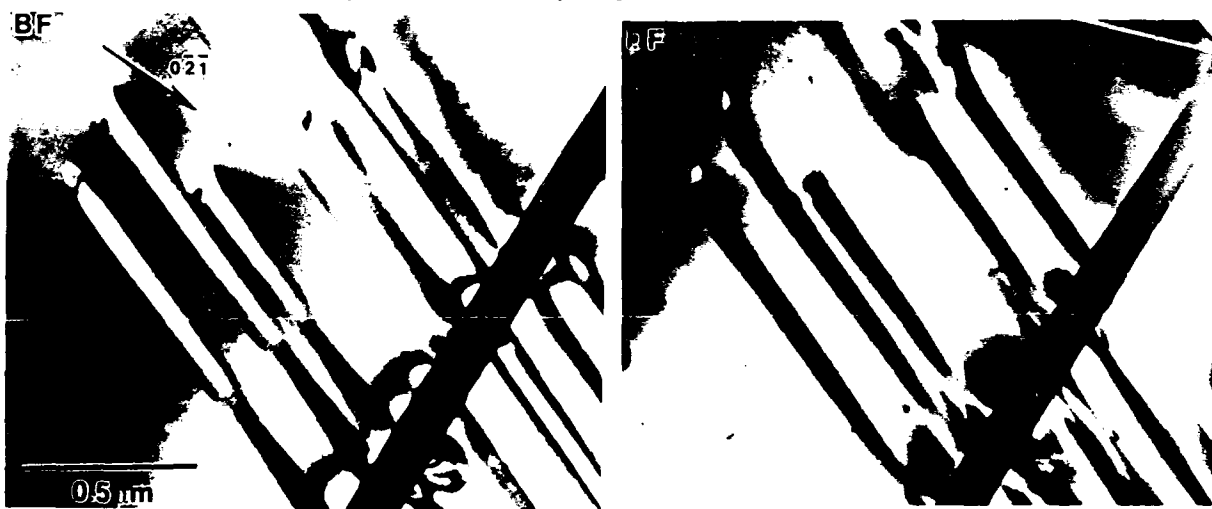
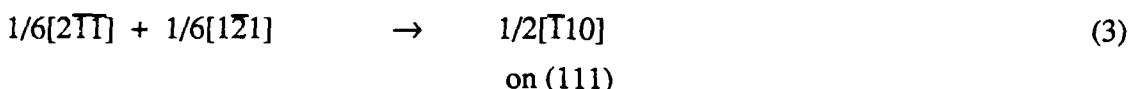
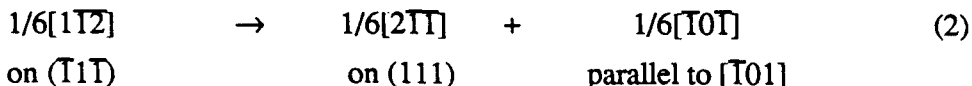
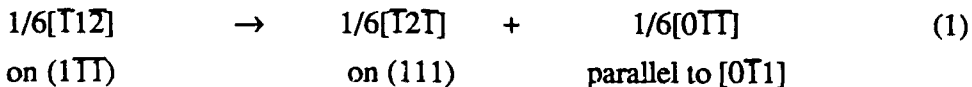


Figure 58. BF (a) and DF (b) micrographs taken with a superlattice spot showing APB contrast between $1/2<110]$ dislocations on the (001) plane in Al₃Ti deformed at 300°C.

the dissociations leading to the formation of a dislocation with $b=1/2[1\bar{1}0]$ on (111), the plane of the microtwin marked T in Fig.1b, is as follows:



The dislocation so formed may cross-slip onto the {001} plane, and glide away dragging out a ribbon of APB. The stair rod dislocations of type $1/6<101>$ remain along the directions of intersection of the inclined {111} planes, although observations of these reaction products have not been made at this time.

Al₃Ti Deformed at 600°C

Typical areas of a sample deformed at 600°C are shown in the micrographs in Figures 59a–b and 60a–b. In Figure 59, the long curved dislocations marked A are visible with $g=\bar{1}1\bar{1}$ (Figure 59b) and invisible with $g=11\bar{1}$ (Figure 59a) and also with $g=220$ (not shown), which establishes that the Burgers vectors are parallel to $[\bar{1}10]$. Furthermore, it was established that these exist as pairs of $1/2<\bar{1}10>$ screw superpartials bounding APB's on the (001) plane. The mean separation between the superpartials was measured to be 30 nm, corresponding to an APB energy on {001} of $\approx 16\text{mJ.m}^{-2}$, although in some areas, for example, that marked B in Figure 59a, this separation is much larger — on the order of 70 nm.

The micrographs in Figure 60 show several interesting features. The long, straight dislocations labelled A in Figure 60a have been identified by diffraction contrast experiments and crystallographic analysis, from which it has been established that $b=[\bar{1}12]$ and based on trace analysis it was established that these dislocations have $u=[110]$ (where u is the dislocation line vector), i.e. they are in edge orientation and lie on the (111) plane. This is the first observation revealing dislocations of type $b=<112>$ in Al₃Ti. A consideration of the atomic arrangement on the (111) plane in the DO₂₂ lattice (Figure 57) shows that $b=1/2<112>$ is a perfect superdislocation;

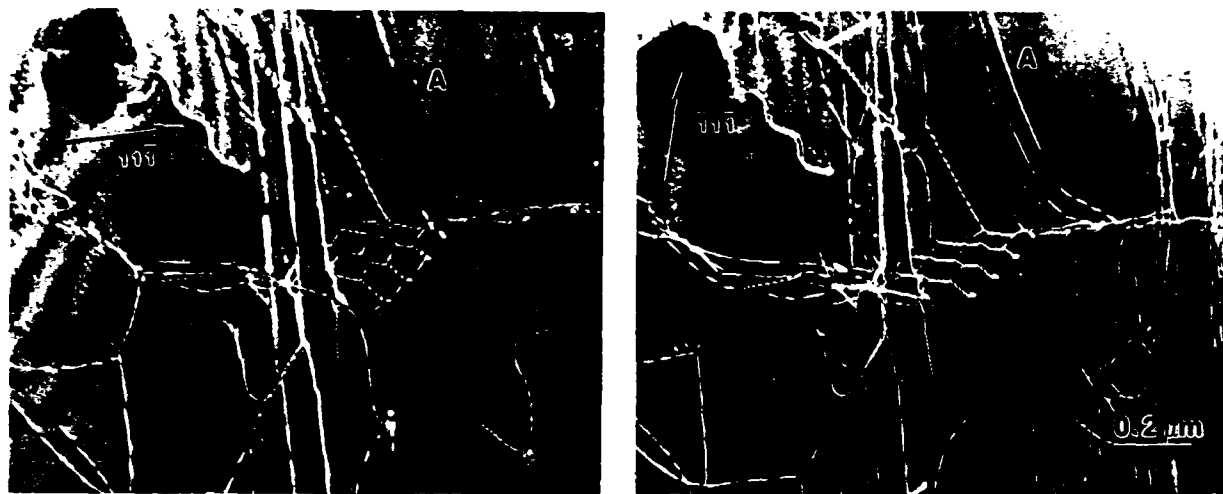


Figure 59. WBDF micrographs of dislocations in Al₃Ti deformed at 600°C. The long, curved dislocations at A lie on the (001) plane and are pairs of 1/2[T10] dislocations separated by APB's.

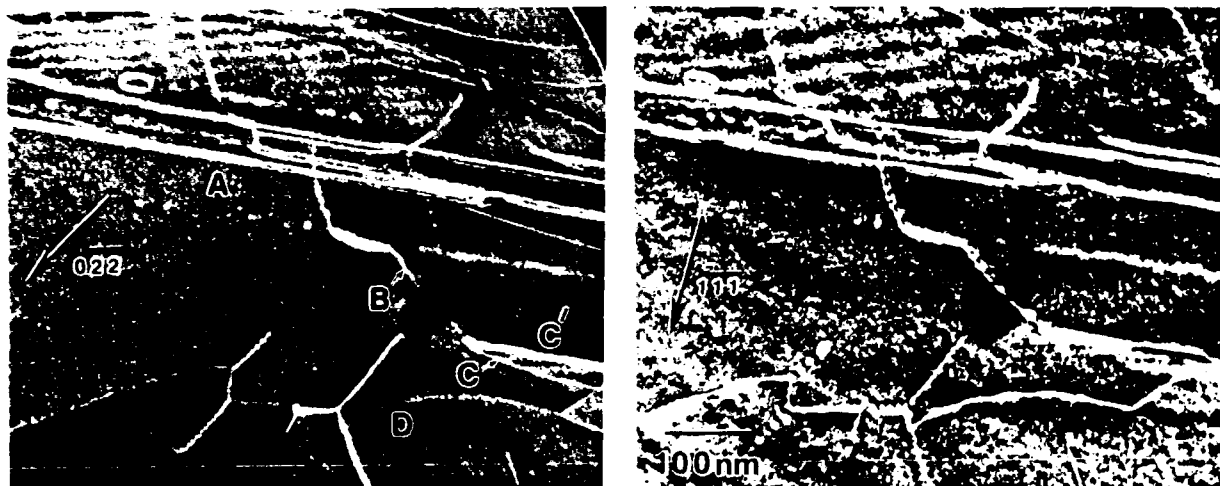


Figure 60. WBDF micrographs of dislocations in Al₃Ti deformed at 600°C. The long, straight dislocations at A form a pair: 1/6[T12] + 1/3[T12]. The segmented dislocation made up of B,C and C' has apparently begun a complicated reaction involving a dissociated dislocation on (1T1) which cross-slips onto the (001).

since the dislocations labelled A exist as a pair, it is tempting to speculate that the perfect dislocation has dissociated as $1/2[\bar{1}12] \rightarrow 1/6[\bar{1}12] + 1/3[\bar{1}12]$, similar to that in the intermetallic compound TiAl(69). It is not yet clear whether the $1/2<112>$ dislocation is a mobile dislocation capable of contributing to strain.

The second feature of significance in Figure 60 involves the dislocations marked B and C (and C'). Various images of the segment marked B are consistent with a Burgers vector lying parallel to $<110>$; the interesting observation is that these dislocations appear to be dissociated, in marked distinction with the observations made of samples deformed at 300°C. The segments marked C appear to have dissociated into a pair of dislocations lying at the intersection of the (1 $\bar{1}$ 1) and (001) planes, whereas that at C' is a $1/2[110]$ dislocation which has cross slipped on to the (001) plane. These observations indicate that the APB energy is anisotropic, i.e., higher on the {111} planes compared to the (001) plane. This provides the driving force for cross slip onto the latter plane in a manner analogous to that in Ni₃Al.

Al₆₇Ni₈Ti₂₅ Deformed at 300°C

Weak-beam dark-field (WBDF) micrographs are shown in Figures 61a-b. Diffraction contrast analysis has established that almost all the dislocations have $b = <110>$ and trace analysis revealed that the slip planes were {111}(70). Furthermore, imaging with $\pm g$ (Figure 61) reveals contrast expected from dipoles. Thus, a major fraction of the dislocations on {111} planes exist as

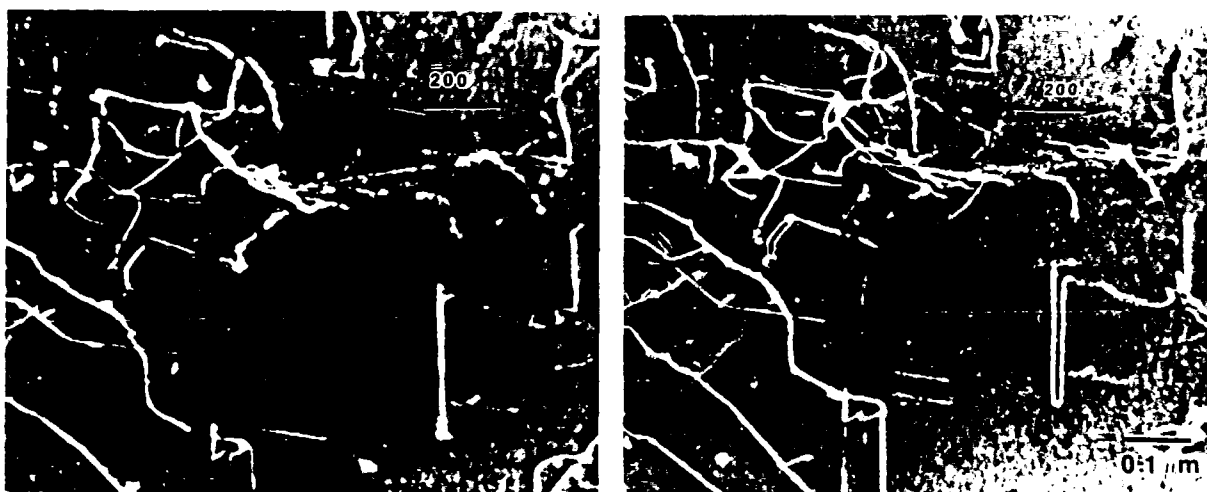


Figure 61. WBDF micrographs showing {111}<110> individual dislocations and dipoles in the Al₆₇Ni₈Ti₂₅ alloy deformed at 300°C.

dipoles and no dissociation of individual dislocations into pairs of $1/2<110>$ dislocations could be discerned. A few $<110>$ dislocations dissociated into a pair of $1/2<110>$ dislocations were observed and trace analysis indicated that these lay on the $\{001\}$ plane.

Al₆₇Ni₈Ti₂₅ Deformed at 600°C

Figure 62a-b shows WBDF micrographs of dislocations in a sample deformed at 600°C. Observations similar to those at 300°C can be made, except that there are many dislocations with $b=<110>$ which have dissociated into pairs of dislocations with $b=1/2<110>$ such as those at A in Figure 62a. Also, many of the $<110>$ dislocations are still present as dipoles shown at C. The presence of these dipoles may account for the limited ductility of this compound following the argument of Marcinkowski(71).

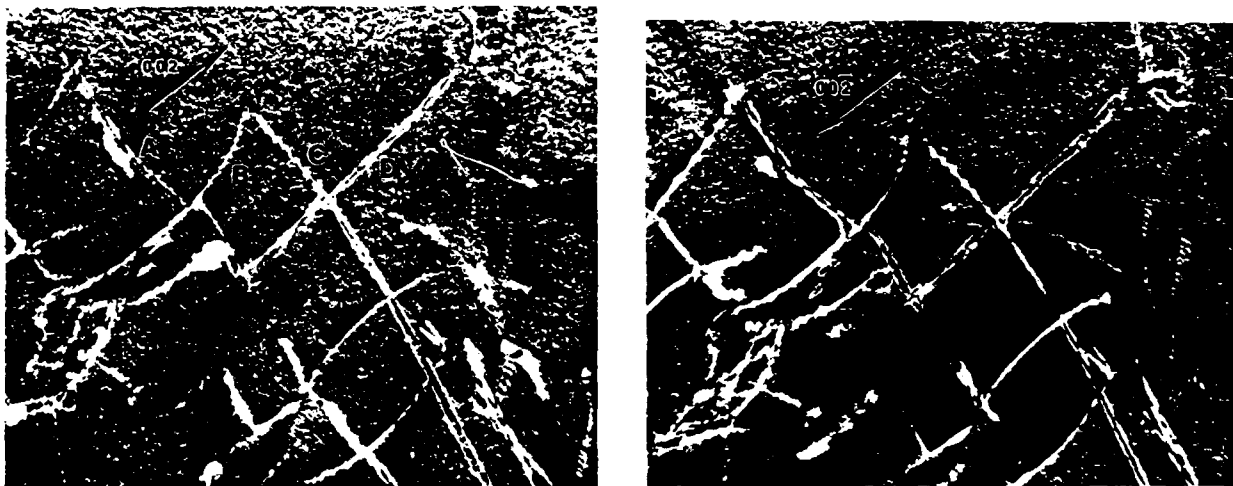


Figure 62. WBDF micrographs showing $\{111\}<110>$ individual dislocations and dipoles and $1/2<110>$ superpartial pairs on $\{001\}$ in the Al₆₇Ni₈Ti₂₅ alloy deformed at 300°C.

References

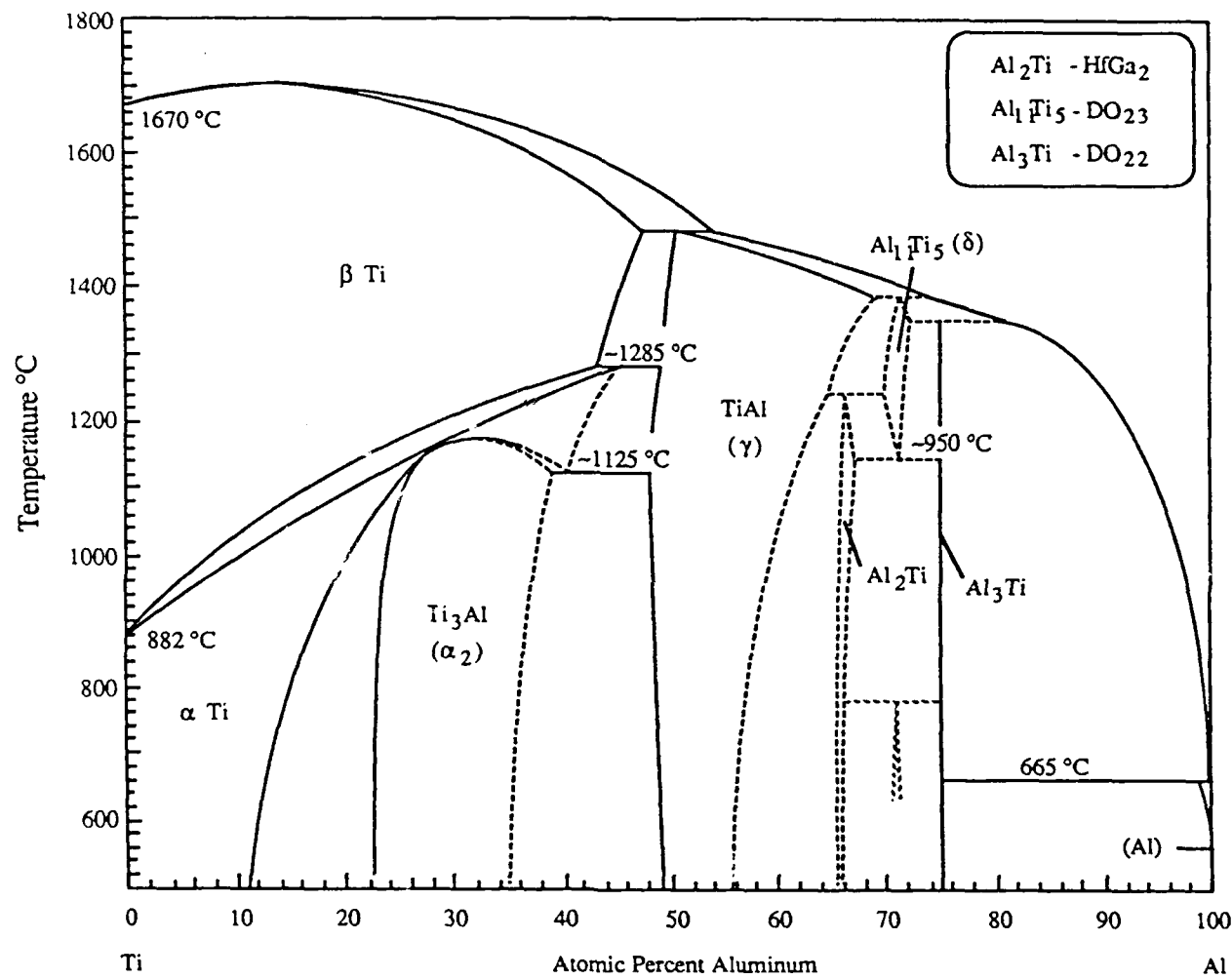
1. D. C. Van Aken and H. L. Fraser, *Acta Metall.*, 33, 963 (1985).
2. D. C. Van Aken, Ph.D. Thesis, University of Illinois, Urbana (1986).
3. J. L. Murray, Unpublished Research, NBS.
4. J. W. Cahn and G. Kalonji, in: *Solid-Solid Phase Transformations*, H. I. Aaronson, D. E. Laughlin, R. F. Sekerka and C. M. Wayman, eds., AIME, Warrendale, PA, 3 (1982).
5. W. E. Mayo and T. Tsakalakos, *Met. Trans.*, 19, 481 (1971).
6. Z. Hashin and S. Shtrikman, *J. Mech. Phys. Solids*, 11, 127 (1963).
7. D. C. Van Aken, D. J. Miller, P. Kurath and H. L. Fraser, to be published.
8. B. Nobel, S. J. Harris and K. Dinsdale, *J. Mater. Sci.*, 17, 461 (1982).
9. R.S. Leigh, *Phil. Mag.*, 42, p.139 (1951).
10. N. Dudzinski, J. R. Murray, B. W. Mott and B. Chalmers, *J. Inst. Metals*, 74, 291 (1948).
11. N. Dudzinski, *J. Inst. Metals*, 81, 49 (1952-53).
12. N. Dudzinski, *J. Inst. Metals*, 83, 444 (1954-55).
13. G. Cliff and G. W. Lorimer, *J. Microscopy*, 110, 107 (1975).
14. H. Jones, *Mater. Sci. Engr.*, 5, 1 (1969-70).
15. R. D. Field, J. W. Zindel and H. L. Fraser, *Scripta Metall.*, 20, 415 (1986).
16. P. Furrer and H. Warlimont, *Z. Metallk.*, 64, 236 (1973).
17. M. H. Jacobs, A. G. Doggett and M. J. Stowell, *J. Mater. Sci.*, 9, 1637 (1974).
18. M. Cooper, *Acta Cryst.*, 23, 1106 (1967).
19. D. J. Skinner, R. L. Bye, D. Raybould and A. M. Brown, *Scripta Metall.*, 20, 867 (1986).
20. P. Skjærpe, *Met. Trans.*, 18A, 189 (1987).
21. J. W. Steeds, in: *Introduction to Analytical Electron Microscopy*, J. J. Hren, J. I. Goldstein and D. C. Joy ,eds., Plenum Press, New York, 387 (1979).
22. B. F. Buxton, J. A. Eades, J. W. Steeds and G. M. Rackham, *Phil. Trans. Roy. Soc. Lond.*, A281, 171 (1976).
23. International Tables for Crystallography, T. Hahn (ed.),D.Reidel Publishing Co., Dordrecht, Holland, A, 604 (1984).
24. G. Phragmen, *J. Inst. Metals*, 77, 489 (1950).

25. V. G. Rivlin and G. V. Raynor, Int. Met. Rev., 26, 133 (1981).
26. D. Munson, J. Inst. Metals, 95, 217 (1967).
27. C. Y. Sun and L. F. Mondolfo, J. Inst. Metals, 95, 384 (1967).
28. J. A. Chapman and D. V. Wilson, Bull. J. Inst. Met., 91, 39 (1962-63).
29. F. C. Grensing, Ph. D Thesis, University of Illinois at Urbana-Champaign, (1987).
30. J. W. Zindel, J. T. Stanley, R. D. Field and H. L. Fraser, in "Rapidly Solidified Al Alloys", ASTM STP 890, 186, (1986).
31. Binary Alloy Phase Diagram, 2, ASM, Metals Park, OH, (1986).
32. F. C. Grensing and H. L. Fraser, Scripta Met., 21, 963, (1987).
33. Metals Handbook, Desk Edition, ASM, Metals Park, OH, (1985).
34. T. E. Leontis and F. N. Rhines, Trans. Am. Inst. Mining Met. Engrs., 166, 265, (1946).
35. J. A. Chapman and D. V. Wilson, Bull. J. Inst. Met., 91, 39 (1962-63).
36. M. Yamaguchi, Y. Umakoshi and T. Yamane, Mat. Res. Soc. Symp. Proc., 81, 275 (1987).
37. M. Yamaguchi, Y. Umakoshi and T. Yamane, Phil. Mag. A, 55, 301 (1987).
38. M. Yaaguchi and Y. Shirai, in proceedings of "Dispersion Strengthened AluminumAlloys" symposium, 1988 TMS Annual Meeting, Phoenix, AZ.
39. Y. Umakoshi, M. Yamaguchi, T. Yamane and T. Hirano, Phil. Mag. A, 58, 651, (1988).
40. K. S. Kumar and J. R. Pickens, Scripta Met., 22, 1015, (1988).
41. J. Tarnacki and Y-W. Kim, Scripta Met., Vol. 22, 329, (1988).
42. S. C. Huang, E. L. Hall and M. F. X. Gigliotti, J. Mater. Res., 3, 1, (1988).
43. D. Shechtman and L. A. Jacobson, Metall. Trans. A, 6, 1325, (1975).
44. M. J. Marcinkowski, N. Brown and R. M. Fisher, Acta Metall., 9, 129, (1961).
45. M. J. Marcinkowski and N. Brown, Acta Metall., Vol. 9, 764, (1961).
46. M. J. Marcinkowski, in: Electron Microscopy and Strength of Crystals, G. Thomas and J. Washburn, eds., Interscience Publishers, New York, 333, (1963).
47. B. H. Kear and H. G. F. Wilsdorf, Trans. Met. Soc. AIME, 224, 382 (1961).
48. K. Suzuki, M. Ichihara and S. Takeuchi, Acta Met., 27, 193 (1979).
49. P. Veyssiére, J. Douin and P. Beauchamp, Phil. Mag. A, 51, 469 (1985).

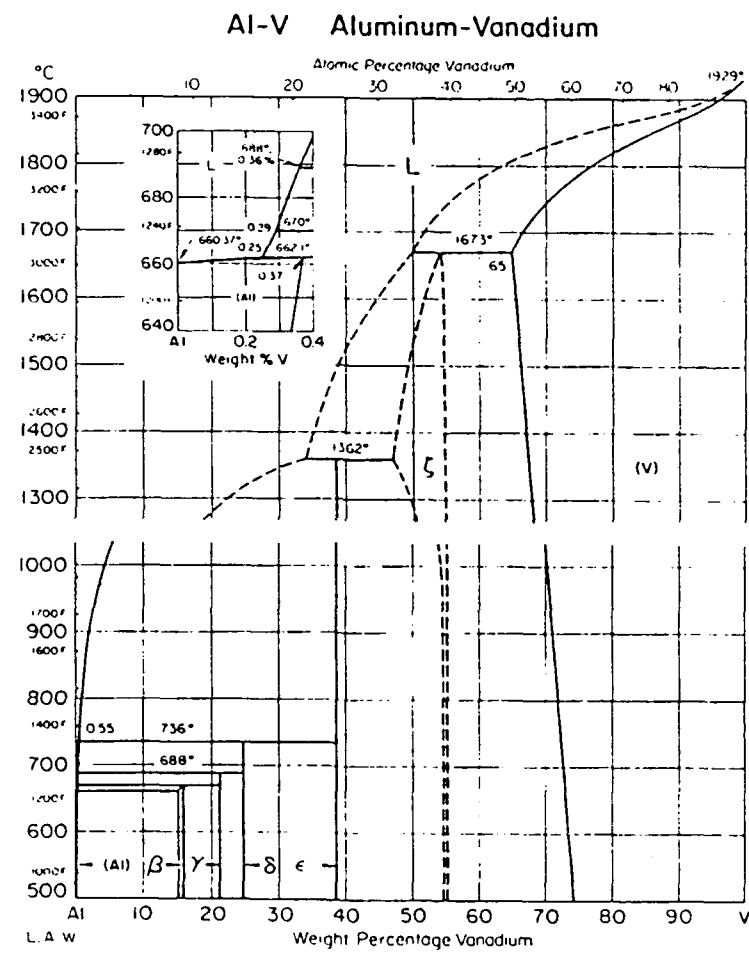
50. E. M. Shulson, Int. J. Powder Metall., 23, 25 (1987).
51. C. C. Koch, Int. Mat. Rev., 33, 20, (1988).
52. L. von Mises, Z. Angew. Math. Mech., 8, 161 (1928).
53. J. C. Williams and M. J. Blackburn, in: Ordered Alloys, B. H. Kear, C. T. Sims, N. S. Stoloff and J. H. Westbrook, eds., Claitors, Baton Rouge, LA, , 425 (1970).
54. V. K. Vasudevan, S. A. Court and Fraser, submitted to Scripta Met..
55. S. A. Court, J. A. Lofvander, M. H. Loretto and H. L. Fraser, accepted in Phil. Mag..
56. S. A. Court, V. K. Vasudevan and H. L. Fraser, submitted to Phil. Mag..
57. M. Kabbaj, A. Galerie and M. Caillet, J. Less-Common Metals, 108, 1 (1985).
58. A. Raman and K. Schubert, Z. Metallk., 56 99 (1965).
59. A. Seibold, Z. Metallk., 72 712 (1972).
60. K. S. Kumar and J. R. Pickens, Scripta Metall., 22, 1015 (1988).
61. C. D. Turner, W. O. Powers and J. A. Wert, unpublished research.
62. G. Vandershaeve and B. Escaig, Phys. Stat. Sol., 20(a), 309 (1978).
63. G. Vandershaeve, T. Sarrazin and B. Escaig, Acta Met., 27, 1251 (1979).
64. G. Vandershaeve and B. Escaig, Phil. Mag. A, 48, 265 (1983).
65. P. Villars and L. D. Calvert, Pearson's Handbook of Crystallographic Data for Intermetallic Phases, Vol. 2, ASM, Metals Park, OH, 1985, 1079.
66. P. G. Nash, V. Vejins and W. W. Laing, Bull. Alloy Phase Dia., 3, 367 (1982).
67. R. Wheeler, V. K. Vasudevan and H. L. Fraser, to be published.
68. G. Vandershaeve and B. Escaig, in Dislocations in Solids, 319 (1985).
69. G. Hug, A. Loiseau and A. Lasalmonie, Phil. Mag., 54 47 (1986).
70. R. Wheeler, V. K. Vasudevan and H. L. Fraser, to be published.
71. M. J. Marcinkowski, Phys. Stat. Sol. (a), 90, 621 (1985).

90
Appendix A

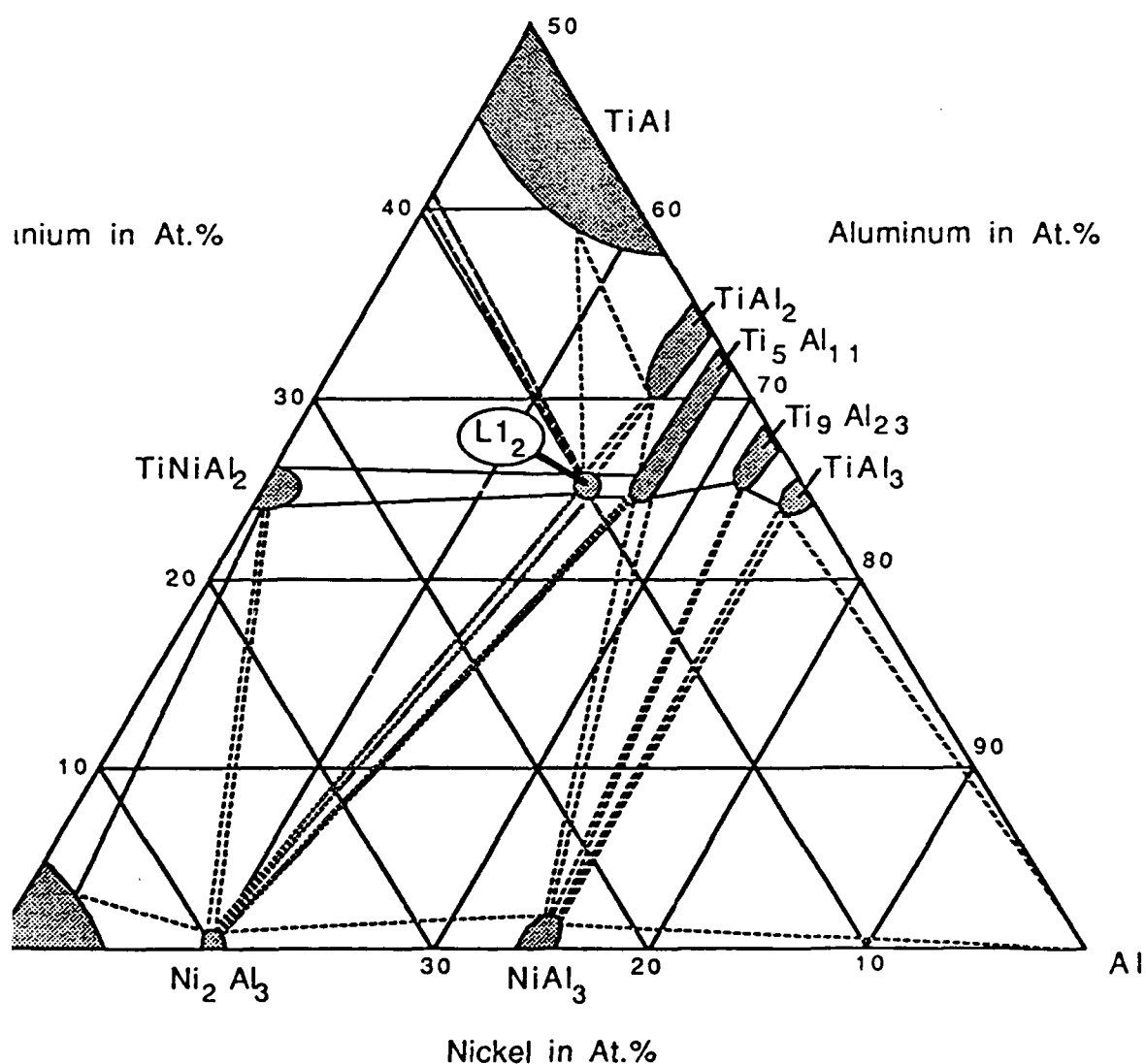
Titanium - Aluminum Alloy System



91
Appendix B



Al-Ti-Ni Isothermal Phase Section at 800°C



(from A. Raman and K. Schubert, Z. Metallkde, 56, (1965),99)

Publications From This Program

1. Dynamic Compaction of Al Alloys, in "Rapidly Solidified Al Alloys", ASTM STP 890, 1986, p.304, with J.W. Sears and D.J. Miller.
2. The Microstructure of Rapidly Solidified Hyper-Eutectic Al-Be Alloys, Acta Met., 33, 963, 1985, with D.C. Van Aken.
3. Rapid Solidification and Subsequent Analysis of Some Hypereutectic Al-base Alloys, in "Rapidly Solidified Al Alloys", ASTM STP 890, 1986, p.186, with J.W. Zindel, J.T. Stanley and R.D. Field.
4. The Intercellular Phase in Rapidly Solidified Alloys Based on the Al-Fe System, Scripta Met., 20, p. 415, 1986, with J.W.Zindel and R.D.Field.
5. Nucleation in the Presence of a Metastable Liquid Miscibility Gap in the Aluminum Beryllium System, Hume-Rothery Memorial Symposium, (1986: New Orleans, LA), Undercooled Alloy Phases, Ed. E.W. Collings and C.C. Koch, TMS-AIME, Warrendale, PA, 1986, p.413, with D.C. Van Aken.
6. Microstructures and Properties of Rapidly Solidified Al-Fe-(Mo/Ce) Alloys, in "Aluminium Alloys: Their Physical and Mechanical Properties", E.A. Starke, Jr. and J.H. Sanders, Jr. Eds., Chameleon Press, Ltd., London, 1986, p. 279, with J.W. Zindel, R.D. Field, P. Kurath.
7. Mechanical Properties of Rapidly Solidified Al-4Be Alloys, in "Aluminum Alloys: Their Physical and Mechanical Properties", E.A. Starke, Jr. and J.H. Sanders, Jr. Eds., Chameleon Press, Ltd., London, 1986, p. 295, with D.C. Van Aken, P. Kurath.
8. The Formation of Microstructures in Rapidly Solidified Hypereutectic Al Alloys Containing Ni or Co, in "Aluminim Alloys: Their Physical and Mechanical Properties", E.A. Starke, Jr. and J.H. Sanders, Jr. Eds., Chameleon Press, Ltd., London, 1986, p.307, with J.T. Stanley, R.D. Field.
9. Rapid Solidification of Al Alloys: in "Aluminum Alloys:Their Physical and Mechanical Properties", E.A. Starke, Jr. and J.H. Sanders, Jr. Eds., Chameleon Press, Ltd., London, 1986, p.1321.
10. Structure and Magnetism of Quasicrystalline and Crystalline $\text{Al}_{1-x}\text{Mn}_x$ Alloys, Phys. Rev. B, 1986, 34, 2960, with S.E.Youngquist, P.F.Miceli, D.G.Wiesler and H.Zabel.
11. Microstructure and Properties of Rapidly Solidified Magnesium Lithium Alloys, in "Processing of Structural Metals by Rapid Solidification", ed. F.H.Froes and S.J.Savage, ASM, Metals Park, 1987, p. 429, with F.C. Grensing.
12. Microstructure and Properties of Rapidly Solidified Material Consolidated by Dynamic Compaction and Hot Isostatic Pressing, in "Processing of Structural Metals by Rapid Solidification", ed. F.H.Froes and S.J.Savage, ASM, Metals Park, 1987, p. 133, with D.J. Miller and J.W.Sears.
13. Identification of Precipitates in Rapidly Solidified and Heat-Treated Al-8Fe-2Mo-Si Alloys, Scripta Met., 21, 1987, p.1105, with V.K. Vasudevan.

14. Microstructure of Melt-Spun Magnesium-Silicon Alloys, *Scripta Met.*, **21**, 1987, p.963, with F.C. Grensing.
15. Structure and Properties of Rapidly Solidified Mg-Si Alloys, *Mat. Sci. and Eng.*, 1988, **98**, 313, with F.C.Grensing.
16. The Microstructures of Rapidly Solidified and Heat-Treated Al-8Fe-2Mo-Si Alloys, *Mat. Sci. and Eng.*, 1988, **98**, 131, with V.K. Vasudevan.
17. Monotectic Solidification in RS Al-In Alloys, *Int. J. of Rapid Solid.*, 1988, **3**, 199, with D.C. Van Aken.
18. A Microstructural Comparison of Melt Spun and Laser Surface Melted Aluminum-Molybdenum Alloys, accepted for publication in *Met Trans. A.*, with F.C. Grensing.
19. The Mechanism of Formation of Microstructure in Rapidly Solidified Hypereutectic Al Alloys, *Acta. Met.*, in press, with J.T. Stanley, R.D. Field.
20. Oxidation Behavior of Some Mg-Li and Mg-Li-Si Alloys, Proc. Symp. on *Light-weight Alloys for Aerospace Applications*, TMS Ann. Meeting, Las Vegas, NV, 1989, with S. Das.
21. Electron Microscopy Studies in Rapid Solidification Processing, *Inst. Phys. Conf. Ser.* No. 93, 1988, **2**, 185.

Doctor of Philosophy Degrees supported by this program

1. Jacob Zindel: Microstructures and Properties of Rapidly Solidified Aluminum Alloys (January 1986).
2. David Van Aken: Al-Be Composites Produced by Rapid Solidification (May 1986).
3. Fritz Grensing: Microstructural Enhancement of Magnesium Alloys For Elevated Temperature Applications Using Novel Processing Techniques (August 1987).
4. Dean Miller: The Consolidation of Rapidly Solidified Particulate by Dynamic Compaction and Hot-Isostatic Pressing (September 1987).
5. Siddhartha Das: A Study of Alloys Based on the Mg-Li System (February 1989).
6. James Stanley: Rapid Solidification Studies of Al and Ti Alloys (May 1989).
7. Daira Legzdina: Deformation Mechanisms in Rapidly Solidified Aluminum Alloys (May 1989).
8. Robert Wheeler: Elevated Temperature Deformation Studies of Al_3X -Based Intermetallics (May 1989).